Christian-Albrechts-Universität zu Kiel
Institut für Experimentelle und Angewandte Physik
Extraterrestrische Physik

Dissertation
zur Erlangung des Doktorgrades
der Mathematisch-Naturwissenschaftlichen Fakultät
der Christian-Albrechts-Universität zu Kiel

Particle Flux Directionality and other Aspects of the Martian Radiation Environment

An Analysis of MSL/RAD Observation Data and Simulation Data

Jan Kristoffer Appel

Kiel, im August 2018

Referent/in:	Robert F. Wimmer-Schweingruber
Koreferent/in:	Wolfgang J. Duschl
Datum der mündlichen Prüfung:	26.11.2018
Zum Druck genehmigt:	26.11.2018

ABSTRACT

Mars is a place of particular interest in the exploration of the solar system because it is one of the places that may have been home to microbial life forms in the past. It is also a prominent target for future manned exploration. Both the past and the present habitability of Mars, and the safety of astronauts working on the Martian surface, depend, among other factors, on the environment of ionizing radiation present on the Martian surface.

As part of the Mars Science Laboratory (MSL) mission, the Radiation Assessment Detector (RAD) on board the Curiosity rover aims to measure the Martian radiation environment. The instrument has been jointly developed by the Christian-Albrechts-University of Kiel (CAU) and the Southwest Research Institute (SwRI). One of the scientific goals being addressed by the instrument is to aid in the validation of particle transport models used to simulate the radiation environment on the Martian surface. This thesis aims to address this goal in particular.

Global dust storms are a meteorological feature that is unique to Mars. These storms produce a striking difference in the appearance of the planet, obscuring almost all of its surface beneath a dense layer of dust. As of the date of this writing, there have been no measurements of the influence of the lofted dust on the radiation environment on the Martian surface. This is simply due to the fact that no global dust storm has occurred during the time RAD has been active. In order to predict the changes in radiation environment, simulations comparing a global dust storm to normal atmospheric conditions are performed. Additionally, an attempt is made to validate the results of the simulations using a period of enhanced dust activity that is included in the RAD measurement time.

The Martian radiation environment is dominated by downward particle fluxes of Galactic Cosmic Rays (GCRs) and the secondary particles produced by them. Near the Martian surface, an upward-directed component composed of secondary particles produced in the Martian soil adds to the total radiation environment. In order to fully characterize the radiation environment, this upward component must be understood as well. A method for discriminating particle directionality in RAD for charged particles is developed through simulations and validated through instrument observations. The RAD instrument is unable to determine directionality for neutrons due to its design. However, since neutrons are important for dosimetry, an instrument design capable of measuring neutron directionality is described and its basic capabilities assessed.

ZUSAMMENFASSUNG

Im Sonnensystem ist Mars von besonderem Interesse, da er in der Vergangenheit möglicherweise mikrobielle Lebensformen beherbergt haben könnte. Ebenso ist Mars ein Hauptziel für zukünftige bemannte Missionen. Die Kenntnis des Feldes ionisierender Strahlung auf dem Mars ist sowohl für die Beurteilung der früheren und heutigen Habitabilität als auch für die Sicherheit zukünftiger Astronauten von großer Bedeutung.

Im Rahmen der Mission Mars Science Laboratory (MSL) mißt das Instrument Radiation Assessment Detector (RAD) an Bord des Rovers Curiosity die Strahlungsumgebung auf dem Mars. Das Instrument wurde gemeinsam von der Christian-Albrechts-Universität zu Kiel (CAU) und dem Southwest Research Institute (SwRI) entwickelt. Eines der wissenschaftlichen Ziele des Instrumentes ist die Validierung von Teilchentransportmodellen. Dieses Ziel wird in der vorliegenden Arbeit vorrangig verfolgt.

Globale Staubstürme sind ein Phänomen, das ausschließlich auf dem Mars vorkommt. Solche Stürme verursachen markante Veränderungen des Planeten, da nahezu die gesamte Oberfläche durch eine dichte Staubschicht verdeckt wird. Zum Zeitpunkt dieser Veröffentlichung gab es keine Beobachtungen des Einflusses solcher Staubstürme auf die Strahlungsumgebung des Mars, da innerhalb der Messzeit von RAD kein solcher Sturm aufgetreten ist. Um Vorhersagen über diesen Einfluss machen zu können, wurden Simulationen, die einen globalen Staubsturm mit normalen Atmosphärenbedingungen vergleichen, durchgeführt. Zusätzlich wurde ein Versuch unternommen, die Simulationsergebnisse anhand einer innerhalb der RAD- Messungen liegenden Zeit mit erhöhter Staubaktivität zu validieren.

Die Strahlungsumgebung auf dem Mars wird durch abwärts gerichtete Teilchenflüsse, Galactic Cosmic Rays (GCRs) und ihre Sekundärteilchen, dominiert. Nahe der Oberfläche existiert zusätzlich eine aufwärts gerichtete Komponente aus innerhalb des Bodens produzierten Sekundärteilchen. Um die Strahlungsumgebung vollständig zu beschreiben, ist es notwendig, diese aufwärts gerichtete Komponente zu verstehen. Hier wurde eine Methode zur Unterscheidung der Teilchenrichtung geladener Teilchen im RAD anhand von Simulationsdaten entwickelt und durch Observationsdaten validiert. Aufgrund seiner Konstruktion ist RAD nicht in der Lage, die Richtung von Neutronen zu messen. Da sie aber für die Dosimetrie relevant sind, wurde ein Instrument, das dazu in der Lage ist, vorgestellt und seine grundlegenden Eigenschaften beurteilt.

ACKNOWLEDGEMENTS

Without the help of many people, this thesis would not have been possible. I want to thank the following groups and people in particular, without any weighing implied in the order of this list.

Robert Wimmer-Schweingruber offered the opportunity for this thesis and made this work possible in the first place. In addition, I want to thank him for keeping his door and ear always open, despite a full schedule. The discussions I had with him, and his ideas, were essential to the thesis.

The members of the AG Extraterrestrial Physics at the University of Kiel, both current and former, not only provided valuable input during discussions, but also for the excellent, friendly and open working climate in the group, as well as sufficient distractions after work.

I have had many stimulating discussions with the members of the MSL/RAD team on team meetings, conferences and via email. These discussions furthered my understanding of the topics addressed in this thesis, and thus improved it. I want to thank Jingnan Guo, Henning Lohf and Jan Köhler in particular for the daily work we did together.

Cindy Hugenschmidt has provided me with a shoulder to lean on, a push when I needed it, and valuable input to my work, in equal measure. Her unwavering optimism always provides a light in difficult times.

My parents, Maren and Gerhard Appel, have enabled and helped me to get to the point of performing the work presented in this thesis in the first place. I will always be grateful to them for making it possible for me to have the choices I had. They always stood by me when I needed it.

My friends and family have always been curious about and interested in my work. Talking about and explaining these topics to them have also improved my understanding and led to an outside viewpoint that I sometimes lack.

CONTENTS

LIST OF FIGURES

LIST OF TABLES

LIST OF ACRONYMS

ACE Advanced Composition Explorer 27
ACR Anomalous Cosmic Ray 26
AGN Active Galactic Nucleus 25
APXS Alpha-Particle X-ray Spectrometer 33
BESS Balloon-borne Experiment with Superconducting Spectrometer 27
BO10 Badhwar-O'Neill 2010 39
CAD Computer Aided Design 108
CAU Christian-Albrechts-University of Kiel 18
CERN European Organization for Nuclear Research 36
CIR Co-rotating Interaction Region 28
CME Coronal Mass Ejection 26
CRIS Cosmic Ray Isotope Spectrometer 27
CsI(Tl) Thallium-doped Cesium Iodide 23
CO_2 Carbon dioxide 25
DAN Dynamic Albedo of Neutrons 93
ESA European Space Agency 38
Geant4 Geometry and Tracking version 4 108
GLE Ground-Level Event 27
GCM General Circulation Model 108
GCR Galactic Cosmic Ray 103
HEAO High Energy Astronomy Observatory 27
HDS Hydrogen Detection Sensor 95
HMF Heliospheric Magnetic Field 26
HZETRN High-Charge and Energy Transport 41
IMP-8 Interplanetary Monitoring Platform - 8 28
LIS Local Interstellar Spectrum 27
MSL Mars Science Laboratory 107
MCD Mars Climate Database 107

MER Mars Exploration Rover 32
MGS Mars Global Surveyor 26
MRO Mars Reconnaissance Orbiter 32
NDS Neutron Directionality Sensor 96
PCB Printed Circuit Board 100
PHA Pulse Height Analysis 23
PHITS Particle and Heavy Ion Transport code System 39
PMT Photo-Multiplier Tube 109
PUI Pick-Up Ion 26
QMD Quantum Molecular Dynamics 39
RAD Radiation Assessment Detector 107
RAMA Radiation, neutron Albedo, and Mapping of hydrogen . . . 95
REB RAD Electronics Box 111
RSH RAD Sensor Head 21
SEP Solar Energetic Particle 108
SSD Solid State Detector 73
SwRI Southwest Research Institute 18
TNS Thermal Neutron Sensor 97
ToF Time of Flight 109
eUV extreme Ultra- Violet 33

EIDESSTATTLICHE ERKLÄRUNG

Ich versichere an Eides Statt, dass ich die vorliegende Dissertation in Form und Inhalt eigenständig angefertigt habe. Abgesehen von der Beratung durch meine Betreuer und der angegebenen Literatur wurde die Arbeit ohne fremde Hilfe erstellt. Ich versichere, dass ich keine andere als die angegebene Literatur verwendet habe. Diese Versicherung bezieht sich auch auf alle in dieser Arbeit enthaltenen Grafiken und bildlichen Darstellungen.

Die Arbeit als Ganzes wurde bisher keiner anderen Prüfungsbehörde vorgelegt. Teile der Arbeit wurden bereits in Fachzeitschriften veröffentlicht und sind als solche gekennzeichnet. Die Quellennachweise der in den einzelnen Veröffentlichungen referenzierten Inhalte finden sich in der jeweiligen Veröffentlichung selbst und werden nicht zusätzlich im Quellennachweis dieser Arbeit aufgeführt. Für das Einbinden der Veröffentlichungen in diese Arbeit wurde die ausdrückliche Genehmigung der publizierenden Fachzeitschrift eingeholt.

Ich erkläre abschließend, dass die Arbeit unter Einhaltung der Regeln guter wissenschaftlicher Praxis der Deutschen Forschungsgemeinschaft entstanden ist.

Kiel, den 20. Dezember 2018 _____

(Jan Kristoffer Appel)

1

INTRODUCTION

One of the most important questions science is facing today is whether or not there is, or has been, life in other places than on Earth. This, of course, includes not only present life, but also past life. Thus, places where this question can be studied are of supreme interest today.

Mars, our planetary neighbor, is one of the places within our solar system in which life might conceivably have evolved once. Furthermore, Mars has the potential for being a future habitat for humanity.

Mars has been studied for a long time, with theories and search of past and present life being made from the start. Perhaps one of the most well-known studies was performed by Giovanni Schiaparelli in the second part of the 19th century (e. g., Schiaparelli (1893) and Schiaparelli (1899)). He created maps of albedo features, giving them names that are still in use today. The channels and lakes described by Schiaparelli inspired many theories about a civilization on Mars, e. g., by Percival Lowell (Lowell, 1906).

Today, no evidence of past or present life on Mars has been found. Studies are continuing nevertheless using a variety of methods, including remote observations (e. g., Montabone et al. (2006) and Purucker et al. (2000)) and meteoroids found in Antarctica (e. g., Mittlefehldt (1994) and Min et al. (2017)). The most well-known studies presently underway are carried out in situ by robotic probes. The latest of those explorers to date is Curiosity, a rover landed on the Martian surface by the Mars Science Laboratory (MSL) mission (Grotzinger et al., 2012). Curiosity touched down in August 2012 inside Gale Crater near the Martian equator.

The importance of Gale crater as a study site for assessing the past habitability on Mars has been detailed in Grotzinger et al. (2012). The Gale crater satisfies both the engineering and safety constraints to the mission as well as being a scientifically interesting region. The site allows access to various features allowing an in-depth study of the Martian environment with regards to its habitability through both its location and its topography.

Gale crater is located near the Martian equator at a latitude of 5.4 °S and a longitude of 137.8 °E. The crater has a diameter of approximately 150 km with a pronounced central peak, called Aeolis Mons or Mount Sharp. Gale crater is straddling a sharp contrast in local topography, with low flatlands to the north and a highland region to

the south. Evidence of aqueous flows on the surface has previously been observed at the boundary of these regions. Furthermore, through its topography, Gale crater allows access to a wide range of features for studying the habitability of the Martian environment:

- The crater bed shows an alluvial fan as well as layered sedimentary material, locally penetrated by small craters.
- Aeolis Mons allows access to almost 5 km of stratified rocks of various composition.

In total, Gale crater is a site well suited to studying the Martian habitability, allowing the MSL mission to meet its science objectives. These are

- to investigate the chemical building blocks of life (carbon, hydrogen, nitrogen, oxygen, phosphorus, and sulfur),
- to identify features that may represent the effects of biological processes (biosignatures),
- to interpret the processes that have formed and modified rocks and soils,
- to assess long-timescale (i. e., 4-billion-year) Martian atmospheric evolution processes,
- to determine present state, distribution, and cycling of water and carbon dioxide, and
- to characterize the broad spectrum of surface radiation, including cosmic radiation, solar particle events and secondary neutrons.

The surface radiation environment is of prime importance for assessing the past and present habitability of Mars. The goal of characterizing this environment is met by the Radiation Assessment Detector (RAD) instrument onboard the Curiosity rover. RAD is co-developed by the Christian-Albrechts-University of Kiel (CAU) and the Southwest Research Institute (SwRI), with the RAD Sensor Head (RSH) being developed at the CAU, and the RAD Electronics Box (REB) being developed at the SwRI. RAD employs a stack of Silicon Solid State Detector (SSD) on top of two scintillation detectors in order to measure particle type and total energy of ionizing particles. A more detailed description is given in Chapter 2.

The Martian environment is radically different compared to that of Earth in almost all aspects. A full description of the environment is given in Chapter 3, but as a brief description, the differences relevant for this work are:

- The Martian atmosphere is considerably thinner than Earth's, with typical surface pressure inside Gale crater being about 7 ‰ of surface pressure at sea level on Earth, and is almost completely composed of Carbon dioxide (CO_2).
- The Martian atmosphere and soil are extremely arid.
- Mars lacks a global magnetic field. There are local remnants of an earlier global field, but Gale Crater shows no relevant magnetic field.

When studying the radiation environment on Mars, these differences result in a complete lack of magnetic shielding and a vastly reduced shielding by the atmosphere. While the primary sources of particle fluxes for Earth and Mars are extremely similar, this results in vastly different radiation environments on the planetary surfaces.

Simulation data is used extensively in this work. It is used both as a tool for interpreting the observations made by the RAD instrument, as well as for verification of particle transport simulation codes. A discussion of two different approaches to such codes, as well as a description of the codes and applications used herein, are given in Chapter 4.

Despite all differences, there are similarities between Earth and Mars. The most obvious is perhaps the presence of seasons (e. g., Hess et al. (1980)). The meteorological effects of the seasons are driven by the sublimation and resublimation of CO_2 ice between the northern and southern polar caps. The transport of gases generates global wind patterns and drives large-scale meteorology. Due to these winds, the extremely small sand grains, called fines, can be lofted into the atmospheric column, resulting in a dust storm. Dust storms can persist for some weeks, and a local storm is not an uncommon occurrence. During the northern winter, a local dust storm can grow to a large storm encompassing a large portion of the planet. This is called a global dust storm.

Global dust storms enshroud most of the planet with an extensive presence of dust in the atmospheric column. This obviously leads to mass added to the atmosphere and may enhance atmospheric shielding against incoming energetic particle fluxes. Furthermore, the heavy dust loading in the atmosphere increases the amount of heavy elements, part of the composition of the fines, in the atmospheric column. These elements are not normally present in the atmosphere in such concentrations. This may result in an altered spectrum of secondary particles generated within the atmosphere.

To date, no measurements of the radiation environment during a global dust storm have been made. This is simply due to the fact that no such storm has occurred within the MSL mission. However, there exists modeling work by Norman, Gronoff, and Mertens (2014) attempting to characterize the influence of dust on ground- level

particle spectra using the High-Charge and Energy Transport (HZETRN) transport code (Wilson et al., 1995). In this work, the results of Norman, Gronoff, and Mertens (2014) are extended using the Planetocosmics application, which is based on the Geometry and Tracking version 4 (Geant4) particle transport code. This will not only further prepare the ground for observations during global dust storms, should they occur during the mission, but it will also allow an assessment of the predictions made by the HZETRN model used by Norman, Gronoff, and Mertens (2014) versus the predictions made by the Planetocosmics code used in this work. This analysis is presented in Chapter 5.

The Martian radiation environment not only consists of downward-directed primary particle fluxes, namely Galactic Cosmic Ray (GCR) and Solar Energetic Particle (SEP), but also in a large part of secondary particles induced by the primary particles inside the Martian atmosphere. Additionally, there is an upward- directed particle flux induced in the atmospheric column and the Martian soil.

The characterization of the upward flux both in simulation and observation is a major part of this work. This will allow for an assessment of the importance of these particles for dosimetry, and thus, for habitability. Furthermore, it will allow an assessment of the quality of the simulation codes used here. Chapter 6 gives more details.

While findings and results are discussed individually within the chapters, a summarizing discussion and conclusions are given in Chapter 7.

2

THE RADIATION ASSESSMENT DETECTOR INSTRUMENT

As stated in the introduction, the characterization of the Martian radiation environment is one of the main science goals of the Mars Science Laboratory (MSL) mission. The instrument that meets this goal is the Radiation Assessment Detector (RAD) instrument. The primary science goals of RAD, as stated by (Hassler et al., 2012), are

- to measure energetic particle spectra at the surface of Mars,
- to measure dose and determine dose equivalent rates for human explorers on the surface of Mars,
- to use these measurements to enable validation of Mars atmospheric transmission models and radiation transport codes,
- to provide input to the determination of the radiation hazard and potential mutagenic influences to life at or just below the Martian surface, and
- to provide input to the determination of the chemical and isotopic effects of energetic particles on the Martian surface and atmosphere.

In order to accomplish the different goals, RAD is a complex instrument including many different detection channels. A complete description is beyond the scope of this work and have been described elsewhere (Hassler et al., 2012). Instead only the features and capabilities of RAD relevant for the present thesis and needed for its understanding will be described.

A sketch of the construction of RAD is shown in Fig. 2.1. The two major components are the RAD Sensor Head (RSH) in silver and the RAD Electronics Box (REB) in gold. The REB contains the electronics necessary for the operation of the instrument. It will not be discussed in detail here. The RSH has two major components, the Solid State Detector (SSD) telescope on top, followed by scintillators below.

RAD is composed of six detectors in total. The SSD telescope contains three silicon diodes, followed by two scintillators. An additional scintillator surrounds the other two scintillators from the side and below. The following description of the detector shapes, materials and properties is taken from Hassler et al. (2012), unless otherwise stated.

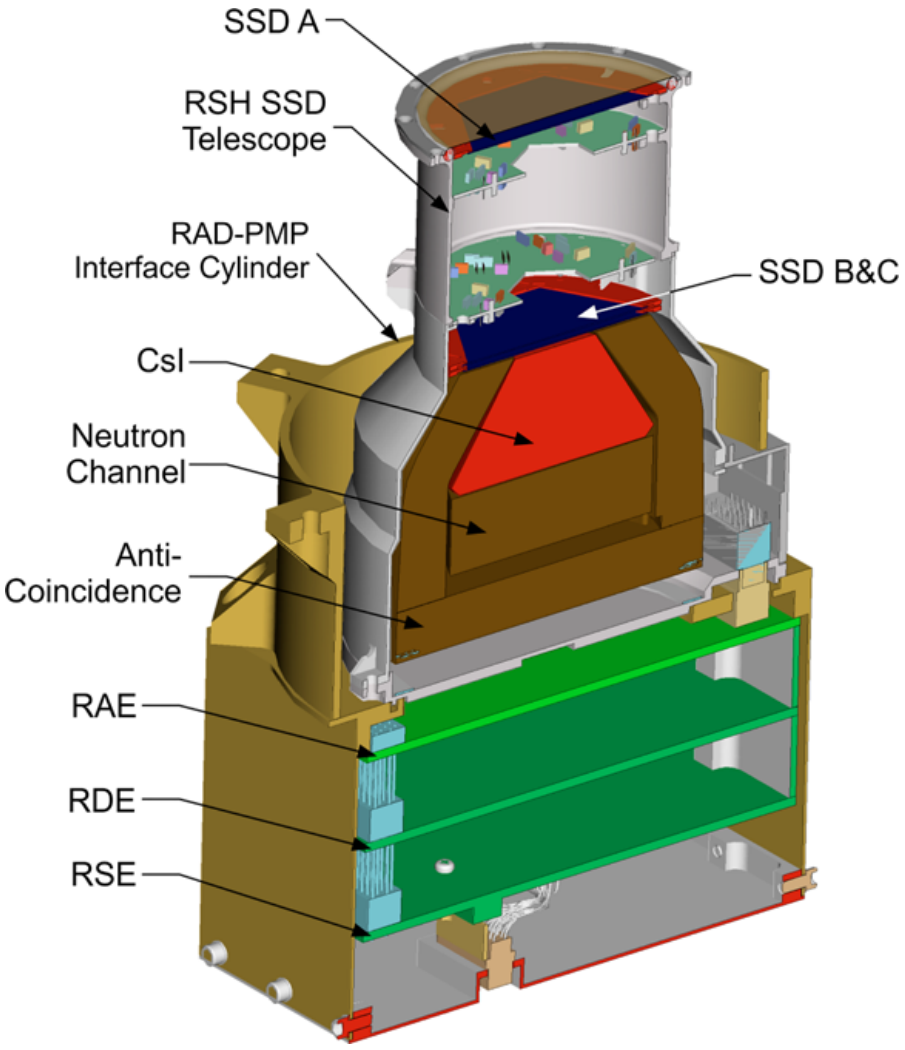

Figure 2.1: Cartoon drawing showing the construction of the Radiation Assessment Detector (RAD). Major components visible include the RAD Sensor Head (RSH) in silver and the RAD Electronics Box (REB) in gold. Taken from Hassler et al. (2012).

A sketch of detector nomenclature and detection logic is shown in Fig. 2.2. The particle telescope on top of the sensor head contains the SSDs called A, B and C. Each silicon diode has a hexagonal shape and is 300 µm thick. The individual diodes are further segmented into an outer and an inner segment. Detectors B and C utilize only the inner segment, while detector A is split into the outer segment A1 and the inner segment A2. The segments of A and the B detector define the possible view cones of the instrument. The inner view cone, defined by the coincidence of detectors A2 and B, has an opening angle of 18°, while the coincidence of A1 and B defines the outer view cone with an opening angle of 30° (Zeitlin et al., 2013). Detector B is additionally used as a trigger for particle detection, requiring at least an energy deposit in one of the A detectors and the B detector for a particle to be accepted.

The scintillation detectors are called D, E, and F. Detector D is a truncated hexagonal pyramid made of Thallium-doped Cesium Iodide (CsI(Tl)). The pyramids opening angle is selected to fully cover the inner view cone defined by the A1-B- coincidence. Detector D is intended to supply a measurement of the total particle energy for proton and alpha particles of up to $95\,MeV\,nuc^{-1}$. Due to its high density, it is also sensitive to gamma rays.

Detector E is made of a tissue-equivalent plastic called BC-432m. Its intended use is as a neutron channel for the detector. However, high-energy particles will also deposit energy in the E detector. It has an extruded hexagonal shape with the same width as the base of the D detector. It should be noted that particle trajectories within the A1-B-coincidence are not fully covered by detector E, but trajectories within the narrower A2-B- coincidence will be fully covered by it.

The scintillator wrapped around the side and bottom of the D and E detector is called the F detector. It is composed of BC-432m as well. It is used as an anti-coincidence shield to veto particles entering the detector stack from below. It is not intended to be used for particle energy measurements.

RAD provides several different direct data products, among others dosimetry and Pulse Height Analysis (PHA) data. Dosimetry data is provided by detectors B and E each. They are used omnidirectionally for dosimetry data, measuring any particle depositing energy in one of the detectors with no other coincidence requirements.

The data product used most frequently in this work is PHA data. It lists the energy deposit in each individual detector generated by each individual particle event. Different coincidence requirements are used to generate PHA data. Of particular note are penetrating particles, which require that energy be deposited in each detector, from A2 to F.

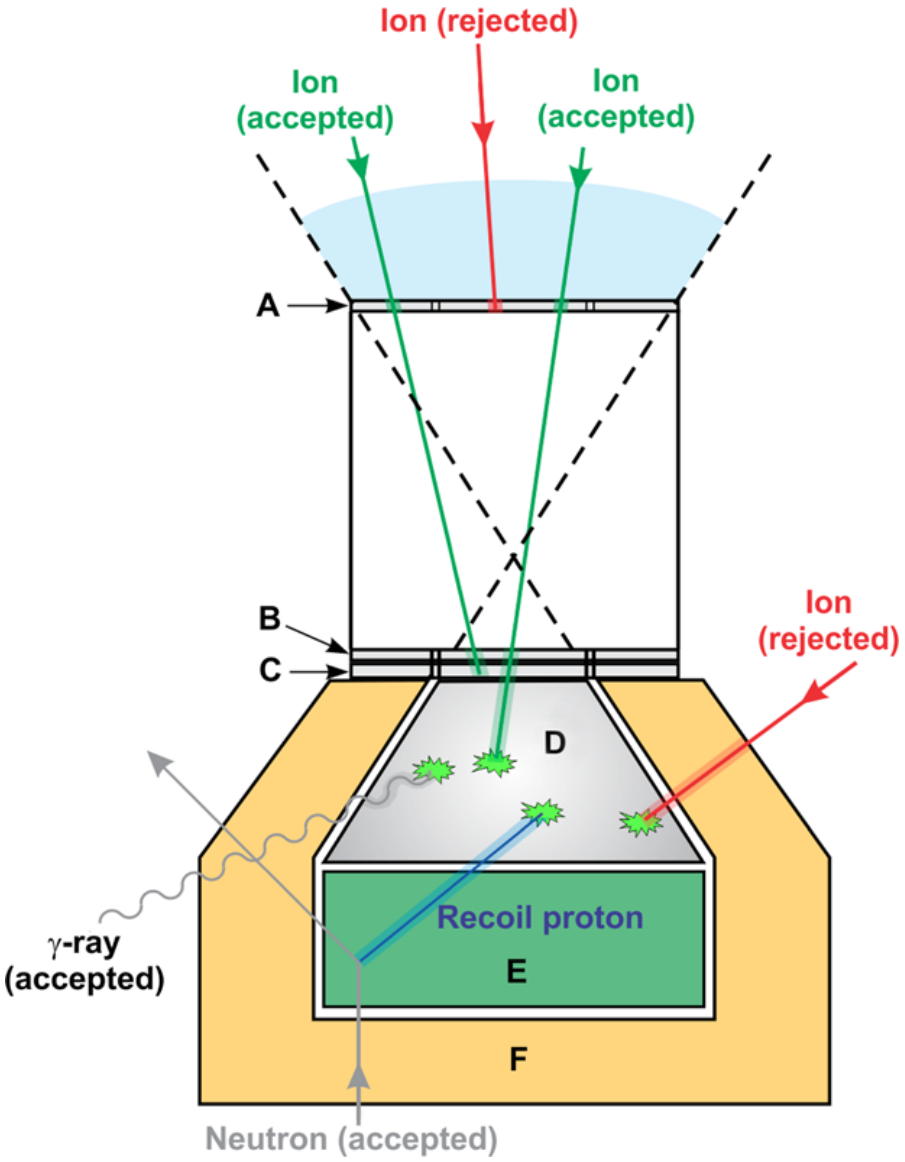

Figure 2.2: Drawing showing the nomenclature of detectors in the RAD Sensor Head (RSH). Accepted particle trajectories are shown in green, rejected trajectories are shown in red. Taken from Hassler et al. (2012).

3

THE MARTIAN ENVIRONMENT

The Martian surface is an interesting place to study because it is, in some ways, the planetary surface with conditions closest to those on the surface of Earth. With liquid water and higher atmospheric pressures thought to once exist on the surface of Mars, the conditions may even have been similar to those on Earth. However, the environment today shows some major differences, which will be highlighted and discussed in this chapter.

Some major differences include Mars' extreme aridity, its thin atmosphere composed almost exclusively of Carbon dioxide (CO_2), and its lack of a global magnetic field. This work concerns itself only with Gale crater, the region in which the Curiosity rover is currently operating. The observations, as of the writing of this thesis, cover the time range from 2012 to 2017.

First, the Martian radiation environment will be discussed, followed by a discussion of atmospheric conditions. Models used in this work and the data obtained from them will be presented.

3.1 THE MARTIAN RADIATION ENVIRONMENT

In this work, the term *Martian radiation environment* is taken to mean the environment of ionizing radiation that is present on Mars. This environment starts at the top of the atmosphere, reaching down to ground level and into the soil. It is made of primary particles entering the top of the atmosphere and the secondary particle cascades produced by these particles in the Martian atmosphere and soil. The source of the primary particles is the interplanetary radiation environment, i. e., the environment outside of the influence of any planetary or other bodies.

The interplanetary radiation environment, or, in short, the heliosphere, is filled with particles from different sources. Following Potgieter (2010), cosmic rays with energies from $1\,MeV\,nuc^{-1}$ up to $1 \times 10^{15}\,MeV\,nuc^{-1}$ can be classified as belonging to one of four different populations:

- Galactic Cosmic Rays (GCRs), which originate from supernovae and Active Galactic Nuclei (AGN) injecting the particles into the interstellar medium at velocities near the speed of light,

corresponding to energies above several $100\,MeV\,nuc^{-1}$ (e. g., Gaisser (1990), Berezhko (2008), Rieger and Mannheim (2000), and Osmanov, Rogava, and Bodo (2007)). The GCR particles consist of 98 % atomic nuclei, with most being Hydrogen, followed by Helium and other heavy elements (e. g., Gaisser (1990)), and 2 % electrons.

- Solar Energetic Particles (SEPs) are periodic events occurring on the surface of the Sun, which inject particles into the heliosphere. The sources are solar flares, Coronal Mass Ejections (CMEs) or shocks. The particles are mainly protons (e. g., Meyer (1985) and Mewaldt et al. (2012)) with energies ranging from about $1\,keV\,nuc^{-1}$ up to about $1\,GeV\,nuc^{-1}$. It should be noted that the energy spectrum of SEPs can be highly variable between different events.

- Anomalous Cosmic Rays (ACRs), which, according to Potgieter (2010), are widely assumed to be Pick-Up Ions (PUIs) that have been accelerated back into the heliosphere at the termination shock, although other acceleration mechanisms have been proposed, e. g., by Drake et al. (2010). Their energies range from $5\,MeV\,nuc^{-1}$ to $100\,MeV\,nuc^{-1}$.

- Jovian electrons are electrons accelerated up to $30\,MeV$ inside Jupiter's magnetosphere.

Still following Potgieter (2010), there are three factors protecting the Earth from incoming ionizing radiation. First, dynamic processes in the heliosphere and the Heliospheric Magnetic Field (HMF) modulate incoming GCR particle fluxes. Second, the Earth itself has a global magnetic field which is able to shield incoming particles. Third, Earth's atmosphere attenuates particle fluxes, e. g., by absorbing incoming GCR particles' energies .

The situation on Mars regarding the protection against ionizing radiation is very different. Heliospheric shielding is, of course, mostly identical to the situation on Earth. However, Mars lacks the global magnetic field that Earth has (Jacobs, 1979). As discussed by, e. g., Purucker et al. (2000) and Connerney et al. (2001), Mars has a strongly localized magnetic field, shown in Fig. 3.1 from Mars Global Surveyor (MGS) measurements. Notably, the location of Gale crater shows no relevant magnetic field. Since this work discusses only the situation as observed by the Curiosity rover inside Gale crater, the magnetic field will be assumed to not be present in any case. Also, the Martian atmosphere has a much lower column density than that of Earth, leading to a worse shielding of incoming particle fluxes on Mars.

Even though the Martian surface is less shielded than the surface of the Earth, protons still need an energy of $150\,MeV\,nuc^{-1}$ to reach the surface from the top of the atmosphere. Typically, only a small fraction

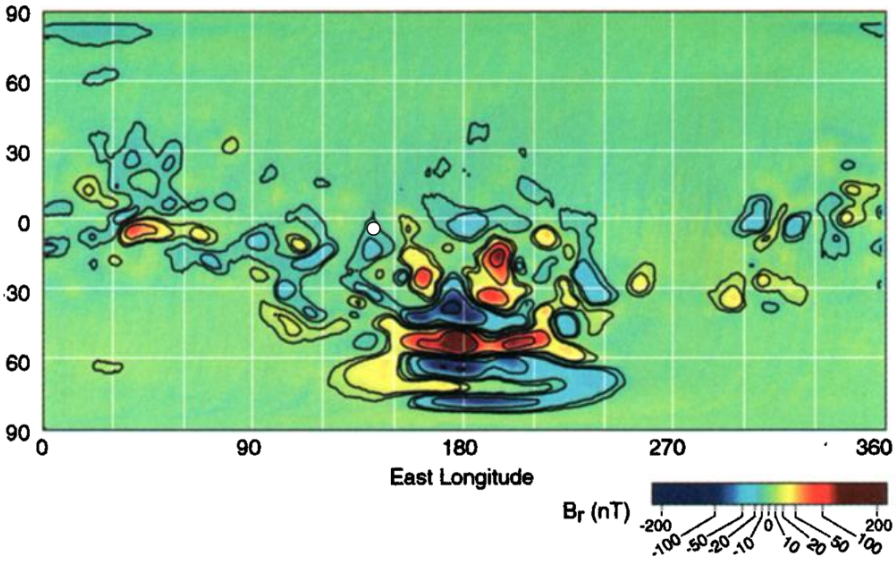

Figure 3.1: Map showing the radial magnetic field B_r on Mars from measurements performed by the Mars Global Surveyor (MGS) mission. The location of Gale Crater is marked by a white circle. Modified from Connerney et al. (2001).

of the particles emitted as SEPs have sufficient energies. SEPs events producing particles that reach the surface are also called Ground-Level Events (GLEs).

Most of the radiation environment on the Martian surface is produced by GCRs. In order to simulate the influence of GCR particles on the Martian radiation environment, the Badhwar-O'Neill 2010 (BO10) model is used. The model is described in O'Neill (2010). It is based on measurements made by, e. g., Advanced Composition Explorer (ACE)/Cosmic Ray Isotope Spectrometer (CRIS), Balloon-borne Experiment with Superconducting Spectrometer (BESS), High Energy Astronomy Observatory (HEAO) as well as other satellite and balloon measurements. The energy spectra are computed using the spherically symmetric Fokker-Planck equation to propagate the interplanetary GCR spectra according to diffusion, convection, and adiabatic deceleration. The outer boundary is described by the Local Interstellar Spectrum (LIS) at a distance of approximately 100 au. The Fokker-Planck equation uses a single parameter, Φ. This parameter describes the attenuation of the LIS by the current state of heliosphere. Φ carries units of Volt. A larger value of Φ leads to a lower GCR flux, since more energy is required for particles to penetrate from the LIS into the heliosphere. The BO10 model uses the sunspot number to compute the value of Φ. This has the advantage of being able to produce spectra for GCR particle fluxes for time periods outside of the data the BO10 model is based on, whereas spacecraft data may not be available. However, the calculation of Φ in the model has been calibrated against

Φ values as measured where spacecraft data overlap the sunspot measurements— i. e., Interplanetary Monitoring Platform - 8 (IMP-8) from 1974 to 1997 and ACE from 1997 to present. The spectra for GCR elements ranging from $Z = 1$ (Hydrogen) to $Z = 94$ (Plutonium) are available for all relevant values of Φ. For elements with virtually zero GCR flux ($Z \geqslant 29$), the BO10 scales the energy spectra for Silicon by relative abundance.

Since the modulation of the GCR is mostly due to the state of the heliospheric magnetic field, the modulation follows what is known as the solar cycle. This is a variation of the heliospheric magnetic field on a timescale of 11 years, overlaid by a 22 year cycle. These cycles are due to variations in the solar magnetic field, which switches its polarity each 11 years. According to Potgieter (2010), the 11 year cycle is the most important variability in the GCR flux, followed by the 22 year cycle, and other variabilities stated as being below 1 %.

In addition to the modulation by the global state of the heliosphere as described above, GCR particles are also influenced by local disturbances. These are mostly local enhancements of the heliospheric magnetic field, e. g., by a Co-rotating Interaction Region (CIR), or by a CME producing a short-term decrease in GCR flux known as a Forbush decrease (Forbush, 1938).

3.2 THE MARTIAN ATMOSPHERE AND SOIL

The Martian atmosphere is, in total, of much lower density than that of Earth. In addition, the pronounced differences in local height and ongoing dynamic processes in the atmosphere lead to a local ground pressure that is highly variable in both time and location. As mentioned before, the discussion in this section will be limited to the Mars Science Laboratory (MSL) landing site, Gale crater.

In general, the Martian atmosphere is composed of about 95 % CO_2, 2 % Argon and 2 % Nitrogen (e. g., Owen et al. (1977), Nier and Mcelroy (1977) or more recently Mahaffy et al. (2013)). The atmosphere has a scale height, which is the height at which the pressure drops by a factor of e, of approximately 10 km. It reaches up to a height of 200 km, at which point the exosphere begins.

Due to the large variations in local ground altitude, the ground-level pressure on the Martian surface is vastly different depending on the location. E. g., the highest point of the Martian surface, Olympus Mons, has an altitude of 21.2 km, while the lowest point, Hellas Basin, has an altitude of -7.2 km. Inside Gale crater, where the Curiosity rover is operating, ground-level pressure is approximately 800 Pa (Gómez-Elvira et al., 2014).

The Martian atmosphere is highly variable over time. Mars undergoes pronounced seasons as well as diurnal changes (Hess et al. (1980), McCleese et al. (2010)). The diurnal pressure cycle is driven

by illumination and has been described by, e. g., Rafkin et al. (2014). The main absorber of energy in the Martian atmosphere is the dust suspended in it. Under incoming solar illumination, the dust absorbs energy, leading to a heating of the atmosphere. This, in turn, leads to an expansion of the atmosphere column, bringing column mass density and thus pressure down. At night, the process reverses, leading to a diurnal cycle. This cycle leads to a variation of pressure on the order of 10 % inside Gale crater. It is worth noting that the diurnal pressure effect inside Gale crater (Gómez-Elvira et al., 2014) is enhanced when compared to earlier measurements made by the Viking landers (Hess et al., 1980).

The seasonal variations are driven by CO_2 evaporating from one polar cap and condensing onto the opposing polar cap. This seasonal cycle has often been observed, e. g., by Viking as described by Hess et al. (1980). A time series showing an exemplary view of the seasonal variation during one Mars year is shown in the upper panel of Figure 3.2, with the per-sol amplitude of the diurnal variation shown in the lower panel. A time series of the diurnal variation for four sols during the MSL mission is shown in Figure 3.3.

One feature of the Martian climate that has no Earth analogue are global dust storms. In a global dust storm, much of the Martian surface is covered by dust suspended in the atmospheric column.

These storms are known to occur during summer on the southern hemisphere. The mechanism by which such a dust storm is generated is complex and not yet fully understood. Factors leading to the formation of a global dust storm are examined in, e. g., Leovy, Zurek, and Pollack (1973), Leovy and Zurek (1979), and Zurek (1981) using observation data, or in, e. g., Haberle, Leovy, and Pollack (1982) and Wilson and Hamilton (1996) using simulations.

Generally, the conditions necessary for a global dust storm appear to only occur at perihelion. During that period, solar radiation is raised by 40 % compared to the aphelion. Leovy, Zurek, and Pollack (1973) suggest that the diurnal winds are not sufficient to raise dust, strong axially symmetric wind systems are needed for saltation. These wind systems can be initiated by strong temperature gradients at the edge of the southern polar cap during spring in the southern hemisphere. Combined with strong mass outflow due to sublimating CO_2 ice and katabatic winds from the polar cap, enough dust can be raised to first form a local dust storm. Other authors, e. g., Wang (2005), note that not all dust storms appear to originate from the polar region, and instead suggest that baroclinic instabilities at the edges of the polar vortex, as opposed to the mass transport of CO_2, generate the strong winds necessary to induce saltation. As a summary, the mechanisms by which a local dust storm evolves into a global one is poorly understood and still actively discussed today (Fenton, Geissler, and Haberle, 2007). It is likely to be a runaway effect, in which the

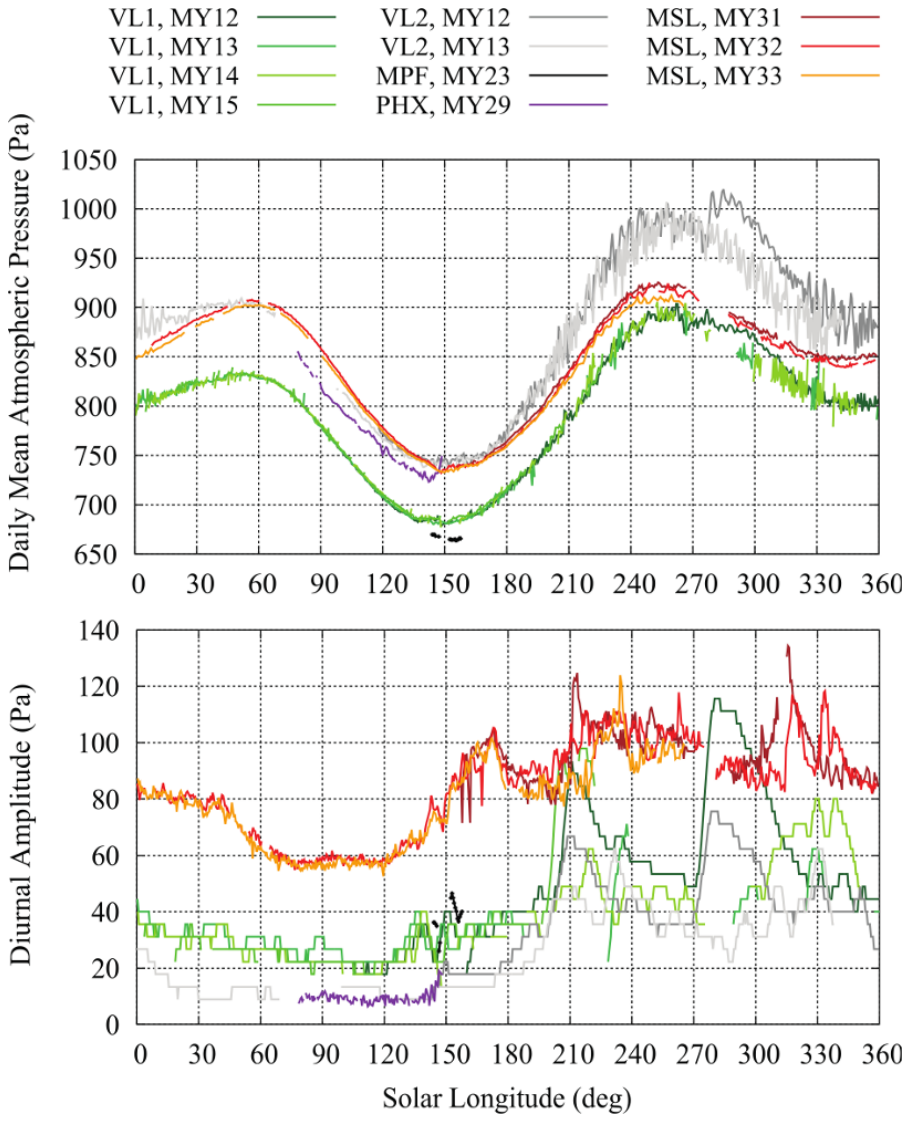

Figure 3.2: View of seasonal pressure variations (upper panel) and the amplitude of diurnal variations (lower panel) on the Martian surface. The data shown is from the missions Viking Lander 1 (VL1) and Viking Lander 2 (VL2), Mars PathFinder (MPF), Phoenix (PHX) and Mars Science Laboratory (MSL). Figure taken from Martínez et al. (2017).

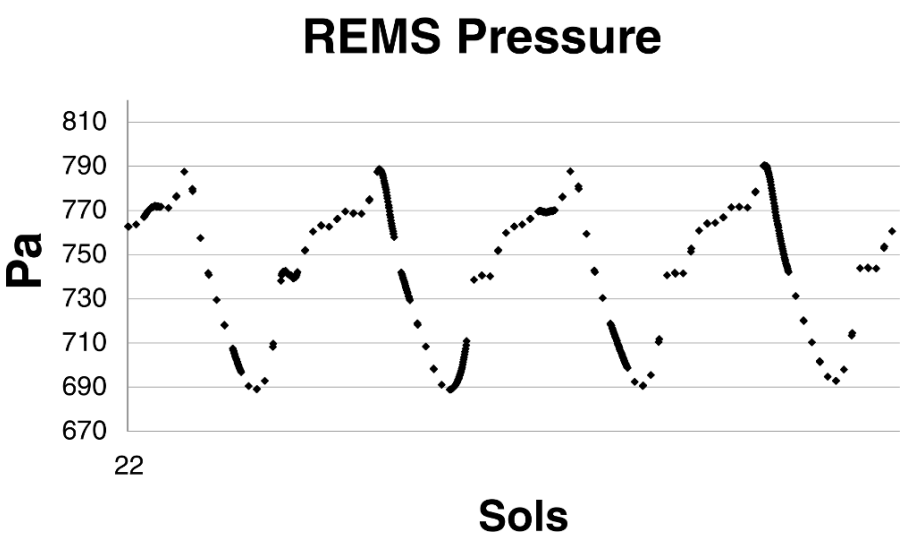

Figure 3.3: View of diurnal pressure variations observed by the Rover Environmental Monitoring Station (REMS) instrument onboard the Mars Science Laboratory (MSL) rover Curiosity. The figure shows data from three consecutive sols starting from sol 22. Figure taken from Rafkin et al. (2014).

increased absorption of solar radiation leads to higher atmospheric temperatures in the storm region, increasing the saltation of dust from the Martian surface until the storm has grown to global size. For the purpose of the work presented herein, the key aspect is that global dust storms occur with some regularity every few Mars years, although given the current understanding, their formation is not yet predictable.

A global dust storm has severe and lasting consequences for the Martian climate. Due to the visual opacity of the individual dust grains, the main absorber of solar radiation is the large volume of dust suspended in the atmosphere. This leads to a raise in atmospheric temperature and pressure in the atmosphere layers in which the dust is suspended, with a corresponding lower surface temperature due to the visual opacity and absorption of solar radiation in higher atmosphere layers. In Gurwell et al. (2005), the surface temperature is stated to drop by 20 K during the 2001 global dust storm. At the same time, the atmospheric temperature at mid altitudes rise by up to 30 K, while near-surface temperatures in the atmosphere remain unchanged. In contrast to a general description of the global effects, the individual effects of a global dust storm on the atmosphere column above a specific location on the Martian surface is hard to predict. Generally, a detailed knowledge of the three-dimensional dust distribution for a specific dust storm under investigation is needed to determine its local effects. It should be noted that the data in the Mars Climate Database (MCD) by itself is not sufficient to produce such a local

atmospheric profile. For that, an atmospheric simulation using the specific dust distribution needs to be performed, e. g., the General Circulation Model (GCM) used to produce the data stored in the MCD.

After a global dust storm has passed, surface albedo is locally increased due to deposition of light dust particles on the surface (Fenton, Geissler, and Haberle (2007), Leovy, Zurek, and Pollack (1973)). This albedo change influences Martian climate and weather, leading to colder surface temperatures in the areas with increased albedo. Globally, the albedo changes lead to an increase of surface temperature by about 0.65 K.

For the purpose of modeling particle transport within the Martian atmosphere, an altitude profile of its composition and density is needed. Here, a model of atmospheric conditions is used. While there are measurements available, those are by nature limited to the places and times when landers operated on the Martian surface. Also, while measured profiles of the atmosphere exist, those are only available when and where landers obtained measurements during their descent through the atmospheric column. Using a model allows for more flexibility in choosing location and time of the simulation and easier access to all relevant data. There are several models of the Martian atmosphere available, e. g., Mars-GRAM 2000 (Justus, James, and Bougher, 2002) and MCD (Lewis et al., 1999). Here, MCD version 5.0 is used. The reasons for this are twofold: First, the model is freely and easily available. Secondly, the model contains detailed data for a vast range of atmospheric conditions.

From a technical point of view, MCD is a database of climatological model run results. Model runs are validated by various available observations, made among others by MGS, Mars Odyssey, Mars Reconnaissance Orbiter (MRO), and the Mars Exploration Rovers (MERs). The database can provide an atmosphere model for different solar and atmospheric conditions. There are four different atmospheric conditions available in the database (Forget, Millour, and Lewis, 2012):

- Cold atmospheric conditions, based on the minimal observed dust opacity during Mars years 24-30.
- Warm atmospheric conditions, based on the maximal observed dust opacity during Mars years 24-30, except during global dust storms.
- "Climatology" atmospheric conditions, based on observations during Mars years 24, 26, 27, 29 and 30. These are years without global dust storms. This data set shows temporal and local variations in atmospheric dust distribution.
- Dust storm atmospheric conditions, with the dust opacity fixed at $\tau = 5$. This represents an extreme global dust storm.

Na_2O	MgO	Al_2O_3	SiO_2	SO_3	K_2O	CaO	TiO_2	Fe_2O_3
1.5 %	7.7 %	8.1 %	46.8 %	6.0 %	0.2 %	6.2 %	1.1 %	18.8 %

Table 3.1: Abundances of compounds in the Martian soil as measured by the Sojourner rover (Rieder (1997), McSween et al. (1999) and Bell et al. (2000)).

Here, a Mars year is defined as one Martian sidereal year, from the time Mars has a solar longitude of $L_s = 0°$ to the time it has completed one full orbit around the Sun, corresponding to $L_s = 360°$. As is commonly done, Mars year 1 is defined as starting with the incidence of $L_s = 0°$ on the 11th of April, 1955 (Clancy et al., 2000). Atmospheric heating above an altitude of 120 km depends on the influx of solar extreme Ultra- Violet (eUV) radiation (Forget, Millour, and Lewis, 2012). The MCD database provides data for three different solar eUV conditions:

- solar minimum,
- solar maximum, and
- solar average.

In the following, the combination of atmosphere and solar conditions will be called a *scenario*. If not otherwise noted, the scenario used represents the "climatology" atmospheric conditions with solar average eUV influx.

An atmosphere profile for particle transport modeling is obtained by reading out atmospheric composition and density from the Martian surface up to an altitude of 250 km, which is the maximum altitude covered by the MCD database. The values are requested specifying the location, time and scenario.

The last component of the Martian environment described here is the Martian soil. This work follows the parameters suggested in the Planetocosmics application used here for simulating particle transport within the Martian atmosphere (Desorgher, L.; Flückiger, E. O.; Gurtner, 2006). Planetocosmics uses composition and density data measured by the Alpha-Particle X-ray Spectrometer (APXS) instrument on the Sojourner rover landed on Mars by the Pathfinder mission. These are the default values used by the Planetocosmics application (Desorgher, 2005). The mission, as described in Rieder (1997), McSween et al. (1999) and Bell et al. (2000), found a mass density of $1.7\,g\,cm^{-3}$ for the Martian soil, with a composition as given in Table 3.1. The major component is Silicon dioxide, with Iron oxide accounting for the characteristic red color of the Martian soil.

4

SIMULATION OF IONIZING RADIATION

One of the scientific goals of the Radiation Assessment Detector (RAD) instrument is the validation of particle transport codes, and the work presented in this thesis aims to contribute to that process. Multiple simulations have been performed for this, including ones for situations observed during the cruise phase of the Mars Science Laboratory (MSL) mission and on the Martian surface, as described in Chapter 6. Another aspect is the prediction of situations that have not occurred during the MSL mission to date, e. g., simulations of the influence of global dust storms on the Martian radiation environment. These simulations are described in Chapter 5. The particle transport codes and programs used in these simulations are described in the following.

In general, one of two different approaches are mainly used in order to simulate the transport of ionizing particles in matter. The first approach is a deterministic code, the other one is a Monte Carlo code.

As an example for a deterministic code, the properties of the High-Charge and Energy Transport (HZETRN) code are described (Wilson et al., 1995). As described therein, the code solves the Boltzmann transport equation for the particles transported using a one-directional and one-dimensional approximation. More modern versions include improvements in those approximations, e. g., including bidirectional neutron transport (Wilson et al., 2014). The primary interaction with particles in a material is with the electrons of the atoms making up the material. The direct interaction of nuclei is relatively infrequent compared to the interaction with the electrons. However, those interactions cannot be neglected due to the high amount of energy transferred in them, thus they have to be considered. Additional approximations are made in HZETRN, e. g., neglecting the fragmentation of target nuclei and taking the angular distribution in a space radiation environments as isotropic.

A particle transport code using the Monte Carlo method employs a stochastic approach to model the transport of particles. The initial spatial, angular and energy distributions of the particles are given by the user and randomly sampled by the transportation code to generate the primary particles. Then, each particle is transported through the simulation geometry. During that transportation, physical processes acting on the particle are executed according to their probability, i. e.,

the mean free path length of the particle in the given density and composition of its surrounding material.

In general, a deterministic code that solves transport equations instead of tracking individual particles is faster to calculate. However, the code has to rely on some assumptions and approximations for its modeling. A Monte Carlo code is generally much slower due to the large number of primary particles needed to be calculated in order to obtain a statistically sound sampling of the primary particle spectra. Since a Monte Carlo code generally tries to directly model the interaction processes between the particles and the target materials, it is in principle only limited by the knowledge of these interaction processes and their cross sections. It can thus be considered a more direct modeling approach.

The following two sections explain the Geant4 Monte Carlo simulation code (Section 4.1) and the Planetocosmics application (Section 4.2) used extensively throughout this work in some detail.

4.1 THE GEANT4 SIMULATION CODE

The Monte Carlo code used in this work is the Geometry and Tracking version 4 (Geant4) code developed at European Organization for Nuclear Research (CERN). It is a flexible, all-purpose particle transport code. Geant4 is widely employed, e. g., for the modeling of CERN instruments (e. g., Prokopovich et al. (2010)), for dosimetry simulations in radiation therapy (e. g., Spiga et al. (2007)) and, of course, for particle transport simulations in planetary and space physics and instrumentation (e. g., Köhler et al. (2011)). In particular, the modeling of particle transport within a planetary atmosphere is provided by the Planetocosmics application described in section 4.2.

In the following, a general overview of the principles of Geant4 is given in order to explain features and terms used throughout this work. The explanation closely follows Agostinelli et al. (2003). For more in-depth explanations, the reader is referred to the original publication.

As suggested by the name, the process of particle transport modeling using the Geant4 code consists of three distinct parts: Geometry, transportation and tracking.

The term geometry is used here to describe the layout and properties of volumes, representing physical objects, in the simulation. Each object is defined by its shape and a material of arbitrary chemical composition and density. The shape is constructed either from various primitive shapes using boolean operations, or by reading a Computer Aided Design (CAD) file. The simulation geometry can be arbitrarily complex, in practice the only limit is the memory available on the machine executing the simulation.

The process of moving the particle through the simulation geometry while executing the different physical processes is called transportation. The particle is moved in small, discrete steps. When choosing the length of each step, Geant4 chooses the minimum length of the following:

- The mean free path of the particle being transported as described by the various physical processes available.
- The distance to the nearest geometrical boundary on the particles' path.
- The maximum step length set by the user for the particle being transported.

At the end of each step, the post-step action for the particle is executed. If the step is limited by a physical process, i. e., the first possibility listed above, the model describing that process is executed on the particle.

Tracking is the process of providing information on particle interactions and energy deposits along the track of the particle within the simulation geometry. In particular, the tracking process also gives the amount of energy deposited in the sensitive detectors hit by the particle along its track, if any.

The physical processes that are available for a given particle are selected by the user. In Geant4, the list of processes that can act on particles is called a physics list. It is possible to either construct a completely custom physics list, or to use or modify a list that has been pre-constructed by the Geant4 software authors. A physical process can act on a particle in one of three distinct phases. For particles that are at rest, nuclear decay processes can be executed. For moving particles, processes can be executed along the length of the step made by the particle. This is used for processes that continuously modify the particles energy, e. g., for Cherenkov radiation and Bremsstrahlung. The last class of processes are the post-step processes executed at the end of one particle propagation step for moving particles. Possible processes for this are particle-particle interactions, production of secondary particles or a particle decay. The pre-constructed physics lists are organized by the different classes of physical interactions between particles, e. g., electromagnetic, hadronic or optical interactions. For the simulations in this work, only the electromagnetic and hadronic interactions have been used. Optical interactions have been omitted since they only apply to photons with wavelengths in the optical range, far larger than those produced by Galactic Cosmic Ray (GCR) particle interactions.

The models used to represent the processes in a given physics list belong to one of three categories:

- Data driven models use measured particle interaction data to compute the outcome of a given interaction. They are considered to be the best approach in modeling, although they depend on sufficient data being available for accurately describing the physical process being modeled.

- Parameterized models are extrapolations of measured particle interaction data. They can be used to either extend the range of the data or to interpolate between insufficient data points.

- Theory-based models use purely theoretical predictions or descriptions of interaction processes for interactions or energies where measurements are insufficient or non-existent.

4.2 THE PLANETOCOSMICS APPLICATION

Planetocosmics is a Geant4 application developed at the University of Bern under an European Space Agency (ESA) contract. Originally based on Geant4 version 8.3, this work uses a Planetocosmics version which has been updated to use the more up-to-date Geant4 version 9.6.p02. The updated version has been provided by D. Matthiä (e. g., Matthiä et al. (2016)). The features of Planetocosmics have been explained in Desorgher, L.; Flückiger, E. O.; Gurtner (2006) and especially in Desorgher (2005).

The Planetocosmics application aims to simplify several aspects of simulating the radiation environments on planetary surfaces and inside planetary magnetospheres. Namely, it automatically generates a geometry model for Geant4 based on an atmosphere and a soil model, it sets up generation of primary particles based on a user-provided input spectrum, and it automates the generation of particle energy spectra at user-defined altitudes both in the atmosphere and the soil. It also allows various studies related to planetary magnetospheres, such as a simulation of cutoff rigidity. However, since Mars has no global magnetic field and the local field inside Gale crater is negligible for particles relevant to the work presented here, as has been discussed in Section 3.1, this is not of importance for the present work.

Planetocosmics, as used for the studies presented here, needs to be provided with two different sets of input data. First, it needs a density and composition profile of the Martian atmosphere. Secondly, it needs an energy spectrum of the primary GCR radiation as present on top of the Martian atmosphere.

The model of the Martian atmosphere is provided by the Mars Climate Database (MCD), which has previously been described in Section 3.2. Atmospheric density and composition is read out from the maximum altitude available in the model, $h = 250\,\mathrm{km}$, down to ground level in steps of $\delta h = 100\,\mathrm{m}$. All components present in the MCD model atmosphere are used for Planetocosmics. The dust

composition is taken from soil composition values measured by the Sojourner rover, which is the default value for Planetocosmics. It has been found that the composition and density of the Martian soil does not influence the Planetocosmics simulation results of this work. Thus, the soil is represented by a block of SiO_2 at a mass density of $\rho_{soil} = 1.7\,g\,cm^{-2}$ unless otherwise noted. The block has a vertical thickness of $l = 100\,m$. This thickness is sufficient to include the Pfotzer maximum (Dartnell et al., 2007) and thus the majority of secondary particle production.

The primary particle energy spectra at the top of the atmosphere are provided by the Badhwar-O'Neill 2010 (BO10) GCR model, unless otherwise noted.

Since computation time for a given simulation run was not a concern, the physics lists used were generally chosen to provide the best possible accuracy. The electromagnetic interactions are loaded from the `emstandard_opt4` physics list. Hadronic interactions are provided by the `QGSP_BIC_HP` list, with ion hadronic interactions provided by the Particle and Heavy Ion Transport code System (PHITS) model (Niita et al., 2006). PHITS is an external Quantum Molecular Dynamics (QMD) model integrated into the application. Additionally, options enabling nuclear electromagnetic and muon interactions as well as synchrotron radiation have been enabled.

The Planetocosmics application has been validated for simulations of the Martian environment against other particle transport models and data taken by the RAD instrument (Matthiä et al., 2016). Generally, good agreement between the measurements and predictions by Planetocosmics have been found. However, Matthiä et al. (2016) investigate only dose rates and energy spectra of particles. The work presented in this thesis addresses other aspects of the Martian radiation environment, namely particle flux directionality and the influence of atmospheric dust, and attempts to validate the simulation results with observations made by the RAD instrument.

5

INFLUENCE OF GLOBAL DUST STORMS ON RAD MEASUREMENTS

One of the most drastic changes in the Martian atmosphere is the occurrence of global dust storms, which usually occur during summer on the southern hemisphere. In such a storm, the amount of dust suspended in the atmosphere is dramatically increased, leading to changes in the temperature, density and pressure profile of the atmosphere. These changes are more fully described in Section 3.2. This chapter investigates the question of how these dramatic atmospheric changes influence the Martian radiation environment.

The question of this influence has been addressed prior in other works. In particular, Norman, Gronoff, and Mertens (2014) investigated this using the High-Charge and Energy Transport (HZETRN) simulation code. Their results can be summarized as predicting no relevant changes on the ground-level radiation environment. At higher altitudes, around 100 km, they predict an increase in ionization rate. This increase can lead to an increased absorption of electromagnetic waves, which might lead to a degradation in space-to-ground communications or radar signals through the atmosphere. The primary energy spectra used by Norman, Gronoff, and Mertens (2014) in their investigation are Galactic Cosmic Ray (GCR) spectra of hydrogen, helium, carbon, nitrogen, oxygen, silicon and iron. In addition, they use several hydrogen spectra for exemplary Solar Energetic Particle (SEP) events. While the enhancements in ionization rate are more pronounced for the SEP spectra, no ground-level changes are predicted for any of them.

One of the scientific goals of the Radiation Assessment Detector (RAD) instrument is the verification of particle transport codes for the Martian environment. The work presented here aims to aid in this goal by comparing simulations of the surface radiation environment on Mars during a global dust storm with observations made by the RAD instrument during times of enhanced dust content, i. e., atmospheric opacity. The simulations are performed using the Planetocosmics application, which is based on the Geometry and Tracking version 4 (Geant4) code. Atmospheric data for the simulations is taken from Mars Climate Database (MCD), and some aspects of atmospheric profiles from a database of simulations, e. g., MCD, is discussed.

This part of the thesis has been prepared as a manuscript for submission to the journal "Space Weather and Space Climate". It has been reproduced below. The authors' own contribution to the manuscript is 80 %.

submitted to **Journal of Space Weather and Space Climate**

The Influence of Global Dust Storms and Atmospheric Dust Enhancements on the Martian Radiation Environment

J. K. Appel[1], J. Guo[1], D. Matthiä[2], S. Rafkin[3], H. Lohf[1], R. F. Wimmer-Schweingruber[1], B. Ehresmann[3], C. Zeitlin[4], D. M. Hassler[3], D. E. Brinza[5], E. Böhm[1], S. Böttcher[1], C. Martin[1], S. Burmeister[1], G. Reitz[2], A. Posner[6], and G. Weigle[7]

[1] Institute for Experimental and Applied Physics, University of Kiel, Germany.
e-mail: appel@physik.uni-kiel.de

[2] Institute of Aerospace Medicine, Deutsches Zentrum für Luft- und Raumfahrt, Köln, Germany.

[3] Southwest Research Institute, Boulder, Colorado, USA

[4] Leidos Innovations Corporation, 2625 Bay Area Blvd., Houston, TX, USA 77058.

[5] Jet Propulsion Laboratory, California Institute of Technology, Pasadena, CA, USA.

[6] NASA Headquarters, Science Mission Directorate, Washington DC, USA.

[7] Big Head Endian, LLC, Burden, Kansas, USA.

ABSTRACT

The occurrence of global dust storms is a unique feature of Mars. These storms lead to drastic changes in the Martian atmosphere. Here, we investigate the influence of these changes on the surface radiation environment through particle transport model calculations performed using the Planetocosmics code for Galactic Cosmic Rays (GCR). We compare the results obtained from our calculations with measurements performed by the Radiation Assessment Detector (RAD) on board the Curiosity rover on the Martian surface. RAD measurements were corrected for the influence of seasonally varying atmospheric pressure. While the models predict no significant changes during global dust storms, RAD measurements show a weak but significant correlation between dose rate and opacity. Extrapolating this trend to opacities typical of a global dust storm, the RAD measurements would indicate a significantly higher ($\tilde{2}1\%$) dose rate during such conditions. The discrepancy between model results and measurements is not fully understood. While we could exclude the influence global, large-scale heliospheric modulation as the cause, the dose-rate variability caused by the small-scale modulation by corotating interactions regions (CIRs) may contribute to this apparent correlation.

Key words. particle transport modeling – Mars – global dust storm – Radiation Assessment Detector – GCR

1. Introduction

On August 6, 2012, the NASA Mars Science Laboratory (MSL) rover Curiosity (Grotzinger et al., 2012) landed on the Martian surface. Since then, it has been operating inside Gale crater, where it is exploring the past and present habitability of Mars. An important part of assessing habitability is the knowledge of the radiation environment. Characterizing this environment is the goal of the Radiation Assessment Detector (RAD, Hassler et al., 2012), which was co-developed by the University of Kiel and the Southwest Research Institute.

The Martian radiation environment is influenced by different factors, including the Martian atmosphere itself (Rafkin et al., 2014; Guo et al., 2017). The atmosphere is a highly dynamic environment with changes on multiple timescales, e.g., the diurnal pressure variations, and pronounced seasonal changes (Hess et al., 1980). One unique feature of the Martian atmosphere is the occurrence of global dust storms. These storms occur stochastically every few Mars years and influence the atmospheric structure, opacity and temperature in a dramatic way. In order to fully understand the influence of these atmospheric changes on the Martian radiation environment, it is important to investigate the changes expected to occur during a global dust storm. Here, we analyze a period of enhanced atmospheric dust content, as evidenced by a corresponding enhancement of atmospheric opacity in measurements made by the Curiosity Rover's Mastcam (Martínez et al., 2017). We assess the relationship between measurements of the radiation environment on the Martian surface and the atmospheric opacity measured at Gale Crater over a time frame of 1000 sols and found a moderate and positive correlation between the opacity, which is enhanced during a global dust storm, and the dose rate measured on the surface. This is however not predicted by the modeled results and would require further investigations. One possible explanation is the strong systematic variability of measured dose rates during the time period of enhanced opacity which is very likely due to small-scale heliospheric modulation by corotating intereaction regions (CIRs) in the solar wind.

2. Atmosphere and Particle Transport Models

The Martian atmosphere is, in general, composed of about 95 % Carbon dioxide, 2 % Argon and 2 % Nitrogen (e.g., Owen et al. (1977), Nier and Mcelroy (1977), Mahaffy et al. (2013)). It is significantly less dense than Earth's atmosphere. Due to the extremely variable topography of Mars, ground-level atmospheric pressure is also highly variable. Inside Gale crater, where the Curiosity rover is operating at an altitude of approximately -4.4 km compared to the Mars Orbiter Laser Altimeter (MOLA) datum, ground-level pressure has been measured in a range between 750 Pa and 950 Pa (Gómez-Elvira et al., 2014) over a Martian year.

Global dust storms are only known to occur at perihelion, which occurs in the southern hemisphere spring. The exact set of conditions necessary for the formation of a global dust storm is not completely understood. Leovy et al. (1973) suggest that strong katabatic winds from the southern polar cap are needed, together with the global mass transport of carbon dioxide, which evaporates from the southern polar cap and recondenses onto the northern polar cap. This combination can first generate a local dust storm, which then can escalate to a global storm. Other research, e.g., Wang

(2005), suggests that not all storms originate from the polar region, and that baroclinic instabilities at the edges of the polar vortex, not the carbon dioxide mass transport, generate the strong winds that lift the dust. For the purpose of this study, the important aspect is that Martian global dust storms are known to occur somewhat regularly, although not predictably, every few Mars years.

During a global dust storm, the Martian atmosphere changes significantly. Dust is lifted to and suspended up to altitudes of between 50 km and 150 km. Visually, this dramatically increases the opacity, almost completely obscuring the Martian surface as seen from space. Dust is the main absorber of solar radiation in the Martian atmosphere, thus leading to increased heating in the layers to which the dust has been lifted (Gurwell et al., 2005).

The response of the Martian atmosphere to the increased radiative heating from dust is complex. Generally, the heating leads to atmospheric expansion in the upper layers. At the same time, the dust enhancement leads to a shadowing of the surface, which lowers surface temperatures. As a result of these effects, the atmospheric column is perturbed by the global dust storm in both vertical and horizontal directions. The resulting effect on surface atmospheric pressure and atmospheric column mass at a given location depends on the precise dust structure of the storm in both the horizontal and vertical, as well as additional factors, e.g., local topography. Detailed studies of the effect of global dust storms on surface meteorology have been performed for the Viking Lander 1 and 2 observations by, e.g., Leovy and Zurek (1979); Zurek (1981), and using simulations by, e.g., Haberle et al. (1982); Wilson and Hamilton (1996).

A detailed study of radiation transport depends on a reasonably detailed knowledge of the three-dimensional distribution of dust in the atmosphere for any given storm under study, because that dust is know to cause perturbations in the atmospheric column mass. Here, we attempt a general study of the influence of a global dust storm on the Martian surface radiation environment. We use the Mars Climate Database (MCD) (Forget et al., 2006) as a source of generalized atmospheric conditions during a global dust storm. The MCD is a database of climate model results for a wide variety of conditions. The results cover the Martian globe during the full annual cycle and for a set of various dust conditions. Some of those conditions, including the ones modeling the average Martian atmosphere, are based on observations made by various probes. Others are based on artificial conditions. In particular, the global dust storm scenario is modeled using an artificially fixed opacity of $\tau = 5$ for the seasons during which a global dust storm is known to occur. While such a model gives a reasonable general overview of the atmospheric conditions during a global dust storm, we emphasize that it is not a representation of the atmospheric column above a particular location on the Martian surface during a particular global dust storm. The particle transport simulations we perform here are sensitive in particular to the surface pressure, which in turn is sensitive to the exact horizontal and vertical distribution of dust during any particular storm. Simulations of atmospheric conditions using an artificially fixed opacity tend to not reproduce surface atmospheric pressure well when compared to a particular global dust storm.

We show Mars Orbiter Laser Altimeter (MOLA) altitude versus atmospheric temperature, pressure, density, shielding depth and composition, as derived from the MCD, in Fig. 1, both during a global dust storm and under non-storm conditions. We will call any such representation of altitude vs. some other value a profile. E.g., altitude plotted vs. atmospheric pressure will be called an atmospheric pressure profile.

In order to model the transport of particles through the Martian atmosphere, a profile of its density and composition as a function of atmospheric depth, or altitude, is needed. For an assessment of the

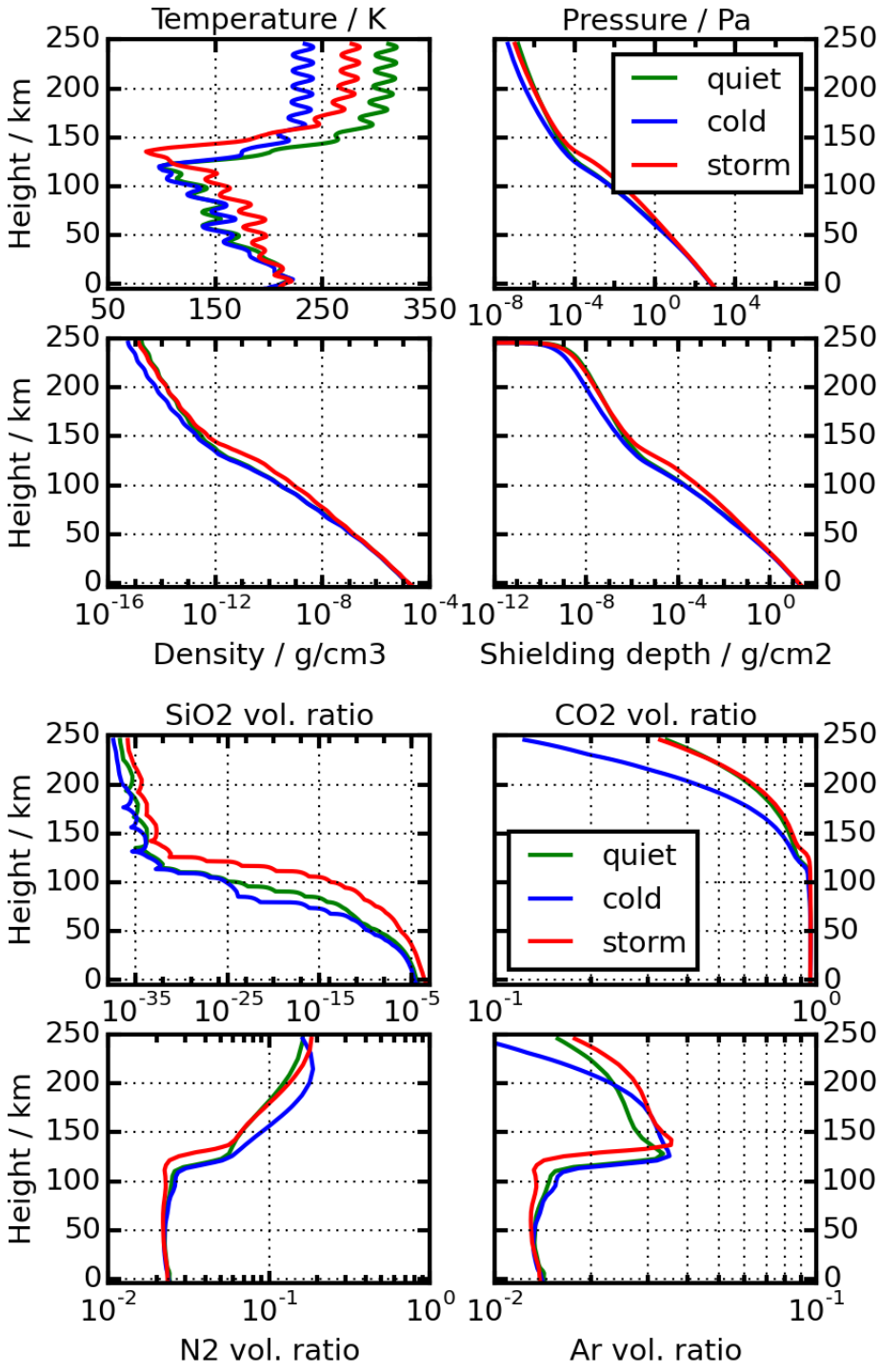

Fig. 1. Comparison of the three atmospheric profiles used in this work. The first two rows show an overview of temperature, pressure, density and shielding depth profiles. The bottom row shows a profile for the three major atmospheric gases in the right frame and SiO_2 as representative for dust content in the left frame for the three model scenarios.

influence of global dust storms, profiles are needed for conditions both during a global dust storm and under normal conditions. Here, we use the MCD version 5.0 (Forget et al., 2006) to obtain those profiles. All profiles are read out for altitudes above the local surface of between 250 km to 0 km in steps of 100 m. We consistently used the position of Gale crater (latitude 4.49° S, longitude 137.42° E, see Grotzinger et al. (2012)) to read out the profiles in order to allow later comparisons with RAD measurements. The other MCD readout parameters are left to their default settings, with the exception of enabling high-resolution MOLA topography, and including both small and large scale perturbations in the atmosphere. It is noted that the LMD General Circulation Model lacks the spatial resolution to capture the topographic relief of Gale Crater and the strong diurnal amplification of the diurnal pressure signal (e.g., Richardson and Newman (2018)).

We use the Planetocosmics application (Desorgher, L.; Flückiger, E. O.; Gurtner, 2006) to calculate particle transport through the atmospheric column. Planetocosmics is a Monte Carlo model based on the Geometry And Tracking (Geant) code developed at CERN (Agostinelli et al., 2003). In order to support more up-to-date particle interaction models, the Planetocosmics application used here has been updated to use Geant version 4.9.6. For modeling electromagnetic interactions, the `emstandard_opt4` physics list is used. Models for hadronic interactions are taken from the `QGSP_BIC_HP` physics list. The ion hadronic interactions are calculated using the Particle and Heavy Ions Transport code System (PHITS) (Niita et al., 2006), which has been integrated into Planetocosmics, replacing the respective ion hadronic processes.

3. Dose Rate Measurements Using the RAD Instrument

RAD is a compact instrument designed to characterize the Martian radiation environment. It has been fully described in Hassler et al. (2012). Here, we focus on describing the features used in this investigation.

The instrument consists of a stack of three silicon Solid State Detectors (SSD), which are called detectors A, B and C. Detector D is a truncated hexagonal pyramid of thallium- doped Cesium Iodide (CsI(Tl)). Detectors E and F are made of Bicron BC-432m plastic scintillator material, which has a density similar to biological tissue. Detector F is used as an anti-coincidence detector. For this investigation, we focus on the RAD dosimetry measurements in detector E. Detectors A through C are sensitive to charged particles, while detectors D and E are sensitive to both charged and neutral particles. RAD offers dosimetry measurements using detectors B and E. By using the measurement provided by detector E, we gain a more complete measurement of dose rate by including both charged an neutral particles.

4. Model Setup

While we use a set of input data for the model that allow an approximation of the radiation environment as measured on the surface by the RAD instrument, an exact calculation of RAD-measured dose rates is challenging due to the instrument-specific properties and the complex shielding geometry of the rover body. Therefore, we focus on the relative changes between the different atmospheric scenarios modeled in this study.

We model the radiation transport under three different atmospheric conditions, described in Forget et al. (2006). First, we use the “quiet” scenario provided by MCD. This is a baseline dust

scenario depicting long-term average conditions. The second scenario we considered is the "cold" MCD scenario. This scenario depicts extremely clear and dust-poor conditions based on data from the Viking landers. The last scenario was the "dust" scenario, depicting a global dust storm. For this scenario, the MCD uses an artificially fixed atmospheric optical depth of $\tau = 5$.

A comparison of the three atmospheric profiles used is shown in Fig. 1. Although the figure only shows the three major atmospheric gases, we use the full composition including all trace gases made available through MCD, namely CO_2, N_2, Ar, CO, O, O_2, O_3, H, and H_2. Similarly, the figure only shows SiO2 as a representative for dust content. In our model calculations, the full chemical composition of dust is used, taken from the standard soil model in Planetocosmics (Desorgher, 2005), which is based on observations made by the Pathfinder/Sojourner mission (Rieder (1997), McSween et al. (1999), Bell et al. (2000)). The surface atmospheric pressures in the three atmospheric profiles are $P_q = 960.96\,\mathrm{Pa}$, $P_c = 954.50\,\mathrm{Pa}$, and $P_q = 998.41\,\mathrm{Pa}$ for the quiet, cold and storm scenarios, respectively.

We use the Badhwar-O'Neill 2010 (BO10) model to calculate the Galactic Cosmic Ray (GCR) spectra on the top of the Martian atmosphere. This is one of the standard models used for obtaining GCR spectra, described in detail in O'Neill (2010). The following short description summarizes the main points of that work.

The model provides free space energy spectra for GCR particles, ranging from an atomic weight of $Z = 1$ to $Z = 94$. Here, free space energy spectrum is to be understood as the energy spectrum of particles outside the magnetosphere of Earth, but inside the heliosphere. The spectra are computed using the spherically symmetric Fokker-Planck equation, with the Local Interstellar Spectra (LIS) at the boundary of the heliosphere, at approximately 100 AU, as a boundary condition. The spectra are fitted to measurements obtained by a multitude of instruments, including all available observations of GCR particle energy spectra from 1955 to 2010.

The model uses one input parameter, the solar modulation Φ. Φ is in units of magnetic rigidity, in volts, and was derived from the International Sunspot Number. The modulation parameter Φ is a depiction of solar activity, where larger values of Φ correspond to lower GCR particle fluxes. Any given value of Φ describes the state of the heliosphere at a given time, and can be used to derive all particle spectra available within the model.

Here, we use a value of $\Phi = 650\,\mathrm{MV}$, read out for a distance of 1 AU. We chose this value of Φ because it is near the average observed during the MSL mission in the time frame of this investigation, i.e., the years 2012-2015. While the orbit of Mars has a semi-major axis of approximately 1.5 AU, the radial gradient of the GCR flux is small, as shown by e.g. Gieseler and Heber (2016). Thus, we use the particle energy spectra at 1 AU for our calculations.

We use hydrogen, helium, carbon, nitrogen, oxygen, silicon and iron as primary particles. These particles are selected to represent the major constituents of the GCR. All particle spectra presented in Fig. 2 are downward-directed particle spectra modeled with BO10, i.e., they have been integrated over a solid angle of 2π.

In addition to the primary spectra described above, we also performed model calculations using hydrogen and helium particle spectra for Φ values of $\Phi = 400\,\mathrm{MV}$ and $\Phi = 1500\,\mathrm{MV}$ in order to investigate solar solar modulation scenarios on the Martian radiation environment during a global dust storm.

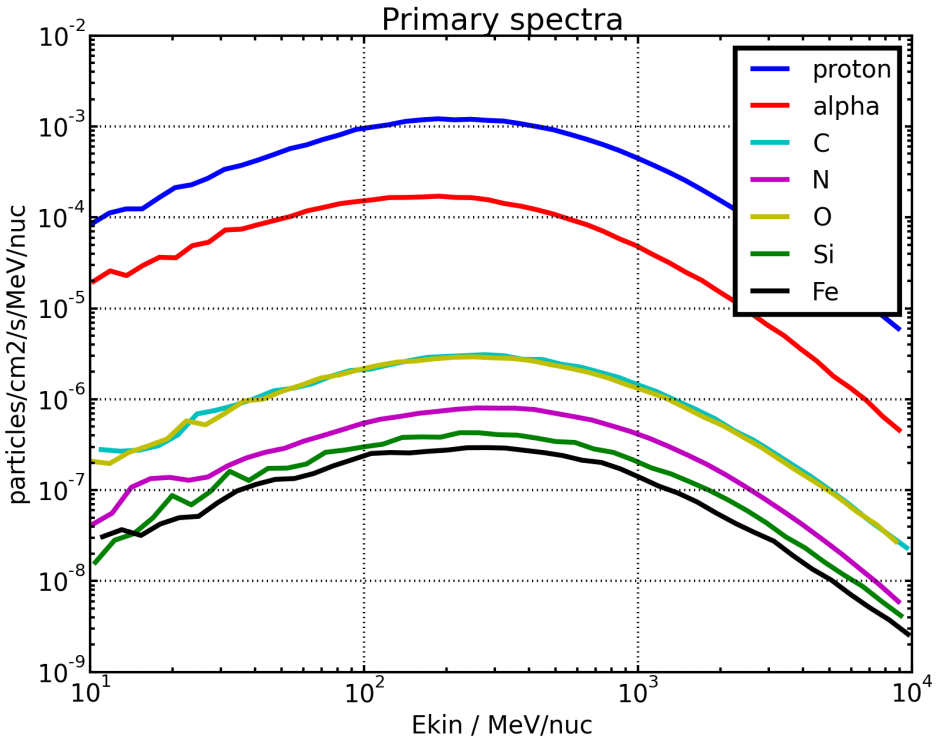

Fig. 2. Primary spectra used in the model calculations. Shown are the primary GCR spectra for hydrogen, helium, carbon, nitrogen, oxygen, silicon and iron, as generated by the Planetocosmics application on top of the atmosphere at an altitude of 250 km above the surface.

5. Model Results

The Planetocosmics calculations do not directly output the ionization rate. Instead, a profile of energy deposition vs. altitude above ground is computed. From that, the ion production rate, or ionization rate, P, is computed as

$$P = \frac{Q}{W} \tag{1}$$

where Q is the total energy influx and W is the energy per ion pair produced. Here, we use units of $[P] = \frac{1}{\mathrm{cm^2\,s}}$, $[Q] = \frac{\mathrm{eV}}{\mathrm{cm^2\,s}}$ and $[W] = \mathrm{eV}$. If we take r, $[r] = \frac{\mathrm{J}}{\mathrm{kg\,s}}$, as the energy deposition rate, and ρ, $[\rho] = \frac{\mathrm{g}}{\mathrm{cm^3}}$, as the mass density, then we can compute the ion production rate as

$$P = 6.24 \cdot 10^{15}\,\frac{r\,\rho}{W} \tag{2}$$

with units of $[P] = \frac{1}{cm^3\,s}$. We use a value of $W = 35\,\mathrm{eV}$ as currently accepted in aeronomy (Norman et al., 2014).

We use two different depictions of dose rate, a profile of energy deposition over atmospheric depth, and the dose rate computed at fixed altitudes above the surface of 0 km, i.e., the Martian surface, and 100 km. Of these, the dose rate computed at an altitude of 0 km corresponds most closely to the RAD measurements, which have been aquired on the surface. The energy deposition

profiles are data products that are produced directly by Planetocosmics. They take into account any energy deposition made by any particle in the atmospheric gas at all altitudes. In addition, we compute the dose rate from the particle energy spectra output by Planetocosmics. The two dose rate depictions are not directly comparable, since they are computed for different materials. While the direct calculation by Planetocosmics gives the dose rate in the atmospheric gas, we compute the dose rates from particle spectra, which is more comparable to the dose measurement in the RAD plastic detector E, for tissue. In addition, the dose rate computed from particle spectra does not have as high a spatial, i.e., altitude, resolution as the energy deposition profiles directly produced by Planetocosmics. However, it allows us to select the particle types, solid angle coverages, energies, and target material, that are used in computing the dose rate.

Particle energy spectra are output by Planetocosmics as a series of fluxes F_N in N energy bins $E = \{E_1, E_2, \ldots, E_N\}$, where F_n are the particle fluxes in energy bin E_n. With the energy loss per path length dx of the particles as $\frac{dE}{dx}$ and ρ the mass density of the material in which the dose rate is computed, the dose rate is $D = \frac{F\frac{dE}{dx}}{\rho}$. With units of $[F] = \frac{1}{m^2\,s}$, $\left[\frac{dE}{dx}\right] = \frac{J}{m}$, and $[\rho] = \frac{kg}{m^3}$, the units of the dose rate become $[D] = \frac{Gy}{s}$.

In general, we use the particle energy spectra for stable isotopes from Hydrogen to Iron, as well as electrons, positrons, pions, muons, neutrons, and gamma rays, to compute the dose rate. Each particle is described by a set of upward and downward directed energy spectra, covering a solid angle of 2π per downward and upward spectrum, respectively. We use both spectra for each particle species, resulting in a dose rate computed for the full solid angle of 4π.

All dose rates were computed for particle energies between 1 $\frac{\text{MeV}}{\text{nuc}}$ and 10 $\frac{\text{GeV}}{\text{nuc}}$ (Guo et al., 2018). We derived the values of $\frac{dE}{dx}$ from Geant4 calculations performed for particles in the respective target material. All dose rates reported by us in this investigation for altitudes of 0 km and 100 km were computed in tissue, as defined by the Geant4 material `G4_TISSUE_SOFT_ICRP`. This is in contrast to the Planetocosmics-produced atmospheric dose rate profiles, which are computed in the atmospheric mixture for each altitude contained within the profile.

We show the ground-level spectra of downward particle flux in Fig. 3 for all three atmospheric conditions. Note that there is no change in particle spectra depending on the atmosphere condition observable for the particles shown and evaluated here, with the particle flux varying by less than 2% betweeen both the quiet and the storm as well as the cold and the storm scenarios. We show the energy deposition profiles computed for the GCR scenario in Fig. 4. The topmost chart in Fig. 4 shows the atmospheric dose rate profile. The dose rate shows a maximum at an altitude around 25 km for all atmospheric scenarios. The global dust storm scenario shows a slightly enhanced dose rate for altitudes between 50 km and 80 km. The ground-level dose rate remains unchanged between the three atmospheric scenarios considered here.

The ionization rate is shown in the lower chart of Fig. 4. The quiet and cold atmosphere scenarios show no discernible graphical variation between each other, however, the global dust storm scenario shows a higher ionization rate between altitudes of 50 km to 100 km. This change is driven by the changes in atmospheric density, shown in the top of Fig. 1. Due to higher dust loading at these altitudes, temperature and density are increased when compared to the non-storm scenarios. Since the ionization rate depends on the atmospheric density, the changes in density drive the changes in ionization rate.

We show the influence of different solar modulation scenarios in Fig. 5 and Tab. 1.

Table 1. Ground-level dose rates for different solar modulation conditions and atmospheric dust scenarios. Dose rates have been computed for particle energies between 1 $\frac{\text{MeV}}{\text{nuc}}$ and 10 $\frac{\text{GeV}}{\text{nuc}}$.

Φ/MV	quiet / μGy/day	cold / μGy/day	storm / μGy/day
400	$1.34{\cdot}10^{+02}$	$1.34{\cdot}10^{+02}$	$1.33{\cdot}10^{+02}$
650	$1.10{\cdot}10^{+02}$	$1.10{\cdot}10^{+02}$	$1.10{\cdot}10^{+02}$
1500	$3.96{\cdot}10^{+01}$	$3.97{\cdot}10^{+01}$	$3.95{\cdot}10^{+01}$
surface pressure / Pa	960.96	954.50	998.41

Table 2. GCR induced dose and ionization rates for all three atmosphere scenarios at an altitude of 0 km, meaning ground level at Gale crater, and 100 km. The rates have been computed for particle energies between 1 $\frac{\text{MeV}}{\text{nuc}}$ and 10 $\frac{\text{GeV}}{\text{nuc}}$.

dose rates / μGy/day

	quiet	cold	storm
100 km	$1.05{\cdot}10^{2}$	$1.05{\cdot}10^{2}$	$1.05{\cdot}10^{2}$
0 km	$1.00{\cdot}10^{2}$	$1.00{\cdot}10^{2}$	$9.93{\cdot}10^{1}$

ionization rates / 1/cm^3

	quiet	cold	storm
100 km	$5.56{\cdot}10^{-5}$	$5.39{\cdot}10^{-5}$	$1.78{\cdot}10^{-4}$
0 km	$3.27{\cdot}10^{+0}$	$3.25{\cdot}10^{+0}$	$3.39{\cdot}10^{+0}$

Surface pressure / Pa

	quiet	cold	storm
0 km	960.96	954.50	998.41

Table 3. Ratios between storm and quiet atmosphere scenarios for GCR induced dose and ionization rates at an altitude of 0 km, corresponding to ground level at Gale crater, and 100 km. The ratios have been computed as the rate for the storm scenario divided by the corresponding quiet scenario rate for particle energies between 1 MeV and 10 GeV.

	dose ratio	ionization ratio
100 km	$1.01{\cdot}10^{+0}$	$3.19{\cdot}10^{+0}$
0 km	$9.89{\cdot}10^{-1}$	$1.03{\cdot}10^{+0}$

5.1. Dose and Ionization Rates at ground level and altitudes of 100 km

Tab. 2 lists dose and ionization rates caused by GCR for all three atmosphere conditions at altitudes of 100 km and 0 km. We show a comparison between the global dust storm and the quiet scenario in Tab. 3. Here, we computed the ratio of dose and ionization rates between the global dust storm and the quiet atmospheric scenario. It is evident that the dose rates are mostly unchanged.

Ground-level ionization rates are unchanged for GCR. However, at an altitude of 100 km during a global dust storm, we observe ionization rates that are increased by a factor of 3, mainly as a result of the increased atmospheric density.

6. RAD Dose Rate Observations During Dust Enhancements

The RAD instrument provides the first, and to date only, measurements of the radiation environment on the Martian surface. Therefore, it is uniquely suited to validate the results of the model calculations shown above. Since Curiosity landed on Mars on August 6, 2012, there have been periods of enhanced dust activity, including a global dust storm. The analysis presented here is restricted to dust activty prior to the global dust storm. The enhancement in atmospheric dust content is evidenced by the enhancements in atmospheric opacity, τ, observed by Mastcam on the Curiosity rover, published by Martínez et al. (2017). Fig. 6 shows the first 1000 sols of opacity data published, with one sol being the duration of a solar day on Mars, approximately 24 hours and 39 minutes.

As described earlier in Rafkin et al. (2014) and Guo et al. (2015), the dose rate measured by the RAD instrument is influenced by different factors, with the major one being atmospheric pressure. In an attempt to isolate the influence of opacity on the dose rate, we use the correlation found in Guo et al. (2017) to subtract the influence of atmospheric pressure and solar modulation on the dose rate measurements. In Guo et al. (2017), the correlation between dose rate and atmospheric pressure is derived as

$$D' = D - \kappa(P - P_0) \tag{3}$$

where D and D' are the measured and pressure-detrended dose rates, respectively, κ is the proportionality factor between dose rate and pressure changes, which is an approximated linear function for small perturbations, and P and P_0 are pressure and an arbitrarily chosen reference pressure, which, however, should be close to the typically measured pressure value. This will yield a dose rate D' adjusted to a constant pressure value of P_0. We use the *Phi*-dependent $\kappa = \kappa(\Phi)$ as established in Guo et al. (2017) for correcting the dose rate measured in the E detector of the RAD instrument. The reference pressure was chosen as $P_0 = 739.46$ Pa here, representing the first value of the data set.

There is an additional correlation for the influence of the solar modulation Φ presented in Guo et al. (2015). We chose not to perform this correction for the analysis we present here. First, the dose dependence on Φ was quantified using 26-sol binned dose rate data correlated with Φ values measured at Earth. This method includes large uncertainties. Given the poor knowledge of daily Φ values at Mars, and the fact that they could be different from those at Earth, this could introduce a bias when applying the modulation correction to the daily dose rate. Second, the variability of Φ is relatively low for the time frame we investigate here, so necessary corrections will also be small. Even if this appears to rule out the large-scale modulation of galactic cosmic rays as a cause for the correlation between dose rate and opacitiy, this must not necessarily be true for small-scale heliospheric modulation, as ist duscussed in more detail in the Discussion (Sec. 7).

We show the pressure data used for correcting the dose rate measurements, as well as solar modulation data for the same time frame, in Fig. 7. Both data sets are averaged per sol (Guo et al., 2015). All RAD dose rate data presented and used for this analysis have been processed to remove the influence of pressure as described above.

We here define enhanced dust activity as a period where the opacity is increased with respect to preceding or following years. The period in question is highlighted in Fig. 6. For analyzing the relationship between dose rate and opacity, we first compute the mean value per sol for each data set during the first 1000 sols of the MSL mission. Fig. 8 shows the resulting dose rate D',

detrended for the influence of atmospheric pressure, and atmospheric opacity τ data sets. We show the relationship of pressure-detrended dose rate D' dose rate in the E detector versus the atmospheric opacity in Fig. 9. A weak but statistically significant correlation is apparent in the data, as is also clear when examining the correlation coefficients. For dose rate measured in detector E and opacity, the Pearson correlation coefficient is $R_P = 0.306$ with a p-value of $p_P = 9.66 \cdot 10^{-5}$. The Spearman correlation coefficient for dose measured in detector E and opacity is $R_S = 0.285$ with a p-value of $p_S = 2.98 \cdot 10^{-4}$.

7. Discussion and Conclusion

We modeled ground level particle spectra on Mars under three different atmospheric conditions, including a global dust storm. We used incoming GCR particle spectra on top of the atmospheric column for the generation of primary particle spectra in our simulations.

The modeled ground-level particle spectra did not change between any of the three atmosphere scenarios. This result can be expected when looking at the mass added to the atmosphere column by the dust content in it. During a global dust storm, the opacity is strongly impacted by the dust content to the point where the atmosphere becomes opaque. Still, the total dust mass in the atmosphere has a negligible direct impact on the radiation transport. Fig. 1 shows this in the bottom panel. Even at ground level, where the mixing ratio of dust has its maximum, dust contributions are negligible when compared to the major atmospheric components. The major increase in dust content during a global dust storm event occurs at altitudes between 70 km and 120 km. Here, the dust content is increased by a factor of about 10^4 when compared with the non-storm quiet and cold conditions. However, this is still a negligible increase compared to the gaseous atmospheric column mass.

Profiles of dose rate in the atmospheric column material computed for GCR, as shown in Fig. 4, show a maximum around 25 km altitude. The dose rate drops sharply below that point until ground level. We obtained dose rate profiles for all three atmosphere scenarios. These are a cold scenario with an almost dust-free atmosphere, a quiet scenario, with an average amount of dust in the atmosphere, and a global dust storm scenario. The difference between the global dust storm and the quiet scenarios, as well as between the global dust storm and the cold scenarios, is below 2%. The difference in surface atmospheric pressure between the quiet and global dust storm atmospheric scenarios is on the order of $\Delta P \approx 40$ Pa. This pressure difference accounts for the difference in dose rates between the simulated quiet and global dust storm conditions.

We performed all dose rate calculations using a lower energy limit of 1 $\frac{\text{MeV}}{\text{nuc}}$. Particles at such low energies are easily stopped by even small amounts of shielding. The dose rates we report here should therefore not be used for estimating dose rates in a shielded environment. The low-energy particles we include contribute heavily to the dose rate and would be shielded by material such as spacecraft, spacesuits or even clothing. For GCR doses, using a higher energy limit of 10 $\frac{\text{GeV}}{\text{nuc}}$ only includes a relatively small part of the full GCR spectra. Coupled with the fact that we only use a select range of primary particles, this leads to an unrealistically low GCR dose rate. Again, the values we report should not be used for purposes such as radiation protection.

The ionization rate profiles are computed from the dose rate profiles in the atmospheric column material. Because of the almost constant dose rate profile for altitudes below 100 km, the ionization rate profile is dominated by the atmospheric mass density profile. While the dust in the atmosphere does not influence the mass distribution, it does influence atmospheric heating, and thus leads to

perturbations of the atmosphere column, as discussed in Sec. 2. This is clearly visible in Fig. 1, which shows temperature, pressure and mass density increases between altitudes of approximately 60 km to 100 km. These changes drive the increase of the ionization rate observed for the global dust storm scenario in comparison to both the quiet and cold scenarios. Peak ionization is predicted at ground level.

Fig. 5 shows that there is no effect of solar-rotation averaged solar modulation Φ on the sensitivity of modeled dose rates on the atmospheric dust content.

We compared the modeled results with observations made by the RAD instrument during the first 1000 sols of the MSL mission. While the model suggests no influence of the atmospheric opacity on the ground-level dose rate, we find a weak but statistically significant correlation between the two in RAD data. We found a correlation coefficient of $R_P = 0.306$ between the dose rate measured in detector E of the RAD instrument and the atmospheric opacity. Our model calculations predict that the dose rate on ground level is independent of dust content, as represented by atmospheric opacity, for the range of opacities observed during the MSL mission. However, the observations show a weak but statistically significant correlation. The increased opacity observed in the data, with a value of $\tau \approx 1.5$, is still small when compared to values during a global dust storm, where the opacity can rise to values of $\tau \approx 5$. The correlation we found predicts a dose rate of $D' = 270.5\,\mu$Gy/day for $\tau = 5$, compared to a dose rate of $D' = 223.6\,\mu$Gy/day for $\tau = 1$. This corresponds to an increase in dose rate by approximately 21 % during a global dust storm. In order to reliably confirm or reject the existence of a correlation between dose rate and atmospheric opacity, further study using a larger range of opacity values is required.

We chose not to correct the daily dose rate for the influence of the solar modulation Φ in the current analysis due to the high uncertainty of applying the solar modulation at Mars using daily Φ values measured at Earth. Also, when comparing the value of Φ during the time of enhanced atmospheric opacity with the preceding Martian year, as visible in Fig. 7, it can be seen that the average value of Φ is slightly higher during the atmospheric dust enhancement than the preceding Martian year. During the atmospheric dust enhancement period, the average value for Φ is $\overline{\Phi} = 614.5$ MV, with a value of $\overline{\Phi} = 449.8$ MV during the preceding year. Since an increase in Φ leads to a decrease in dose rate D' (Guo et al., 2015), we expect a decrease in dose rate for this time. However, as visible in Fig. 9, the dose rate is increased. While this suggests that there seems to be an effect of atmospheric opacity on ground-level dose rate, we want to emphasize again that the influence of solar modulation has not been corrected for, unlike the influence of atmospheric pressure. Despite the argument made above regarding different average values for Φ during different Mars years, it is entirely possible that the effect we observe in Fig. 9 is due to random correlations between atmospheric opacity and solar modulation on short time scales. While correcting the influence of the solar modulation in the observational data would help to clarify this point, establishing the relationship between solar modulation Φ and pressure-corrected dose rate D' has proven challenging. More work is needed to reliably confirm or deny the correlation we observe here.

Small scale heliospheric modulations are dynamic, transient and location dependent. While Φ values are measured at Earth, Mars could be at a heliospheric location that is exposed to different heliospheric structures such as stream interaction regions (SIRs) and Coronal mass ejections (CMEs). SIRs turn to co-rotate with the Sun and are seen at different heliospheric longitudes with a time delay dependent on the longitudes of the observer. CMEs are transient solar eruptions propagating radially outwards and they modulate the galactic cosmic rays mainly locally along their

passage. Thus its influence on modulation potential at different observers in the heliosphere could be rather different.

A possible influence on the dose rate measurements is the instrument temperature. We have investigated this influence and found that the instrument temperature varies between 13 °C and 19 °C for the time frame under investigation. We have not found a correlation between instrument temperature and measured dose rate. The dose rate measurements were performed using the E detector of RAD, which is made of a plastic scintillator material known to have a stable scintillation light output for the temperature range we observe here.

We use atmospheric profiles generated by the MCD for our simulations to represent generalized atmosphere conditions during a Martian global dust storm. However, as discussed in Sec. 2, the effect of a global dust storm on the atmospheric surface pressure and column mass at a given location depends heavily on the 3-D atmospheric structure of dust and the location on the planet. Since this is not taken into account in the MCD atmosphere data, the simulation results we present here may not be completely representative of the actual period of dust content enhancement contained in our analysis. The MCD atmosphere data shows a difference in surface pressure between the quiet and global dust storm scenarios of $\Delta P_{sim} \approx 40\,\mathrm{Pa}$, with the surface pressure higher in the global dust storm atmosphere profile. The REMS data during the period of enhanced dust content shows a decrease in surface pressure of $\Delta P_{REMS} \approx 10\,\mathrm{Pa}$. In our analysis, we attempt to correct for the effect of pressure in RAD observational data based on previous analyses. Even if it were not corrected, the pressure difference in the REMS data cannot account for the observed correlation between dose rate and atmospheric opacity.

Finally, close inspection of Fig. 8 shows that the time period of enhanced opacity (shaded in grey around sol 800) exhibits strong variability of the dose rate measurements. This time period coincides with the time period where the Sun showed large equatorward coronal holes which drove strong corotating interaction regions (CIRs) in the solar wind. Such structures are known to modulate the GCR at small scales. It is possible that their phasing relative to the opacity enhancement roundt this time conspires to produce the unexpected but statistically significant correlation between dose rate and opacity. After all, 'correlation does not imply causation'.

The analysis we present here is limited by the availability of opacity data. Once these have been extended to a longer time period, ideally including the 2018 global dust storm on Mars, a re-analysis of this apparent correlation should be performed. On the modeling side, the 3-D distribution of dust and the resulting atmopspheric profiles for the particular dust storms should be taken into account.

Acknowledgements. RAD is supported by NASA (HEOMD) Mars Science Laboratory Mission and Science Investigation, under JPL subcontract #1273039 to Southwest Research Institute and in Germany by DLR and DLR's Space Administration grant numbers 50QM0501 and 50QM1201 to the Christian Albrechts University, Kiel. Part of this research was carried out at the Jet Propulsion Laboratory, California Institute of Technology, under a contract with the National Aeronautics and Space Administration.

In particular, we would like to extend sincere gratitude to Jeff Simmonds, Ashwin Vasavada and Joy Crisp at JPL, Gale Allen, Michael Meyer, Chris Moore, Victoria Friedensen at NASA HQ, and Heiner Witte at DLR in Germany for their unwavering support of RAD over the years.

The RAD instrument data used in the analysis presented here are available in the NASA Planetary Data System at http://ppi.pds.nasa.gov/search/view/?f=yes&id=pds://PPI/MSL-M-RAD-2-EDR-V1.0

References

Agostinelli, S., J. Allison, K. Amako, J. Apostolakis, H. Araujo, et al. Geant4—a simulation toolkit. *Nuclear Instruments and Methods in Physics Research Section A: Accelerators, Spectrometers, Detectors and Associated Equipment*, **506**(3), 250–303, 2003. 10.1016/S0168-9002(03)01368-8. 2

Bell, J. F., H. Y. McSween, J. A. Crisp, R. V. Morris, S. L. Murchie, et al. Mineralogic and compositional properties of Martian soil and dust: Results from Mars Pathfinder. *Journal of Geophysical Research: Planets*, **105**(E1), 1721–1755, 2000. 10.1029/1999JE001060. 4

Desorgher, L. PLANETOCOSMICS Software User Manual. *Tech. rep.*, Physikalisches Institut, University of Bern, Switzerland, 2005. 4

Desorgher, L.; Flückiger, E. O.; Gurtner, M. The PLANETOCOSMICS Geant4 application. In 36th COSPAR Scientific Assembly. Beijing, 2006. 2

Forget, F., E. Millour, and S. Lebonnois. The new Mars climate database. In Second workshop on Mars atmosphere modelling and observations, 2006. 2, 2, 4

Gieseler, J., and B. Heber. Spatial gradients of GCR protons in the inner heliosphere derived from Ulysses COSPIN/KET and PAMELA measurements. *Astronomy & Astrophysics*, **589**, A32, 2016. 10.1051/0004-6361/201527972. 4

Gómez-Elvira, J., C. Armiens, I. Carrasco, M. Genzer, F. Gómez, et al. Curiosity's rover environmental monitoring station: Overview of the first 100 sols. *Journal of Geophysical Research: Planets*, **119**(7), 1680–1688, 2014. 10.1002/2013JE004576. 2

Grotzinger, J. P., J. Crisp, A. R. Vasavada, R. C. Anderson, C. J. Baker, et al. Mars Science Laboratory Mission and Science Investigation. *Space Science Reviews*, **170**(1-4), 5–56, 2012. 10.1007/s11214-012-9892-2. 1, 2

Guo, J., T. C. Slaba, C. Zeitlin, R. F. Wimmer-Schweingruber, F. F. Badavi, et al. Dependence of the Martian radiation environment on atmospheric depth: Modeling and measurement. *Journal of Geophysical Research: Planets*, **122**(2), 329–341, 2017. 10.1002/2016je005206. 1, 6, 6

Guo, J., C. Zeitlin, R. F. Wimmer-Schweingruber, T. McDole, P. Kühl, J. C. Appel, D. Matthiä, J. Krauss, and J. Köhler. A Generalized Approach to Model the Spectra and Radiation Dose Rate of Solar Particle Events on the Surface of Mars. *AJ*, **155**, 49, 2018. 10.3847/1538-3881/aaa085, 1705.06763, URL http://adsabs.harvard.edu/abs/2018AJ....155...49G. 5

Guo, J., C. Zeitlin, R. F. Wimmer-Schweingruber, S. Rafkin, D. M. Hassler, et al. Modeling the Variations of Dose Rate Measured By RAD During the First MSL Martian Year: 2012-2014. *The Astrophysical Journal*, **810**(1), 24, 2015. 10.1088/0004-637X/810/1/24, 1507.03473. 6, 6, 7, 7

Gurwell, M. A., E. A. Bergin, G. J. Melnick, and V. Tolls. Mars surface and atmospheric temperature during the 2001 global dust storm. *Icarus*, **175**(1), 23–31, 2005. 10.1016/j.icarus.2004.10.009. 2

Haberle, R. M., C. B. Leovy, and J. B. Pollack. Some effects of global dust storms on the atmospheric circulation of Mars. *Icarus*, **50**(2-3), 322–367, 1982. 2

Hassler, D. M., C. Zeitlin, R. F. Wimmer-Schweingruber, S. Böttcher, C. Martin, et al. The Radiation Assessment Detector (RAD) Investigation. *Space Science Reviews*, 2012. 10.1007/s11214-012-9913-1. 1, 3

Hess, S. L., J. A. Ryan, J. E. Tillman, R. M. Henry, and C. B. Leovy. The annual cycle of pressure on Mars measured by Viking Landers 1 and 2. *Geophysical Research Letters*, **7**(3), 197–200, 1980. 10.1029/GL007i003p00197. 1

Leovy, C. B., and R. W. Zurek. Thermal tides and Martian dust storms: Direct evidence for coupling. *Journal of Geophysical Research*, **84**(B6), 2956, 1979. 10.1029/jb084ib06p02956. 2

Leovy, C. B., R. W. Zurek, and J. B. Pollack. Mechanisms for Mars dust storms. *Journal of the Atmospheric Sciences*, **30**(5), 749–762, 1973. 10.1175/1520-0469(1973)030¡0749:MFMDS¿2.0.CO;2. 2

Mahaffy, P. R., C. R. Webster, S. K. Atreya, H. Franz, M. Wong, et al. Abundance and Isotopic Composition of Gases in the Martian Atmosphere from the Curiosity Rover. *Science (New York, N.Y.)*, **341**(July), 263–266, 2013. 10.1126/science.1237966. 2

Martínez, G. M., C. N. Newman, A. D. Vicente-Retortillo, E. Fischer, N. O. Renno, et al. The Modern Near-Surface Martian Climate: A Review of In-situ Meteorological Data from Viking to Curiosity. *Space Science Reviews*, 2017. 10.1007/s11214-017-0360-x. 1, 6, 6, 8, 9

McSween, H. Y., S. L. Murchie, J. A. Crisp, N. T. Bridges, R. C. Anderson, et al. Chemical, multispectral, and textural constraints on the composition and origin of rocks at the Mars Pathfinder landing site. *Journal of Geophysical Research: Planets*, **104**(E4), 8679–8715, 1999. 10.1029/98JE02551. 4

Nier, A. O., and M. B. Mcelroy. Composition and structure of Mars' upper atmosphere results from the neutral mass spectrometers on Viking 1 and 2. *Journal of Geophysical Research*, **82**(28), 4341–4349, 1977. 10.1029/JS082i028p04341. 2

Niita, K., T. Sato, H. Iwase, H. Nose, H. Nakashima, and L. Sihver. PHITS—a particle and heavy ion transport code system. *Radiation Measurements*, **41**(9-10), 1080–1090, 2006. 10.1016/j.radmeas.2006.07.013. 2

Norman, R. B., G. Gronoff, and C. J. Mertens. Influence of dust loading on atmospheric ionizing radiation on Mars. *Journal of Geophysical Research: Space Physics*, **119**(1), 452–461, 2014. 10.1002/2013JA019351. 5, A.1, A.1, A.2, A.1, A.1

O'Neill, P. Badhwar-O'Neill 2010 Galactic Cosmic Ray Flux Model —Revised. *IEEE Transactions on Nuclear Science*, **57**(6), 3148–3153, 2010. 10.1109/tns.2010.2083688. 4

Owen, T., D. K. Biemann, J. R. Rushneck, D. E. Biller, W. Howarth, and A. L. Lafleur. The composition of the atmosphere at the surface of Mars. *Journal of Geophysical Research*, **82**(28), 4635–4639, 1977. 10.1029/JS082i028p04635. 2

Rafkin, S. C., C. Zeitlin, B. Ehresmann, D. M. Hassler, J. Guo, et al. Diurnal variations of energetic particle radiation at the surface of Mars as observed by the Mars Science Laboratory Radiation Assessment Detector. *Journal of Geophysical Research: Planets*, **119**, 1345–1358, 2014. 10.1002/ 2013JE004525. 1, 6

Richardson, M. I., and C. E. Newman. On the relationship between surface pressure, terrain elevation, and air temperature. Part I: The large diurnal surface pressure range at Gale Crater, Mars and its origin due to lateral hydrostatic adjustment. *Planetary and Space Science*, 2018. 10.1016/j.pss.2018.07.003. 2

Rieder, R. The Chemical Composition of Martian Soil and Rocks Returned by the Mobile Alpha Proton X-ray Spectrometer: Preliminary Results from the X-ray Mode. *Science*, **278**(5344), 1771–1774, 1997. 10.1126/science.278.5344.1771. 4

Sheel, V., S. A. Haider, P. Withers, K. Kozarev, I. Jun, S. Kang, G. Gronoff, and C. Simon Wedlund. Numerical simulation of the effects of a solar energetic particle event on the ionosphere of Mars. *Journal of Geophysical Research*, **117**(A5), A05,312–A05,312, 2012. 10.1029/2011JA017455. A.2, A.1

Townsend, L. W., D. L. Stephens, J. L. Hoff, E. N. Zapp, H. M. Moussa, T. M. Miller, C. E. Campbell, and T. F. Nichols. The Carrington event: Possible doses to crews in space from a comparable event. *Advances in Space Research*, **38**(2), 226–231, 2006. 10.1016/j.asr.2005.01.111. A.1, A.1

Wang, H. Relationship between frontal dust storms and transient eddy activity in the northern hemisphere of Mars as observed by Mars Global Surveyor. *Journal of Geophysical Research*, **110**(E7), 2005. 10.1029/2005je002423. 2

Wilson, R. J., and K. Hamilton. Comprehensive model simulation of thermal tides in the Martian atmosphere. *Journal of Atmospheric Sciences*, **53**, 1290–1326, 1996. 10.1175/1520-0469(1996)053¡1290:CMSOTT¿2.0.CO;2, URL http://adsabs.harvard.edu/abs/1996JAtS...53.1290W. 2

Zurek, R. W. Inference of dust opacities for the 1977 Martian great dust storms from Viking Lander 1 pressure data. *Icarus*, **45**(1), 202–215, 1981. 10.1016/0019-1035(81)90014-2. 2

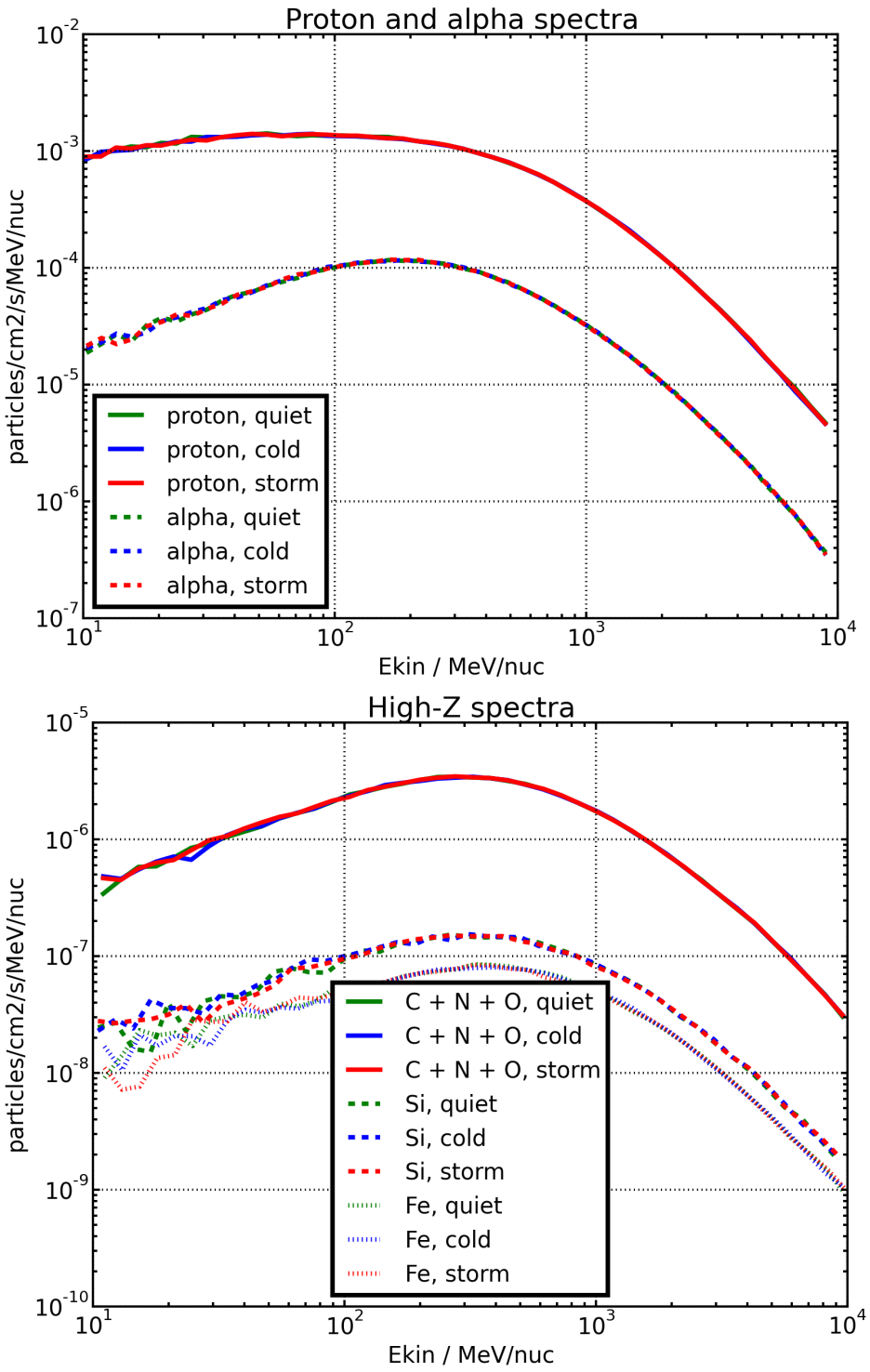

Fig. 3. Resulting GCR ground-level spectra. The top figure shows hydrogen and helium spectra, the bottom figure shows carbon, oxygen, silicon and iron spectra.

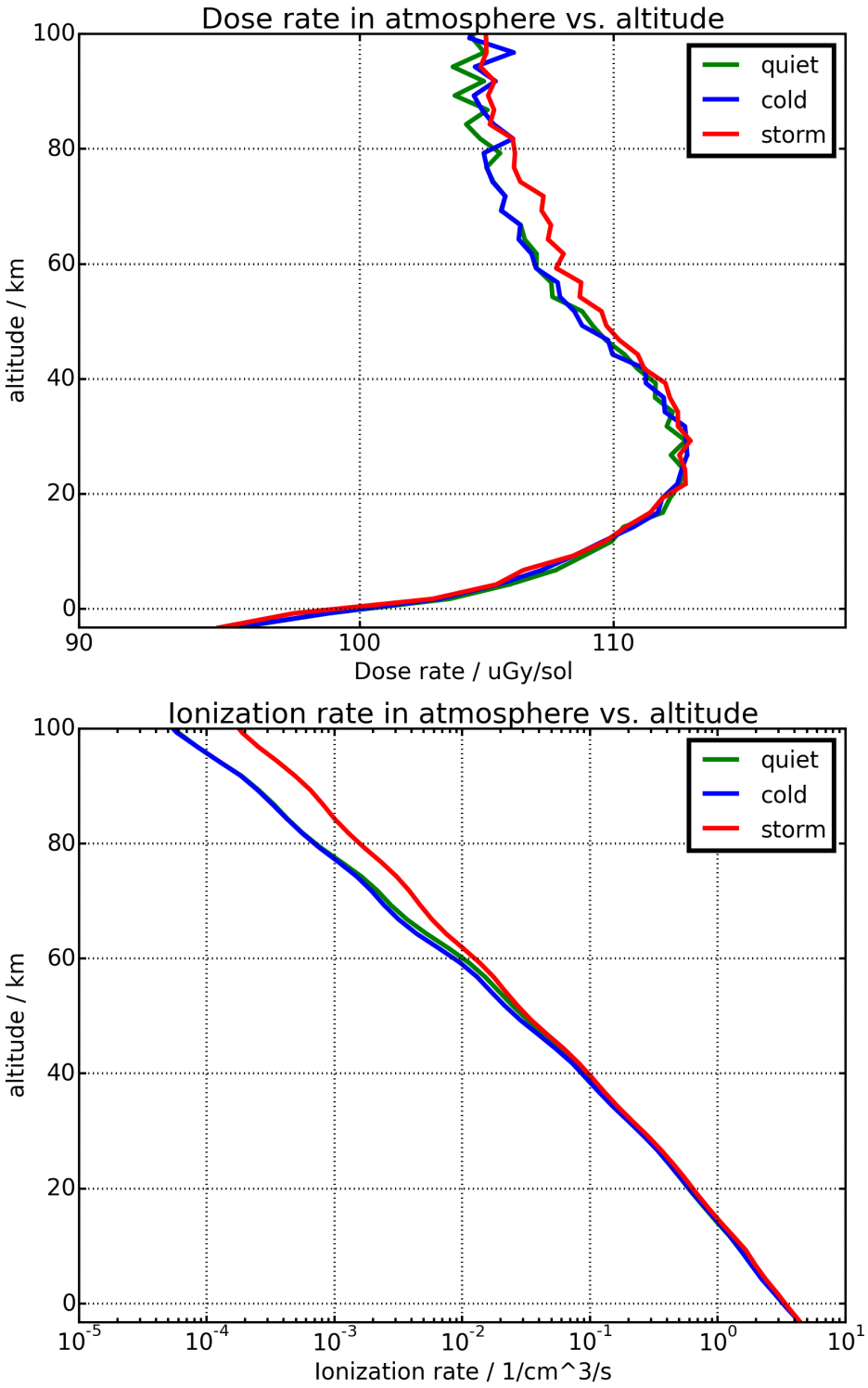

Fig. 4. Energy deposition profiles in the atmosphere. The top figure shows a dose rate profile for all three atmospheric scenarios using only GCR primaries. The bottom figure shows the ionization rate profiles in the atmosphere computed from the results shown in the top figure.

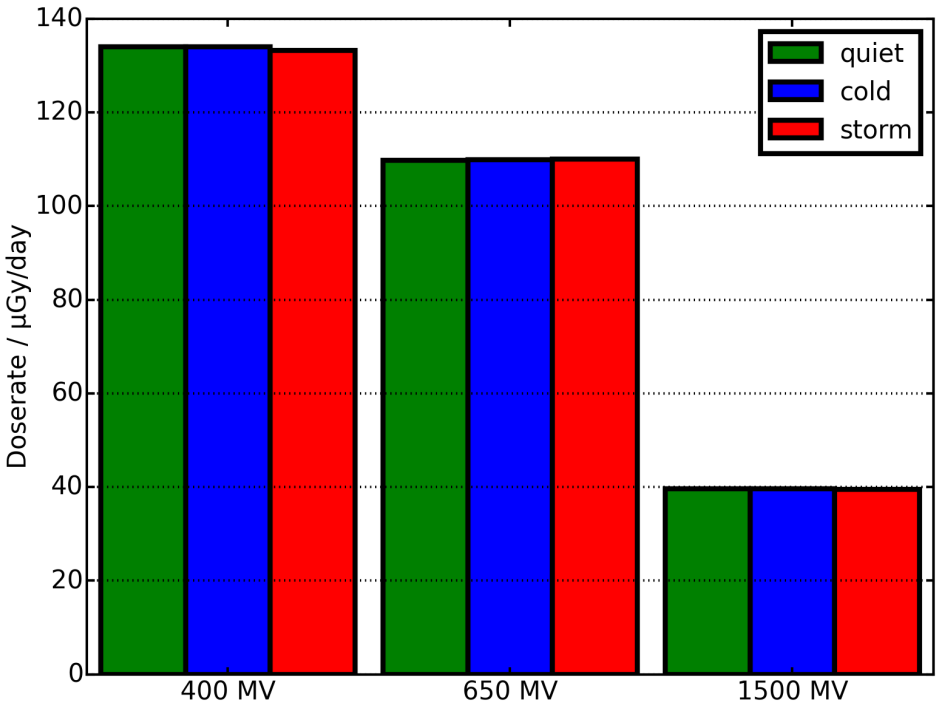

Fig. 5. The influence of extreme solar modulation scenarios on dose rates on the Martian surface. The doses shown are computed from models using hydrogen and helium primary particle spectra.

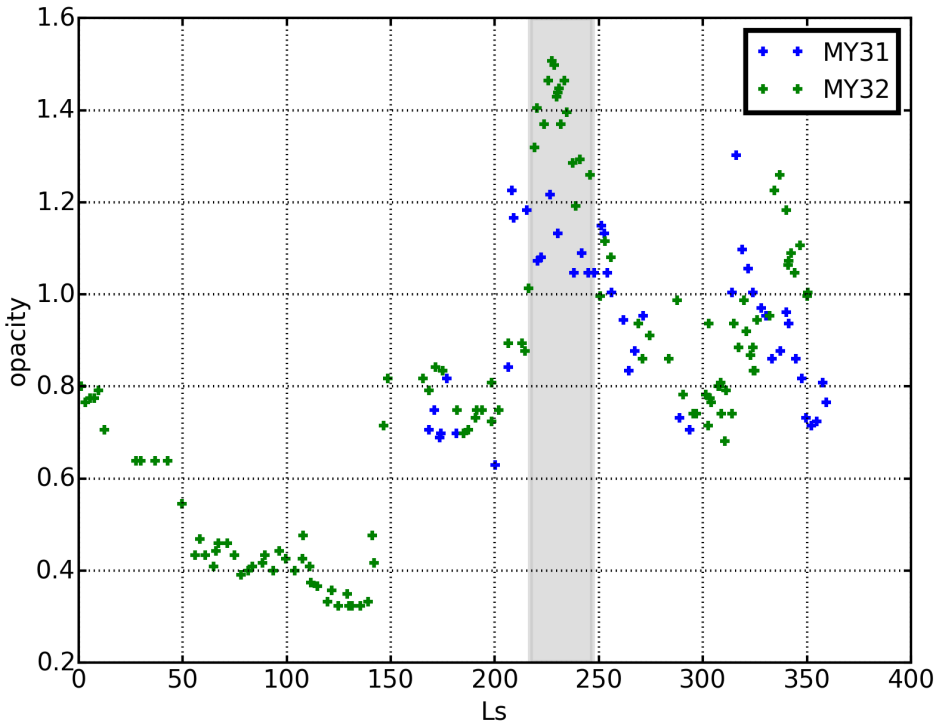

Fig. 6. Measurements of atmospheric opacity τ for the first 1000 sols of the MSL mission. The measurements are taken from Martínez et al. (2017). We show the mean opacity per sol for each sol with available data. The shaded area shows the time of enhanced atmospheric opacity in MY 32.

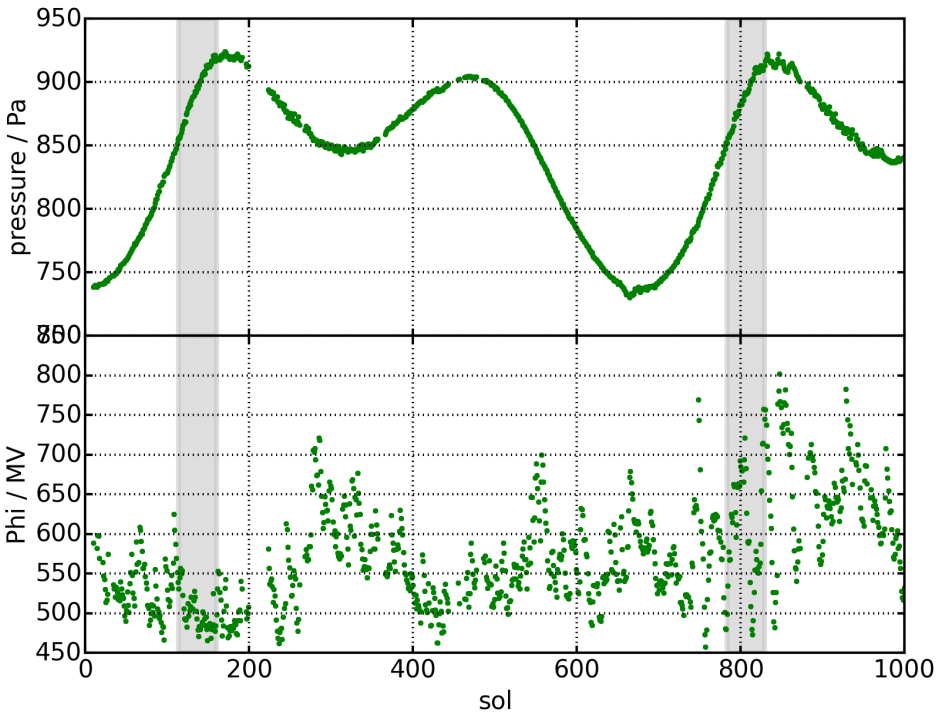

Fig. 7. Ground-level atmospheric pressure and solar modulation potential data sets used to correct the dose rate measurements. The gray shading around sol 800 indicates time of enhanced atmospheric opacity, the earlier shading before sol 200 marks the same season in the preceding Martian year. From Guo et al. (2015).

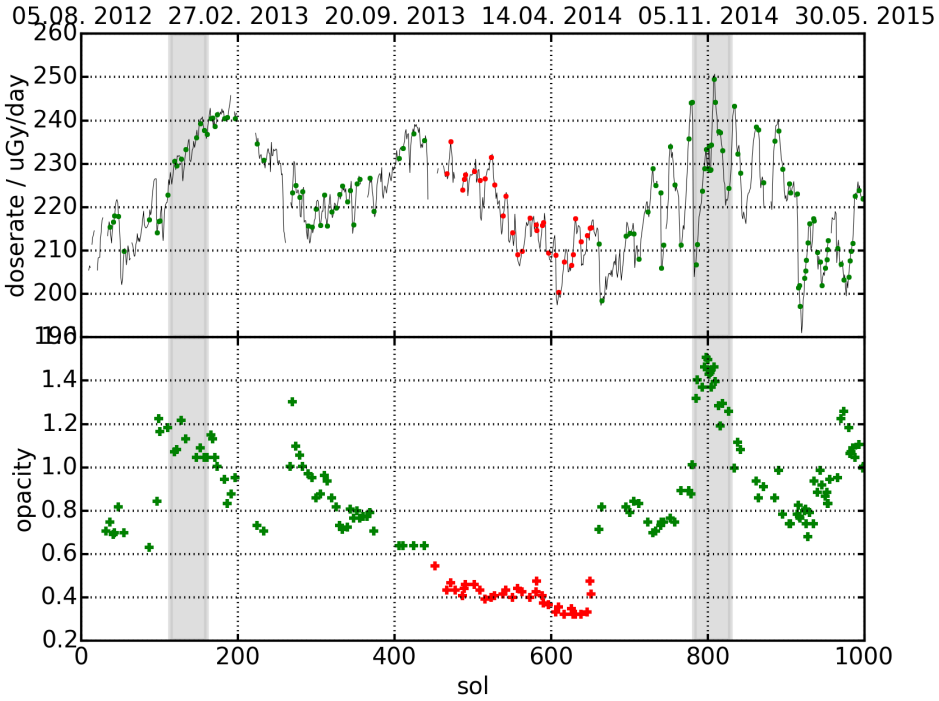

Fig. 8. Timeline of surface dose rate in tissue equivalent (top) produced from RAD measurements, and atmospheric opacity produced from measurements by Mastcam as published in Martínez et al. (2017) (bottom). The tissue equivalent surface dose rates have been produced from measurements in detector E of the RAD instrument. The measurements have been processed to remove the influence of atmospheric pressure as described in Equations 3. The plots show the mean per sol for each data set. The time colored in red indicates an opacity of $\tau < 0.6$ during summer in the northern Martian hemisphere. The gray shading around sol 800 indicates time of enhanced atmospheric opacity, the earlier shading before sol 200 marks the same season in the preceding Martian year.

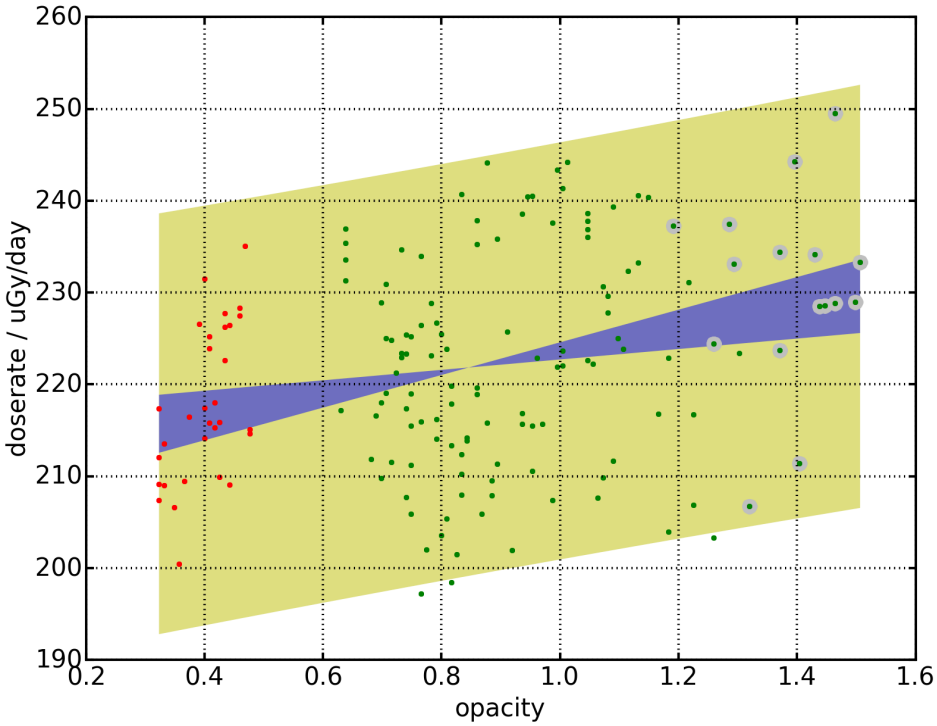

Fig. 9. Surface dose rate in tissue equivalent from RAD measurements, plotted vs. atmospheric opacity from measurements by Mastcam (Martínez et al., 2017). The tissue equivalent surface dose rates have been determined from measurements in detector E of the RAD instrument. The dose rate measurements have been processed to remove the influence of atmospheric pressure as described in Equation 3. The plot shows the mean per sol for each data set. The points colored in red indicates an opacity of $\tau < 0.6$ during summer in the northern Martian hemisphere. The points marked with gray shading indicate the time of enhanced atmospheric opacity. The yellow-shaded band shows the 95% prediction band, the blue-shaded band shows the 95% confidence band.

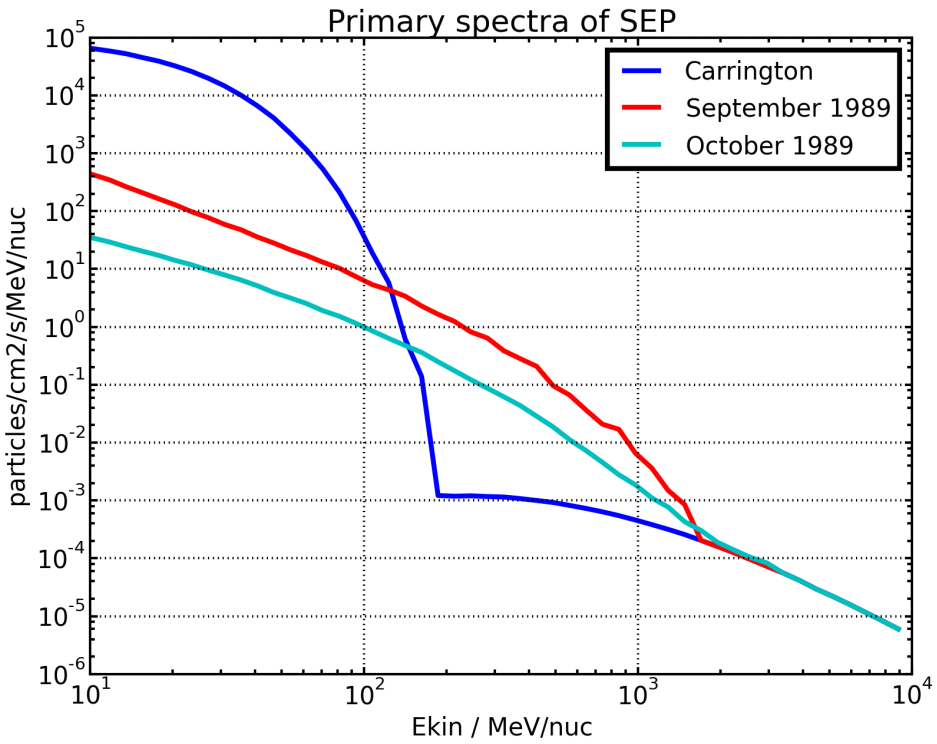

Fig. A.1. Primary spectra used in the model calculations for SEP particles. Shown are the primary SEP proton spectra added to the primary GCR spectrum for hydrogen.

Appendix A: Solar Energetic Particle Events

In addition to modeling the changes in the Martian radiation environment due to GCR particles under different atmospheric conditions, we performed the same model calculations for a set of representative Solar Energetic Particle (SEP) events. Since the results of the SEP modeling are not needed for the comparison between RAD observations and model predictions we performed here, we include them as an appendix.

A.1. Model Setup

For this study, we considered model spectra of three Solar Energetic Particle (SEP) events also studied in Norman et al. (2014). These events were the Carrington event, the September 1989 event, and the October 22, 1989 event. For all events, we consider only proton fluxes, as these are the most important particles for atmospheric and ground-level spectra.

The events are selected to represent various extremes of the wide range of SEP characteristics. The Carrington event represents an extraordinarily intense event, with the highest integral proton flux. The September 1989 event represents a harder particle spectrum, containing more particles at higher energies, than the Carrington event, though with lower integral flux. The October 1989 event has the same spectral hardness as the September 1989 event, but has a lower integral flux.

We show the primary spectra of the events in Fig. A.1.

Table A.1. Parameters used to characterize the Carrington and October 1989 events according to Equation A.1 (Norman et al., 2014), (Townsend et al., 2006)

	Carrington event	October 1989 event
$\phi_0/\frac{1}{\mathrm{cm^2\,s\,sr}}$	$2.78{\cdot}10^5$	429.0
κ/MeV	0.0236	0.458
α	1.108	0.3908

Table A.2. Parameters used to characterize the September 1989 event according to Equation A.2 (Norman et al., 2014), (Sheel et al., 2012)

	September 1989 event
$\kappa/\frac{1}{\mathrm{cm^2\,s\,sr\,MeV}}$	6000.0
γ	1.7
E_{ref}/MeV	1.0
E_0/MeV	600.0

The parametrizations of all events were taken from Norman et al. (2014). The differential flux of the Carrington and the October 1989 events are described by

$$\frac{d\phi}{dE} = \phi_0 k\alpha E^{\alpha-1} e^{-kE^{\alpha}} \tag{A.1}$$

(Townsend et al., 2006). The parameter Φ is the proton fluence, E the proton energy, and k and α are dimensionless parameters. The values used for the events are summarized in Tab. A.1.

The September 1989 event has a differential flux that is described by

$$\frac{d\phi}{dE} = \kappa\left(\frac{E}{E_{ref}}\right)^{-\gamma} e^{-E/E_0} \tag{A.2}$$

(Sheel et al., 2012) with proton fluences Φ and κ, the proton energy E, and a dimensionless parameter *gamma*. The values are given in Tab. A.2.

It should be noted that while the SEP event particle spectra we have used have been modeled after historic SEP occurrences, we do not aim to study these events in particular. Rather, they were selected to represent a range of possible future SEP events, and to allow comparison with the results by Norman et al. (2014). This is especially obvious for the Carrington event spectrum, for which no observational data of the particle energy spectrum exists and which should be seen as a hypothetical spectrum for the historic event. The spectra also represent the peak flux during each SEP event. The dose rates we compute from them should not be used to calculate total doses during an event.

A.2. Model Results

All ground-level downward particle spectra for the three SEP events in all atmosphere scenarios are shown in Fig. A.2. Again, there are no spectral changes between any of the atmosphere conditions. It should however be noted that all three events shown are ground-level events. That is, the enhanced proton flux at the top of the atmosphere, compared to GCR levels, propagates through the atmospheric column to the ground, resulting in an enhanced ground-level proton flux as well.

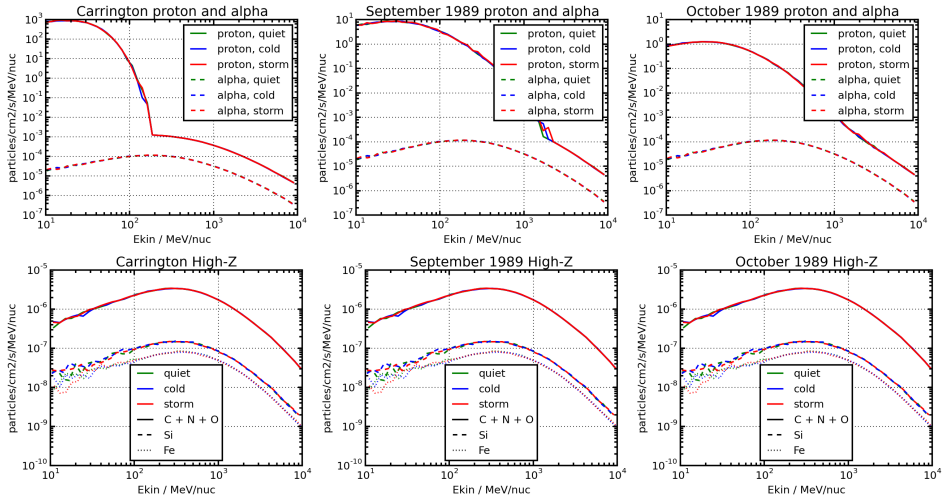

Fig. A.2. Ground-level spectra resulting from the three SEP events added to the GCR hydrogen primary spectra. The top row shows hydrogen and helium spectra, the bottom row shows high-Z particle spectra. The different events are shown in a separate column each, with the left one showing the Carrington event, the middle one the September 1989 event and the right one the October 1989 event.

Fig. A.3 shows the energy deposition in the atmosphere for all three SEP events. First, when compared to the GCR energy deposition shown in Fig. 4, it is obvious that all SEP events result in dose rates that are higher by multiple orders of magnitude, dropping quickly with lower altitude. The Carrington event shows no variation for the dose rates between the three atmospheric scenarios. Interestingly, the September 1989 and October 1989 events show a slightly smaller dose rate for the global dust storm scenario for altitudes above 60 km.

The ionization rates, shown in the lower panel in Fig. A.3, again show a notably enhanced rate for the global dust storm scenario. As is the case with GCR, the enhancement in ionization rate is mainly driven by the increased atmospheric density.

A.3. Dose and Ionization Rates at ground level and altitudes of 100 km

Tab. A.3 lists dose and ionization rates caused by the three SEP events for all three atmosphere conditions at altitudes of 100 km and 0 km. We show a comparison between the global dust storm and the quiet scenario in Tab. A.4. Here, we computed the ratio of dose and ionization rates between the global dust storm and the quiet atmospheric scenario. SEP induced dose rates are slightly reduced during a global dust storm by 3 % to 24 %.

Ground-level ionization rates are slightly decreased for SEP events. However, at an altitude of 100 km during a global dust storm, we observe ionization rates that are increased by a factor of 100.

Appendix B: Discussion of SEP Simulations

Dose and ionization rates for SEP events show different behaviors when compared to the GCR results, depending on the spectral shape and flux of the individual event. All three SEP events show

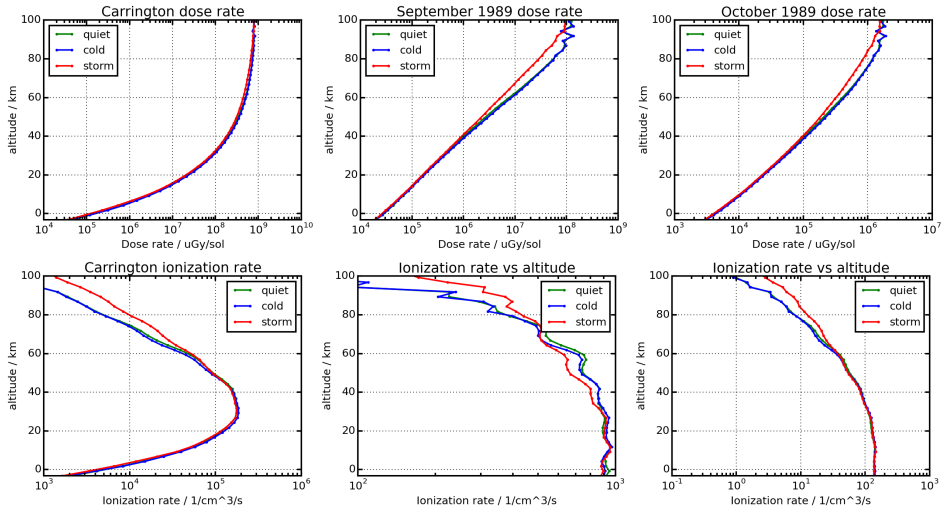

Fig. A.3. Profiles of energy deposit in the atmosphere during SEP events. The top row shows the dose rate for each of the three events during each atmospheric condition. The bottom row shows the ionization rate computed from the dose rate. The left column shows the Carrington event, the middle column shows the September 1989 event, and the right column shows the October 1989 event.

a rapid drop to the minimum dose rate at ground level. Ionization rates show even more varied behavior. The Carrington event is especially notable, since it produces a pronounced maximum at an altitude of approximately 40 km. The other two events show a steady increase with decreasing altitudes and reach a plateau at approximately 50 km for the September 1989 event and approximately 30 km for the October 1989 event. As is the case with GCR, all SEP spectra show an enhancement in ionization rate for altitudes above 60 km.

We observed a particular sensitivity of the computed dose rate results on the lower energy limit chosen for the computations, as shown, e.g., in Fig. B.1. The SEP dose rates were particularly sensitive to this calculation. The reason for this is obvious from the primary event spectra shown in Fig. A.1. All SEP event show high proton fluxes at low energies, where the energy loss per unit length $\frac{\mathrm{d}E}{\mathrm{d}x}$ of the particles are high. Consequently, those particles deposit a high dose rate, and cuts in this energy range influence the computed dose rate greatly. This is shown in Fig. B.1 for dose rates computed using different lower energy limits from primary interplanetary spectra. The influence of the selection of the lower energy limit is clearly visible, changing the resulting dose rate over more than an order of magnitude. This makes it clear that when computing dose rates, especially for SEP events, care must be taken to select the lower energy limit of the computation if the results are to be compared to the work of others.

The influence of the lower energy limit on dose rate computations can also be used to perform a first-order study on the influence of thin shielding elements on the dose rate. As a typical construction material for spacecraft, let us consider Aluminum as a shielding material. We find that, at a mass density of $\rho = 2.73 \frac{\mathrm{g}}{\mathrm{cm}^2}$, even thin layers of Aluminum are able to stop the low-energy particles, which, as discussed above, influences the resulting dose rate significantly. This emphasizes the importance of exact knowledge of shielding geometry for an analysis of expected dose rate for, e.g., a manned space mission.

Table A.3. SEP induced dose and ionization rates for all three atmosphere scenarios at an altitude of 0 km, meaning ground level at Gale crater, and 100 km. The rates have been computed for particle energies between 1 MeV and 10 GeV.

100 km, dose rates / μGy/day

	Carrington	Sep89	Oct89
quiet	$8.20{\cdot}10^{8}$	$1.46{\cdot}10^{8}$	$1.91{\cdot}10^{6}$
cold	$8.12{\cdot}10^{8}$	$1.41{\cdot}10^{8}$	$1.85{\cdot}10^{6}$
storm	$7.97{\cdot}10^{8}$	$1.11{\cdot}10^{8}$	$1.68{\cdot}10^{6}$

100 km, ionization rates / 1/cm^3

	Carrington	Sep89	Oct89
quiet	$4.35{\cdot}10^{+2}$	$7.58{\cdot}10^{+1}$	$9.98{\cdot}10^{-1}$
cold	$4.16{\cdot}10^{+2}$	$6.95{\cdot}10^{+1}$	$9.29{\cdot}10^{-1}$
storm	$1.34{\cdot}10^{+3}$	$1.83{\cdot}10^{+2}$	$2.81{\cdot}10^{+0}$

0 km, dose rates / μGy/day

	Carrington	Sep89	Oct89
quiet	$1.73{\cdot}10^{5}$	$2.90{\cdot}10^{4}$	$4.35{\cdot}10^{3}$
cold	$1.74{\cdot}10^{5}$	$2.83{\cdot}10^{4}$	$4.42{\cdot}10^{3}$
storm	$1.32{\cdot}10^{5}$	$2.64{\cdot}10^{4}$	$4.06{\cdot}10^{3}$

0 km, ionization rates / 1/cm^3

	Carrington	Sep89	Oct89
quiet	$5.37{\cdot}10^{+3}$	$9.40{\cdot}10^{+2}$	$1.41{\cdot}10^{+2}$
cold	$5.34{\cdot}10^{+3}$	$9.10{\cdot}10^{+2}$	$1.42{\cdot}10^{+2}$
storm	$4.28{\cdot}10^{+3}$	$8.92{\cdot}10^{+2}$	$1.37{\cdot}10^{+2}$

Table A.4. Ratios between storm and quiet atmosphere scenarios for SEP induced dose and ionization rates at an altitude of 0 km, corresponding to ground level at Gale crater, and 100 km. The ratios have been computed for particle energies between 1 MeV and 10 GeV.

Dose rate ratios storm/quiet

	Carrington	Sep89	Oct89
0 km	$7.61{\cdot}10^{-1}$	$9.07{\cdot}10^{-1}$	$9.34{\cdot}10^{-1}$
100 km	$9.72{\cdot}10^{-1}$	$7.57{\cdot}10^{-1}$	$8.81{\cdot}10^{-1}$

Ionization rate ratios storm/quiet

	Carrington	Sep89	Oct89
0 km	$7.98{\cdot}10^{-1}$	$9.49{\cdot}10^{-1}$	$9.77{\cdot}10^{-1}$
100 km	$3.09{\cdot}10^{+0}$	$2.42{\cdot}10^{+0}$	$2.81{\cdot}10^{+0}$

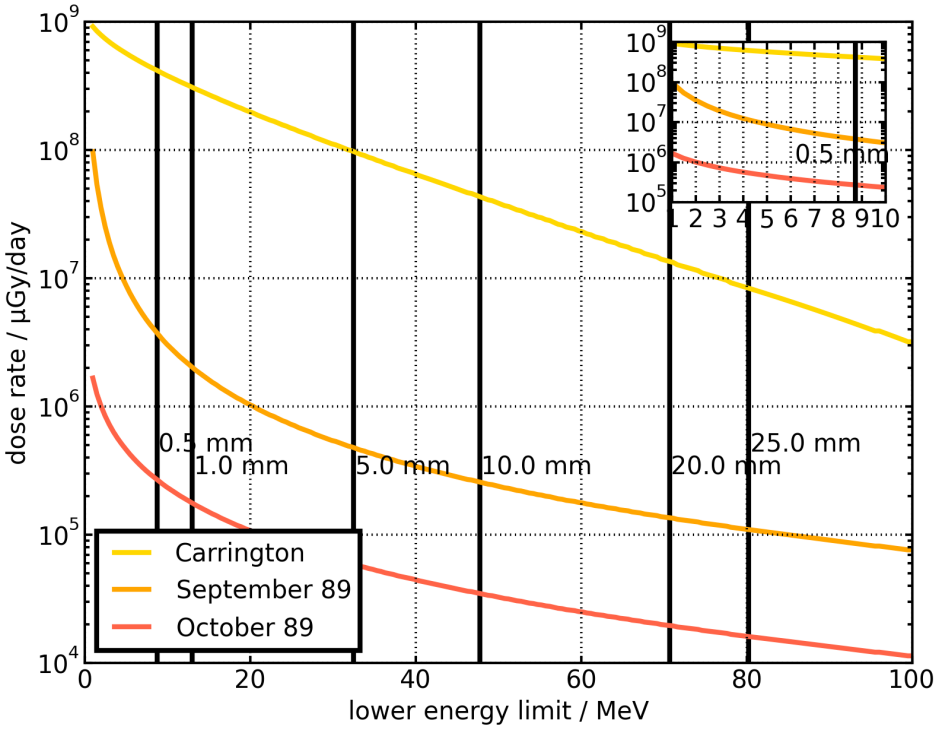

Fig. B.1. Dose rate results for varying lower energy limits. The upper energy limit for the dose rate computations is kept constant at $E_{upper} = 10\,\mathrm{GeV}$. The dose is computed for the model SEP proton spectra in interplanetary space as described by Equations A.1 and A.2 and the parameters in Tab. A.1 and A.2. The inset shows a magnification of the first 10 MeV. The annotated vertical black lines show shielding by aluminum. The lines denote the highest proton energy stopped in a layer of aluminum of the thickness annotated, in millimeter.

6

DIRECTIONALITY OF PARTICLE FLUXES

The Martian radiation environment consists not only of downward-directed, but also upward-directed particle fluxes. The upward-directed fluxes consist of both scattered primary particles as well as secondary particles generated within the Martian atmosphere and soil. From particle transport simulations, they have been predicted to be a significant percentage of the total particle flux.

Measuring the upward-directed particle fluxes is, of course, important for a complete assessment of the Martian radiation environment. Additionally, there are other reasons why they should be investigated. The first reason is their importance for dosimetry. As will be shown below in Section 6.2, neutrons show a strong upward flux. At the same time, they are important for dosimetry because they have a high interaction cross section for biological tissue. The second reason is the opportunity to use the upward particle fluxes to validate particle transport simulations and thus helping to meet one of the science goals of the Radiation Assessment Detector (RAD) instrument.

The measurement of upward-directed particle fluxes in the RAD instrument is made challenging by the instrument's design. It is intended to measure downward-directed particle fluxes in the Solid State Detector (SSD) particle telescope, as well as neutral particles omnidirectionally. When entering the instrument from below, low-energy particles can easily be stopped by the scintillation detectors on the bottom of the RAD instrument, which have a high mass density. In addition, the instrument triggers are set up to discard charged particle events that do not deposit any energy in the B detector. In practice, this means that the RAD instrument cannot detect the direction of neutral particles, and can only discriminate between upward and downward charged particle fluxes if the particles have enough energy to penetrate all of the detectors in the detector stack.

This chapter first presents a method to determine the directionality of charged particles using the RAD instrument, followed by a study of an instrument concept designed to determine the directionality of neutrons.

6.1 OBSERVING DIRECTIONALITY OF CHARGED PARTICLES

The work on charged particle directionality detection has been published as a paper in the "Journal for Geophysical Research". The manuscript is reproduced below. The authors' own contribution to the manuscript is 85 %.

AGU PUBLICATIONS

Earth and Space Science

RESEARCH ARTICLE
10.1002/2016ea000240

Key Points:
- We model the radiation environment during the MSL cruise phase and on the Martian surface
- We obtain the particle energy spectra at the RAD instrument for both scenarios
- After developing a method to distinguish between upward and downward fluxes, we apply the method both to simulation data and to data taken by the RAD instrument during the cruise phase and on the surface

Correspondence to:
J. K. Appel,
appel@physik.uni-kiel.de

Citation:
Appel, J. K., Köehler, J., Guo, J., Ehresmann, B., Zeitlin, C., Matthiä, D., … Weigle, G. (2018). Detecting upward directed charged particle fluxes in the Mars Science Laboratory Radiation Assessment Detector. *Earth and Space Science*, *5*, 2–18. https://doi.org/10.1002/2016ea000240

Received 23 NOV 2016
Accepted 20 OCT 2017
Accepted article online 15 NOV 2017
Published online 23 JAN 2018

Detecting Upward Directed Charged Particle Fluxes in the Mars Science Laboratory Radiation Assessment Detector

J. K. Appel[1], J. Köehler[1,2], J. Guo[1], B. Ehresmann[3], C. Zeitlin[4], D. Matthiä[5], H. Lohf[1], R. F. Wimmer-Schweingruber[1], D. Hassler[3], D. E. Brinza[6], E. Böhm[1], S. Böttcher[1], C. Martin[1], S. Burmeister[1], G. Reitz[5], S. Rafkin[3], A. Posner[7], J. Peterson[3], and G. Weigle[8]

[1]Institute for Experimental and Applied Physics, University of Kiel, Germany, [2]Thales Electronic Systems GmbH, Kiel, Germany, [3]Southwest Research Institute, Boulder, CO, USA, [4]Lockheed Martin Information Systems & Global Solutions, Houston, TX, USA, [5]Aerospace Medicine, Deutsches Zentrum für Luft- und Raumfahrt, Köln, Germany, [6]Jet Propulsion Laboratory, California Institute of Technology, Pasadena, CA, USA, [7]Science Mission Directorate, NASA Headquarters, Washington, DC, USA, [8]Big Head Endian, LLC, Burden, KS, USA

Abstract The Mars Science Laboratory rover Curiosity, operating on the surface of Mars, is exposed to radiation fluxes from above and below. Galactic Cosmic Rays travel through the Martian atmosphere, producing a modified spectrum consisting of both primary and secondary particles at ground level. These particles produce an upward directed secondary particle spectrum as they interact with the Martian soil. Here we develop a method to distinguish the upward and downward directed particle fluxes in the Radiation Assessment Detector (RAD) instrument, verify it using data taken during the cruise to Mars, and apply it to data taken on the Martian surface. We use a combination of Geant4 and Planetocosmics modeling to find discrimination criteria for the flux directions. After developing models of the cruise phase and surface shielding conditions, we compare model-predicted values for the ratio of upward to downward flux with those found in RAD observation data. Given the quality of available information on Mars Science Laboratory spacecraft and rover composition, we find generally reasonable agreement between our models and RAD observation data. This demonstrates the feasibility of the method developed and tested here. We additionally note that the method can also be used to extend the measurement range and capabilities of the RAD instrument to higher energies.

Plain Language Summary The MSL rover Curiosity is exposed to energetic particles from above and below on the Martian surface. Particles enter the Martian atmosphere from above and travel through it until they reach the ground. Particles lose energy and can produce secondary particles while passing through the atmosphere, resulting in an energy distribution on ground level that is different from that on the top of the atmosphere. The resulting particles produce an upward directed particle distribution in the soil. We develop a method to distinguish the upward and downward particle fluxes in the RAD instrument, verify it using data taken during the cruise to Mars, and apply it to data taken on the Martian surface. We use a combination of models to find criteria for discriminating the flux directions. After developing models of the cruise phase and surface shielding conditions, we compare simulated values for the ratio of upward to downward flux with those found in observation data. We find generally reasonable agreement between our models and RAD observation data. This demonstrates the feasibility of the method developed and tested here. The method can also be used to extend the measurement range and capabilities of the RAD instrument to higher energies.

1. Introduction

The Mars Science Laboratory (MSL) mission is an ongoing NASA mission. It successfully landed the rover "Curiosity" inside the Gale Crater on the surface of Mars on 6 August 2012 (Grotzinger et al., 2012). One of the scientific instruments on board the rover is the Radiation Assessment Detector (RAD), which measures the Martian radiation environment. It is able to measure charged particles $\geq 100\ \frac{\text{MeV}}{\text{nuc}}$ (Hassler et al., 2012). RAD is designed to measure radiation entering the detector from above. The main science goals of the RAD instrument

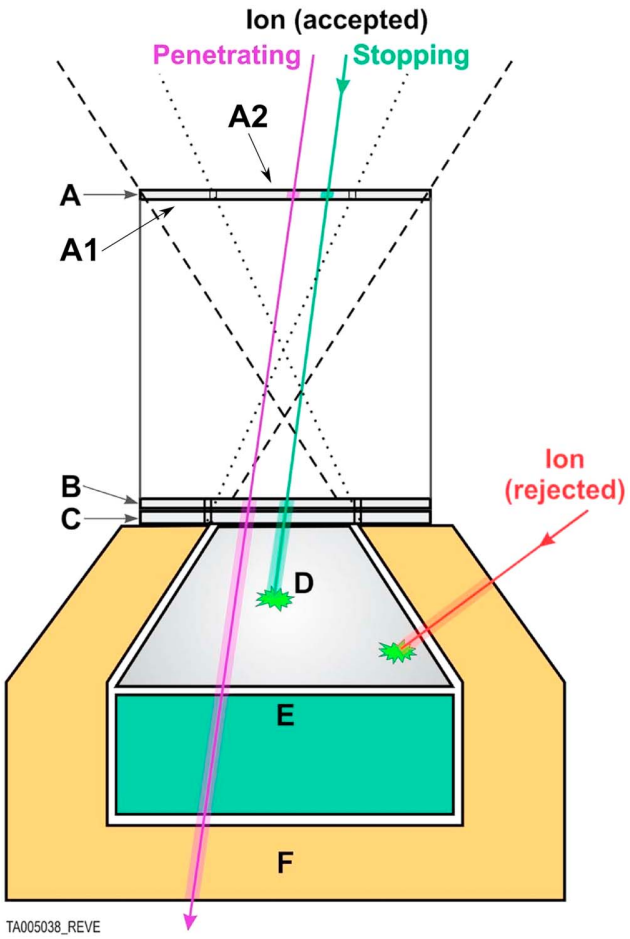

Figure 1. Schematic view of the RAD detector with various particle detections shown. The viewcone as defined by the A1-B coincidence (dashed) and by the A2-B coincidence (dotted) is shown, as are the names of the detectors. For the SSD, the segmentation borders are visible. (Ehresmann et al., 2014 there modified from Hassler et al., 2012).

include characterizing the Martian radiation environment to enable validating models of atmospheric particle transport.

In this paper, we will present a method to discriminate between upward and downward directed charged particle fluxes above the particle energy range RAD is designed to measure. The application of this method significantly increases the instruments' capabilities for charged particle detection. In addition, it aids in validating the particle transport models used in this analysis.

RAD operated during most of the cruise phase from Earth to Mars, taking almost 220 days of data (Zeitlin et al., 2013). It has been operating on the surface of Mars almost continuously since the landing of the MSL rover on 6 August 2012 (Hassler et al., 2014). This provides us with a still growing data set spanning over 1,300 Martian days (sols) to date, including the full Martian annual cycle, which is about 668 sols, with 1 sol being about 1.03 Earth days long (Allison, 1997).

This paper is organized in the following way: After a short description of relevant features of the RAD instrument, we develop a method for discriminating upward and downward fluxes through simulations. The simulation results help us to test and pin down certain criteria of the method when applied to data. With these criteria, we apply the method to data of the radiation environment RAD measures both during the cruise phase and on the surface of Mars. We compare the findings from the modeling with data obtained both during cruise phase and on the Martian surface. Lastly, we assess the findings and discuss the accuracy of the models and transport codes used in this analysis.

1.1. The RAD Instrument

The Radiation Assessment Detector (RAD) is a compact and light-weight instrument designed to fully characterize the radiation environment on the Martian surface.

RAD derives heritage from the Comprehensive SupraThermal and Energetic Particle analyzer (COSTEP) instrument on SOHO (Müller-Mellin et al., 1995), the Matroshka instrument currently flying on the ISS (Reitz et al., 2009), as well as Böhm (2004) and Posner et al. (2005). A detailed description of RAD is given in Hassler et al. (2012). We describe briefly the features relevant to this investigation in the following paragraphs.

A schematic view of the RAD instrument is shown in Figure 1. It employs a detector stack consisting of three hexagonal silicon Solid State Detectors (SSD) called detectors A, B, and C on top of two scintillation detectors, called D and E. Detector A is split into two segments, an outer segment called A1 and an inner segment called A2. The detectors B and C only use the inner segment of the detector. The scintillation detectors are enclosed in an anticoincidence shield made of another scintillation detector, F.

The D detector is a truncated hexagonal pyramid of thallium- doped Cesium Iodide (CsI(Tl)). The E scintillator is made of Bicron BC-432 m plastic scintillator and has an extruded hexagonal shape. BC-432 m is also used for the anticoincidence, F, which is split into two scintillators, F2 below the detector stack and F1 enclosing D and E from the side.

The two segments of the A detector, together with the inner segment of the B detector, define the two possible view cones of the RAD instrument. The A1-B coincidence viewcone uses the outer A1 segment, and the A2-B coincidence viewcone uses the inner A2-B viewcone, which is also fully covered by the D detector below it. As we will later show, our analysis requires particles to deposit energy in both the D and the E detector. Since only the A2-B viewcone is fully covered by the D detector, we only consider particles inside the A2-B viewcone in this work.

RAD is designed to measure protons and alpha particles entering the detector stack from above in an energy range between 10 MeV and 100 $\frac{\text{MeV}}{\text{nuc}}$.

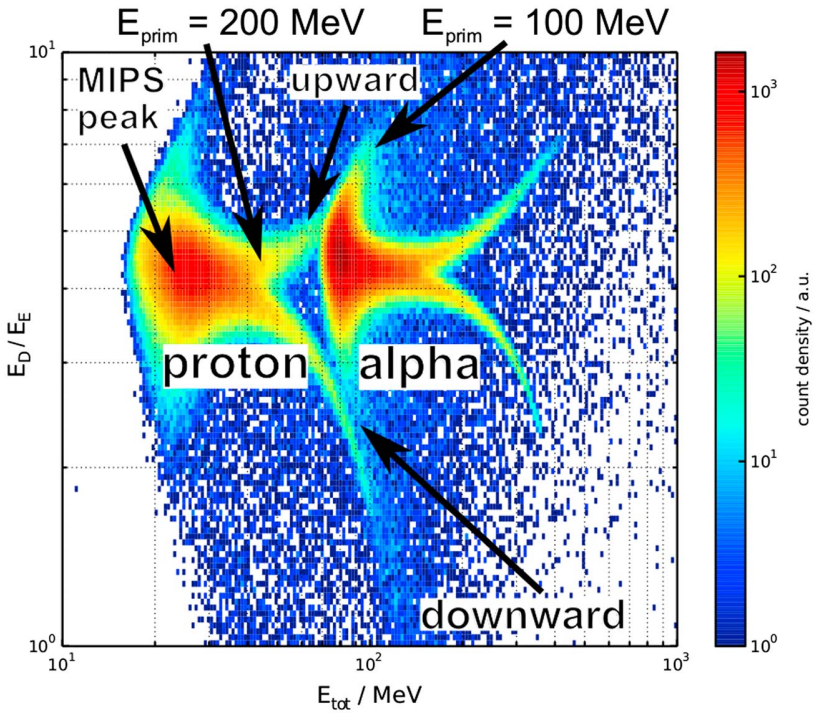

Figure 2. Two-dimensional count density histogram for simulation data of $\frac{E_D}{E_E}$ versus E_{tot}. The annotations denote particle species and beam directions.

2. Simulation Setup

We performed two major simulation steps in order to analyze the instrument response to upward directed particle fluxes. First, we develop criteria to distinguish between the upward and downward fluxes in RAD data. In order to do this, we simulated the passage of particles with a uniform energy spectrum through only the RAD instrument. After we found working discrimination criteria, we replicated the RAD measurement both inside the spacecraft during the cruise phase and on the Martian surface. This was achieved by first simulating the passage of particles through the surrounding geometry, which during the cruise phase consists of the MSL cruise stage and the rover itself, and on the surface consists of the Martian atmosphere and soil as well as the rover body. These models yielded the upward and downward directed spectra at the position of the RAD instrument. We then simulated the response of the instrument to these spectra and applied the discrimination method as developed in the first step of this analysis.

2.1. Upward and Downward Fluxes in the RAD Instrument

We simulated the passage of upward and downward directed particle fluxes through the instrument in two separate simulations using the GEANT4 toolkit (Agostinelli et al., 2003). We used version 10 of the toolkit, using the QGSP_BERT physics list, for all instrument and shielding simulations. The particle source for these simulations was a circular area positioned just above the A detector for downward and just below the F detector for upward directed radiation. The particles were emitted in beams parallel to the central axis of the RAD instrument with no angular distribution of the tracks. For the energy spectrum of the particles, a logarithmically flat spectrum from 100 MeV to 1 GeV was generated.

Based on the results of this simulation, we are able to discriminate the flux direction in the energy range between a primary particle energy of $E_{\mathrm{prim}} = 100$ MeV and $E_{\mathrm{prim}} = 200$ MeV by plotting the ratio between energy deposited in detectors D and E, namely, $\frac{E_D}{E_E}$, versus the total deposited energy $E_{\mathrm{tot}} = E_{A2} + E_B + E_C + E_D + E_E$. Because we use energy deposited in detectors D and E for determining the flux direction, we need complete coverage of the telescope viewcone by those detectors. This is true for the narrower A2-B viewcone, so we only select particles within this viewcone.

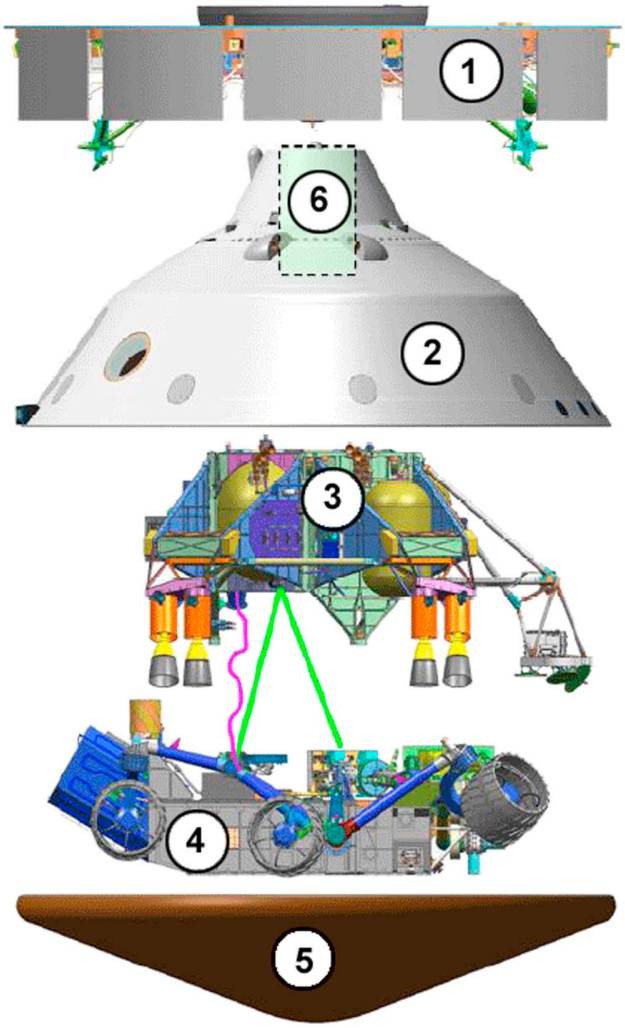

Figure 3. Schematic view of the components of the MSL cruise stage. The labeled parts are 1—cruise stage, 2—aeroshell, 3—descent stage, 4—MSL rover, 5—heatshield, and 6—parachute assembly (Image credit: NASA/JPL-Caltech).

The F detector is used as an anticoincidence shield for the telescope: particles that enter the instrument from below and deposit energy in the F detector get rejected by the detection logic. The exception to this is penetrating particles which deposit energy in all detectors of the stack. It is thus necessary to require penetrating particles in order to detect upward directed fluxes in the instrument.

We then plot $\frac{E_D}{E_E}$ versus E_{tot} in a 2-D count density histogram as shown in Figure 2. The distinctive proton and alpha particle populations are clearly visible. For each particle type, we find the peak intensity produced by the Minimum Ionizing ParticleS (MIPS) on the side of the population with the least deposited energy E_{tot} as expected from the Bethe-Bloch formula. As particles with smaller primary energies deposit more energy, we can discern the upward and downward branch.

For protons, the branches separate at a deposited energy of $E_{tot} \geq 42$ MeV up to an energy of $E_{tot} = 100$ MeV, where the particles do not penetrate the detector stack any longer. This corresponds to a primary proton energy range of 100 MeV $\leq E_{prim} \leq$ 200 MeV for which we are able to separate the particle direction.

This discrimination can, in principle, be applied to all charged particles detected with the RAD instrument. However, we will only present the analysis for protons, because protons are the most common particles in these environments, particularly among the secondary particles coming from the surface (e.g., Ehresmann, 2014; Matthiä et al., 2016).

2.2. The RAD Shielding Environment During the MSL Cruise Phase

During the cruise phase, the instrument was not only shielded from upward directed particles by the rover, but the rover itself was shielded inside the MSL spacecraft, consisting of four main parts: The descent stage mounted above the rover, the aeroshell and heatshield surrounding both rover and descent stage, and the cruise stage mounted above the aeroshell. A schematic of this configuration is shown in Figure 3. This leads to a highly inhomogenous shielding in the upper viewcone of the RAD instrument, where particles are shielded by the descent stage, the aeroshell, and the cruise stage. While approximately half of the field of view is almost unshielded, the other half is shielded by various amounts of mass. The lower viewcone is shielded by the rover body itself and the heatshield.

For the simulation of upward and downward particle fluxes during the cruise phase, we employed a separate simulation for each direction. Both simulations use a square source area with a side length of $l = 10$cm from which the primary particle spectra were generated as parallel beams. The particle beams then passed through the shielding masses before being registered in a vacuum volume used for particle counting.

Upward directed particles are shielded both by the rover body and by the aeroshell, which in this part is the heat shield for the atmosphere entry. The rover body is represented by two blocks of different materials: the rover bellypan consisting of a 5 mm aluminum plate, followed by the rover body filled with electronics with a height of 29 cm. The best data available to the authors states that the rover body is dominated by the RAD Electronics Box (REB) with a shielding density of 6 g cm^{-2}, consisting of Printed Circuit Boards (PCB) plus magnesium to account for the REB housing. The chemical composition of PCBs is taken from Ogunniyi et al. (2009). The heatshield is positioned directly below the rover bellypan. It is represented by a 3.2 cm high block of carbon with a density of 0.27 $\frac{g}{cm^3}$ (Tran et al., 1996; Edquist et al., 2014). The composition, densities, and dimensions of the different blocks are given in Table 1.

The shielding density distribution for the upper viewcone is described in Zeitlin et al. (2013) as shown in Figure 4. From this we approximate the shielding as 10 blocks of aluminum with varying thickness according to the integrated shielding density inside the instrument viewcone. A histogram of this distribution inside

Table 1
Composition and Density of Simulation Boxes

Block	Density	Composition
Heatshield	0.27 $\frac{mg}{cm^3}$	C: 100%
Belly plate	2.7 $\frac{g}{cm^3}$	Al: 100%
		Cu: 20%
		SiO_2: 15%
		PET: 9.9%
		PP: 4.8%
Rover body	0.183 $\frac{g}{cm^3}$	Al: 2%
		Pb: 2%
		Ni: 2%
		Fe: 8%
		Sn: 4%
		Mg: 30%

Note. the percentage values of the electronics material are normalized to 100%.

the A2-B coincidence angle is shown in Figure 5. In reality, not all material is aluminum, for example, the propellant tanks contain Hydrazine. However, since the distribution available to us is stated as being aluminum equivalent, we use pure aluminum for the shielding blocks.

For both the upward and downward particle spectra simulations, the primary particle spectra consisted of proton and alpha particle spectra generated by the Badwhar-O'Neill Galactic Cosmic Ray (GCR) model (BO10) (O'Neill, 2010). We use a solar modulation parameter of $\Phi = 627.38$ MV as input for the model, which corresponds to the modulation during the MSL cruise phase (Usoskin et al., 2011). The spectra were computed for a distance of 1 AU. However, the radial gradient of the GCR is on the order of 3% per AU (Gieseler & Heber, 2016). The error induced by the different GCR spectra at Mars' orbit, with a radius of approximately 1.5 AU, is therefore very small when compared to other uncertainties. In addition, the change will tend to balance out in comparison to the underestimation the BO10 will make of the GCR flux when compared to more recent models.

It should be noted that we use parallel particle beams for the cruise phase shielding simulations. In contrast to that, the shielding simulations for the Martian surface, as described in the next section, use angular distributions for the particles generated. The final shielding geometry used in the simulation is also extremely simplified from the real geometry seen in Figure 3. The rationale behind this is that given the uncertainties and the large number of unknowns in the description of the geometry, and given the fact that the GCR has an isotropic angular distribution, our simplified model will be sufficient to reproduce the shielding situation as it is known to the authors.

2.3. The RAD Shielding Enviroment on the Martian Surface

Next, we attempt to simulate the 2-D count density histogram as expected from data taken by RAD on the Martian surface. This is done using an approach consisting of three different modeling steps: First, we use the Planetocosmics code (Desorgher et al., 2006) to determine the expected spectra and intensities of upward and downward directed particles on the Martian surface. Second, the upward directed part of the spectrum

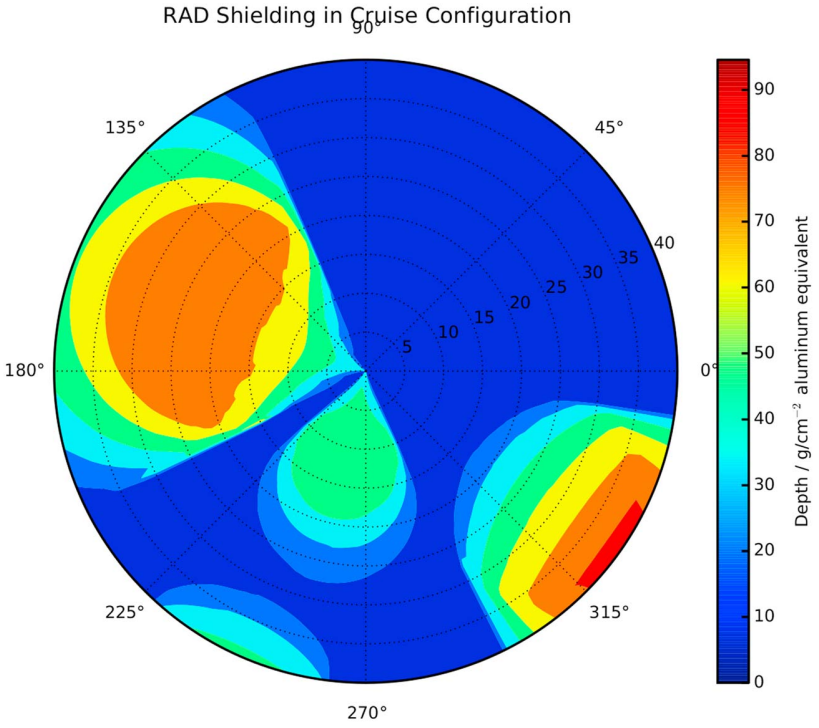

Figure 4. Distribution of shielding densities in the upper A1-B coincidence angle viewcone of the RAD instrument during cruise phase. Note that this shows the full viewcone, while the analysis in this paper only considers the inner viewcone ($0° \leq \theta \leq 18°$). Taken from Zeitlin et al. (2013)

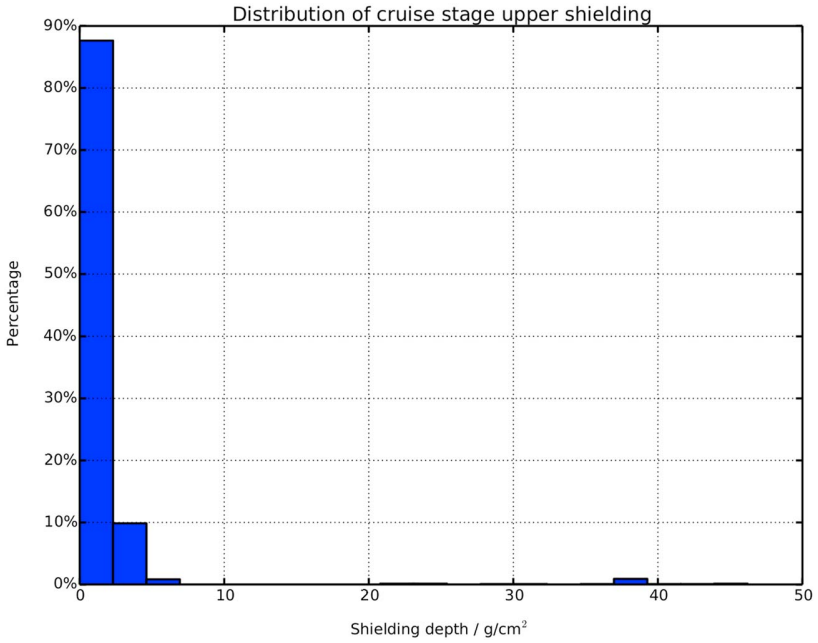

Figure 5. Histogram of shielding distribution inside the upper RAD instrument viewcone as used for constructing the simulation shielding model. It is evident that almost the entire upper viewcone is unshielded.

passes through the body of the MSL rover before being measured by the RAD instrument. This is simulated by modulating the upward Planetocosmics generated spectrum by a second GEANT4 simulation representing the MSL rover body. Finally, we simulate the instrument response to the downward spectra obtained from the Planetocosmics simulations and the upward spectra obtained from the rover body simulation. We then use the results from the RAD instrument simulation to build the 2-D count density matrix as described in section 2.1 and similar to that shown in Figure 2.

We used a version of Planetocosmics updated to utilize Geant4 version 9.6, configured to use the PHITS code (Niita et al., 2006) for ion hadronic interactions, the QGSP_BIC_HP physics list for hadronic interactions, and the emstandard_opt4 physics list for electromagnetic interactions. The simulations for determining the upward and downward directed spectra on the Martian soil were done using a planar geometry with a side length of $l = 3,000$ km to avoid particle losses at the simulation boundaries. We used the Mars Climate Database (Forget et al., 2006) as a model atmosphere, with the atmospheric height being $h = 250$ km. The atmosphere profile is extracted at the location of Gale Crater, using the climatology model, which corresponds to a normal amount of atmospheric dust loading (Forget et al., 2006). The surface pressure of the model atmosphere is $p = 842.72$ Pa, which is the mean pressure during the observation interval (Haberle et al., 2014). The Martian regolith is represented in the Planetocosmics simulation by a 100 m thick layer of SiO_2 with a mass density of 1.7 g cm^{-2}. While this does not represent the exact composition of the soil, we have found through preliminary simulations that this simplification of soil composition does not significantly influence the upward directed particle spectra in the energy range interesting to us. The depth of the soil layer chosen is sufficient to accommodate the maximum of secondary particle production, which occurs at a depth of approximately 1 m (Morthekai et al., 2007).

The input spectra at the top of the Martian atmosphere were proton and alpha particle spectra taken from the Badwhar-O'Neill GCR model as used in section 2.2.

The simulation geometry for simulating the MSL rover body uses a cube with a width and depth of $l = 10$ m and a height of $h = 1$ m. The cube consists of four blocks of different materials: From the bottom, there is a 60 cm high block representing the Martian atmosphere, followed by a 5 mm aluminum plate representing the rover bellypan. This is followed by the MSL rover body as described in section 2.2 with a height of 29 cm, and lastly by a 10.5 cm high block of vacuum used as a particle counting volume. The composition, densities, and dimensions of the different blocks are given in Table 2.

Table 2
Composition, Density and Height of Simulation Boxes

Block	Density	Height	Composition
			CO_2: 95.7%
Atmosphere	$1.92 \cdot 10^{-5}$ $\frac{mg}{cm^3}$	29.0 cm	N: 2.7%
			Ar: 1.6%
Belly plate	2.7 $\frac{g}{cm^3}$	0.5 cm	Al: 100%
			Cu: 20%
			SiO_2: 15%
			PET: 9.9%
			PP: 4.8%
Rover body	0.183 $\frac{g}{cm^3}$	29.0 cm	Al: 2%
			Pb: 2%
			Ni: 2%
			Fe: 8%
			Sn: 4%
			Mg: 30%

Note. The percentage values of the electronics material are normalized to 100%.

The particle source used in the simulations is configured to emit particles in an angular distribution predicted by the Planetocosmics simulations from the bottom area of the simulation. The source uses the upward directed proton, alpha, and neutron particle spectra resulting from the Planetocosmics simulations as described above for generating energy spectra.

Upward directed particle spectra for the RAD instrument simulation are generated from proton and alpha particles reaching the topmost vacuum layer of the simulation. We select only the particles that are within the inner RAD A2-B viewcone of 18°. The downward directed particle spectra are taken directly from the Planetocosmics simulation. We use the downward directed proton and alpha particle spectra from particles selected to be within the inner RAD viewcone.

3. Simulated Particle Fluxes in the RAD Instrument

In the following sections, we describe the particle spectra resulting from our simulations. For the cruise phase, these are the spectra calculated by the shielding simulation inside the MSL spacecraft. The spectra on the Martian surface are from Planetocosmics and the rover body shielding simulation. We describe the particle spectra in an energy range from 10 MeV to 10 GeV, spanning the energy range used in our simulations.

3.1. Cruise Phase Particle Fluxes

The particle spectra derived for the cruise phase are shown in Figure 6.

It is immediately evident that the spectral shape of proton and alpha particle fluxes are largely unchanged, both for the upward and for the downward directed fluxes. Both particle types are also shielded more strongly in the downward direction than in the upward direction.

When comparing integrated particle fluxes in the range from 10 MeV to 10 GeV, the proton upward directed fluxes at RAD are reduced to 92.7% of GCR flux. Downward directed proton fluxes are reduced to 83.7% of GCR flux. In the same energy range, upward directed alpha particle fluxes are reduced to 82.6% of GCR flux, while downward directed alpha particle fluxes are reduced to 69.1% of GCR flux.

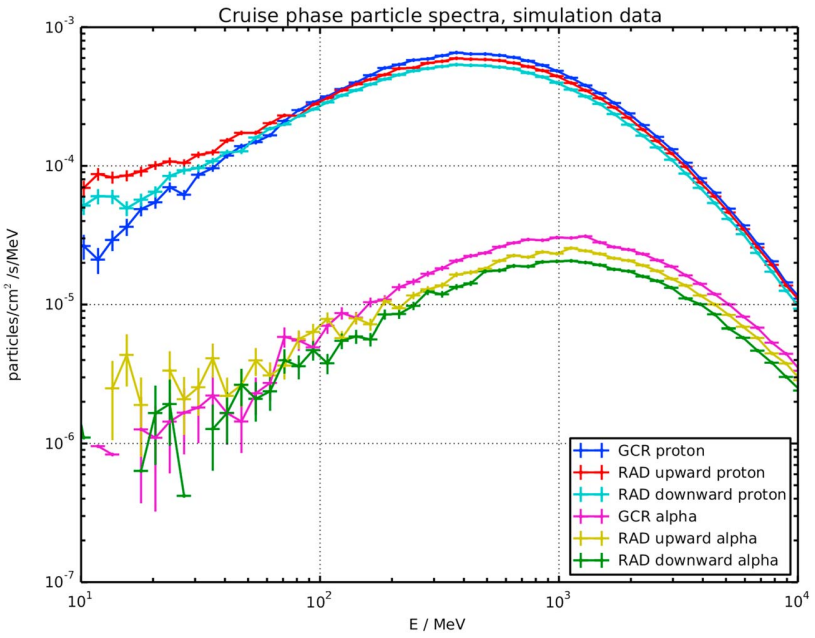

Figure 6. Comparison of downward and upward directed charged particle spectra during the cruise phase outside the spacecraft (labeled as primary) and at the RAD instrument. The fluctuations of the alpha particle spectra below 70 MeV are due to numerical effects.

Table 3
Ratios for Integrated Particle Fluxes During Cruise Phase for Different Particle Species

Particle	RAD up / GCR	RAD down / GCR
Proton	0.927	0.837
Alpha	0.826	0.691

Note. The ratios are computed for energies between 10MeV and 10GeV.

In total, integrated alpha particle fluxes are shielded more strongly than protons, with the difference between the two particle species being 10.1% for upward and 14.6% for downward directed fluxes. Both particle species experience no large reductions in flux due to the spacecraft shielding when compared to the GCR fluxes outside the spacecraft. We summarize the ratios of GCR flux to particle fluxes at the position of RAD in Table 3 for individual particles.

3.2. Particle Fluxes on the Martian Surface

Next, we describe the particle fluxes predicted by our simulations on the Martian surface. Here we have particle fluxes at several different places: On top of the atmosphere, we have the GCR flux, as before for the cruise phase. On the Martian surface, we have the upward and downward particle fluxes as predicted by the Planetocosmics simulation, as well as the upward directed particle fluxes at RAD. The latter, as described in section 2.1, is the upward directed fluxes inside the rover body at RAD, taken from the rover body simulation using the Planetocosmics upward directed fluxes as input.

We show the downward particle fluxes on the Martian surface in Figure 7. While the alpha particle fluxes show the same spectral shape, the proton fluxes are shifted toward a maximum at lower energies. We integrate particle fluxes between 10 MeV and 10 GeV and find that the downward proton flux on the Martian surface is attenuated to 84.2% of GCR flux at the top of the atmosphere. For alpha particles, the flux is reduced to 79.4% of GCR flux.

The upward particle fluxes on the Martian surface are shown in Figure 8. We note that for alpha particles, there are only very low upward fluxes at low energies on the Martian surface, and no particle fluxes inside the rover body at RAD. Protons show a more pronounced upward directed flux, which gets shielded by the rover body below an energy of approximately 300 MeV.

The upward directed alpha particle flux on the Martian surface is 0.02% of the GCR flux, and the proton upward directed flux on the surface is 6.7% of GCR flux. Our simulations predict no upward alpha particle fluxes at RAD. The proton upward flux at RAD is reduced to 52.9% of the upward flux on the Martian surface. When compared to the downward flux on the surface, the upward flux at RAD is reduced to 4.2%. The ratios for the different fluxes are summarized in Table 4.

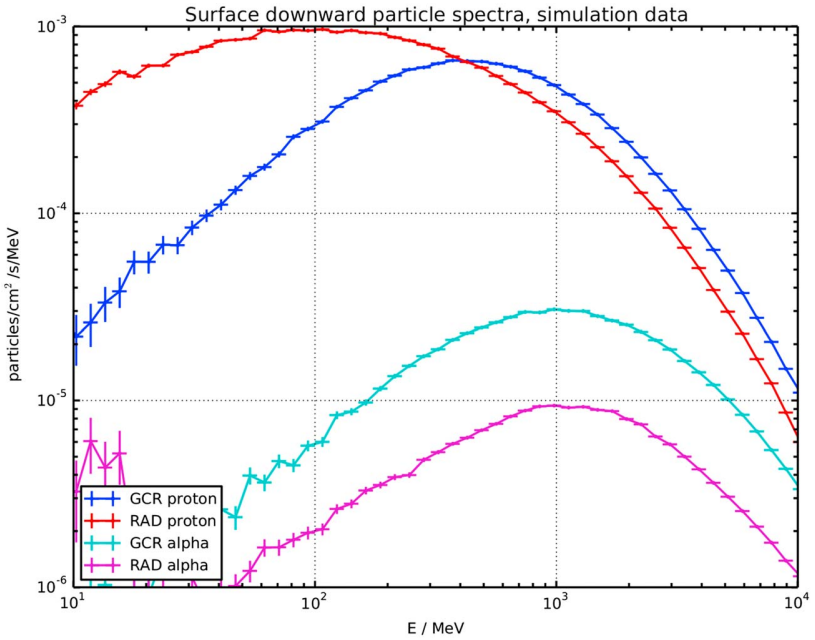

Figure 7. Comparison of GCR particle spectra to downward directed spectra on the Martian surface at soil level. Spectra labeled as primary are the downward GCR spectra on top of the atmosphere.

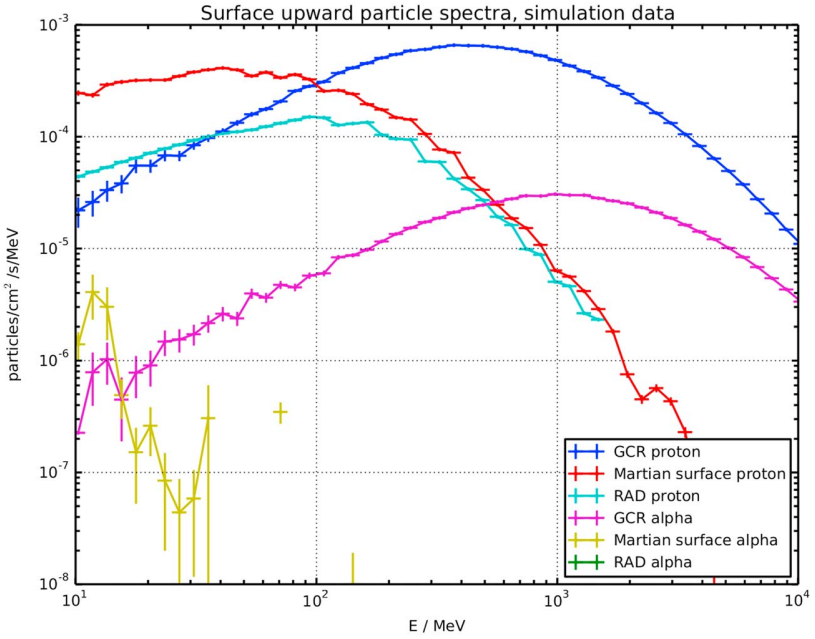

Figure 8. Comparison of GCR particle spectra to upward directed spectra on the surface at soil level and inside the rover body. Spectra labeled as primary are the downward GCR spectra on top of the atmosphere. There are no upward directed alpha particle fluxes predicted inside the rover body.

3.3. Determining Flux Ratios

To discriminate between upward and downward directed fluxes, the method we show in section 2.1 relies on energy deposits in both the D and E scintillator. It is similar to work done by Sierks (1997) for SOHO/Electron, Proton, Helium Instrument (EPHIN) and based on the method presented in McDonald and Ludwig (1964). The use of detector F as an anticoincidence shield means that particles entering the instrument from below will not get registered. The exception to this is penetrating particles that deposit energy in each detector of the instrument. Protons start penetrating RAD at about $E_{\text{prim}} = 100$ MeV, which therefore is the lower boundary for the primary particle energy range in which the flux directions can be distinguished. The upper boundary is given by the point where the two branches merge into the MIPS peak.

For protons, this happens at a primary particle energy of about $E_{\text{prim}} = 200$ MeV. We list the mean energy deposits for protons in the D and E detectors in Table 5. If we compare the $\frac{E_D}{E_E}$ values for the two primary energies shown, we can clearly see that while the values are vastly different for $E_{\text{prim}} = 100$ MeV, they are almost equal at $E_{\text{prim}} = 200$ MeV. We also list the total deposited energy E_{tot} in Table 5, giving us a range of approximately 45 MeV $\leq E_{\text{tot}} \leq$ 100 MeV in which we are able to separate particle flux directions.

The flux intensities of the branches were not derived as absolute values. Instead, the ratio of upward to downward directed flux $R = \frac{I_{\text{up}}}{I_{\text{down}}}$ was computed. To precisely determine the intensity I of the flux directions, we needed to avoid contamination by alpha particles or background. We achieved this by using an integration

Table 4
Ratios of Integrated Fluxes for Different Particle Types on the Martian Surface for Particle Energies Between 10 *MeV and* 10 *GeV*

Particle	$\frac{\text{Upward}}{\text{Downward}}$	$\frac{\text{RAD}}{\text{Upward}}$	$\frac{\text{RAD}}{\text{Downward}}$	$\frac{\text{Downward}}{\text{GCR}}$	$\frac{\text{Upward}}{\text{GCR}}$
Proton	0.079	0.529	0.042	0.842	0.067
Alpha	0.0005	NA	NA	0.794	0.0002

Note. Here downward means downward directed flux at soil level, upward means upward directed flux at soil level before passing the rover, and RAD means upward flux at the RAD instrument after passing the rover. GCR is downward directed GCR fluxes on top of the Martian atmosphere. NA, not application.

Table 5
Mean Energy Deposits in the D and E Detector for Upward and Downward Directed Protons at Different Primary Particle Energies

	E_{prim} = 100 MeV		E_{prim} = 200 MeV	
	Upward	Downward	Upward	Downward
E_D/MeV	81.3 ± 16.5	57.9 ± 3.1	37.9 ± 10.1	36.3 ± 9.4
E_E/MeV	13.2 ± 2.3	24.3 ± 3.4	8.7 ± 2.2	9.5 ± 2.9
$\frac{E_D}{E_E}$	6.2 ± 2.3	2.4 ± 0.5	4.4 ± 2.3	3.8 ± 2.1
E_{tot}/MeV	96.7 ± 16.4	83.2 ± 5.9	47.4 ± 10.5	46.5 ± 10.3

Note. The uncertainties are given by the standard deviation of the selected particles.

method we call branch integration. In the following, we explain this process, using the simulation data shown in Figure 2 as an example.

When plotting the ratio $\frac{E_D}{E_E}$ for one value of total deposited energy E_{tot}, we see upward and downward particles in separate branches as shown earlier in Figure 2. We first select the line of each branch manually in order to obtain a curved path of the branch to follow in the later integration steps. This integration path follows the visual maximum of each branch. As an example, we show the selected upward integration path for simulated cruise phase data as the black line in Figure 9 (left).

Next, we use additional masking to remove the contamination by alpha particles. This contamination can most easily be seen in the upward branch around $E_{tot} \simeq 100$ MeV. We use a polygonal mask in the $\frac{E_D}{E_E}$ versus E_{tot} histograms to remove alpha particle contaminations from the proton data. An example for this mask is shown in Figure 10.

We then integrate the counts contained in the branches. This is done as a two-step process: First, we take single slices in the $\frac{E_D}{E_E}$ axis for each branch, following the selected integration line. We shift the $\frac{E_D}{E_E}$ position for each individual slice of a branch so that they are positioned at the same point. Then, we add all profiles for one branch to obtain the total $\frac{E_D}{E_E}$ profile for that branch. We use the method of shifting the individual profiles to avoid broadening the peak of the branches' profile, which would otherwise happen due to the varying

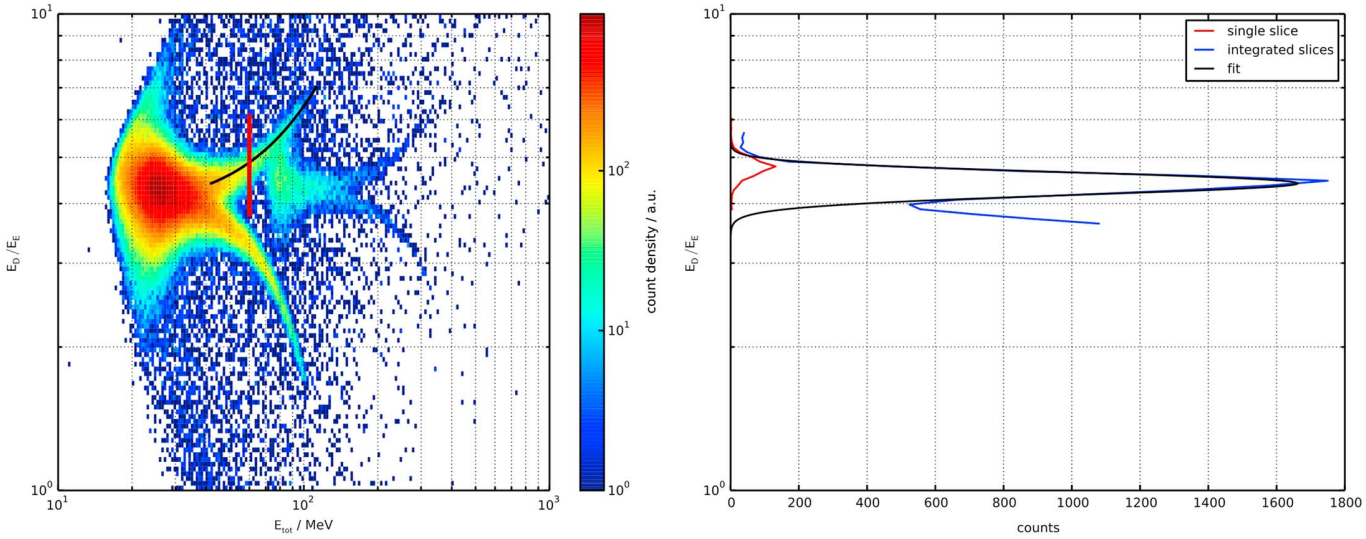

Figure 9. Example demonstrating the branch integration technique used in this analysis on the upward branch of simulated cruise phase data. (left) The data set used in the analysis. The black line is the manually selected integration line for the upward branch. The red line shows the position and extent of one of the slices taken for the branch integration process. (right) The integration results. The red line is the $\frac{E_D}{E_E}$ profile obtained from the single slice marked red in the left figure, which has not yet been shifted in its position on the $\frac{E_D}{E_E}$ axis. The blue line shows the result of the summation of the shifted $\frac{E_D}{E_E}$ profiles of all slices. Note the contamination with alpha particles visible in the profile for $\frac{E_D}{E_E} \leq 4$. The black line is the result of the Gaussian fit to the integrated slices, which is used to obtain the flux intensity of the branch.

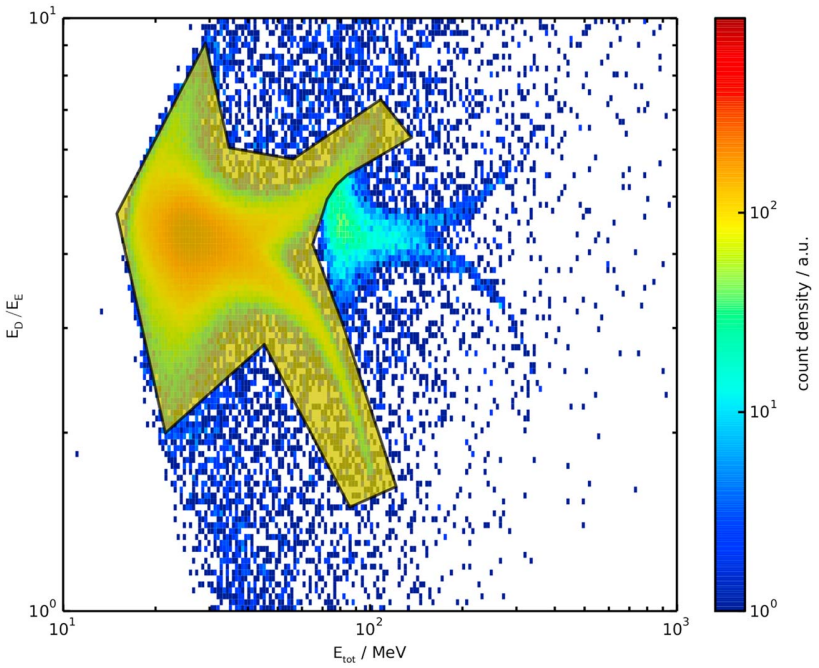

Figure 10. Mask used to separate protons from alpha particle contaminations. The polygonal mask is shown as yellow shade on top of a plot of simulated cruise phase data.

position on the $\frac{E_D}{E_E}$ axis. The position and extent of an individual slice used for integration is shown as a red line in Figure 9 (left) with the corresponding $\frac{E_D}{E_E}$ profile shown in Figure 9 (right). The sum of all individual slices is shown in Figure 9 (right) as a blue line.

In the second integration step, we fit the $\frac{E_D}{E_E}$ profile obtained with a Gaussian and integrate the area below it. This eliminates the background counts that may be present in the profiles. We show the result of the Gaussian fit to the integrated slices in Figure 9 (right) as a black line. Note that the fitted profile excludes the alpha particle contamination visible for $\frac{E_D}{E_E} \leq 4$. The area below the $\frac{E_D}{E_E}$ profiles for the upward and downward branches corresponds to the flux intensity I_{up} and I_{down} for each of the branches. We can then compute the ratio $R = \frac{I_{up}}{I_{down}}$.

In the case of simulation data using parallel beams with no spacecraft shielding as shown in Figure 11, this results in a ratio of $R = 0.77 \pm 0.06$.

In order to calculate the expected flux ratios from simulation data, one needs to be careful when combining the simulation runs for different particle species. We first performed the branch integration on the RAD instrument simulation for each individual particle species. The resulting areas are then scaled by the fluxes obtained from the rover body or the Planetocosmics simulations, respectively. Lastly, we compute the upward to downward flux ratio from the scaled areas.

3.4. Flux Ratios in Simulation Data

The 2-D histogram of the simulated fluxes during the cruise phase is shown in Figure 11. When computing the flux ratio R for an isotropic radiation field, a ratio of $R \simeq 1$ can be expected. From the simulation data, the branch integration yields a flux ratio of $R = 0.98 \pm 0.08$.

The 2-D histogram for the simulated surface data set is shown in Figure 12. The integration of the branches yields a flux ratio of $R = 0.10 \pm 0.01$.

4. Observations of Upward Proton Flux

After having developed the method using simulation data and having applied it to simulated cruise phase and surface data, we now apply it to RAD measurements.

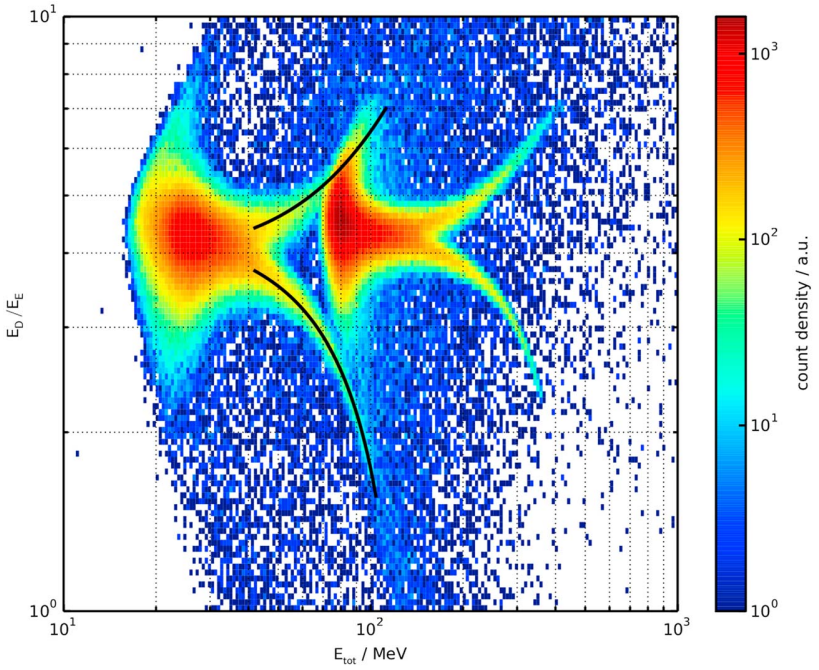

Figure 11. Selected integration lines for integrating along the upward and downward branches in simulation data for parallel particle beams entering the RAD instrument from above and below. The lines are shown in black above the proton upward and downward directed branches. Note that the simulation data shown in this plot is filtered to only contain penetrating particles.

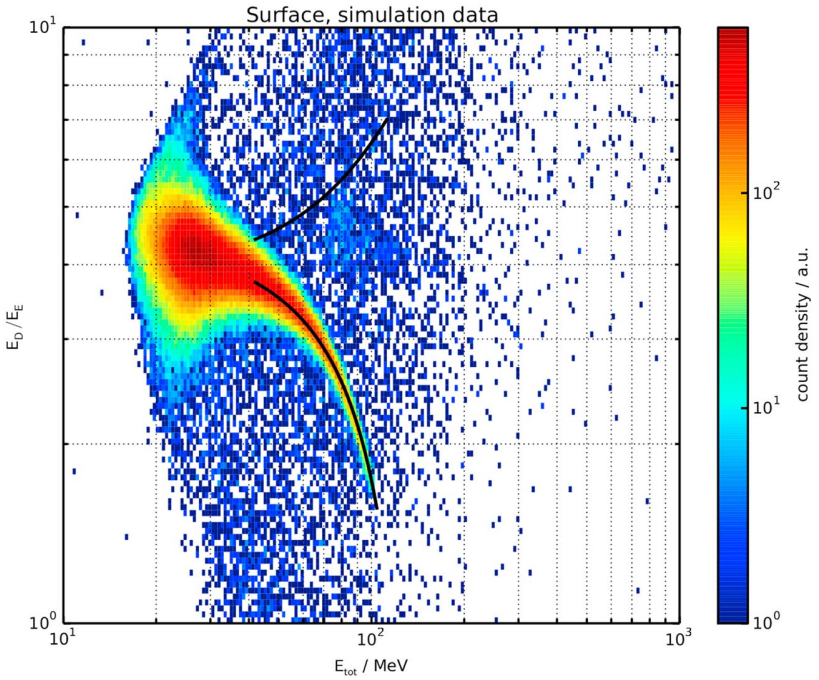

Figure 12. Selected integration lines for integrating along the uwpard and downward branches in simulation data for Martian surface radiation conditions. The lines are shown in black above the proton upward and downward directed branches. Note that the simulation data shown in this plot is filtered to only contain penetrating particles.

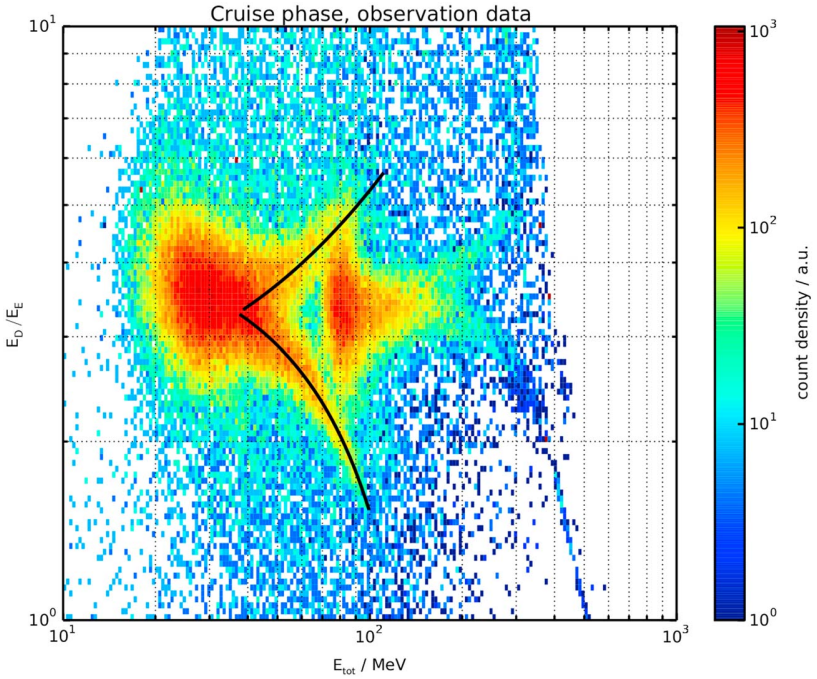

Figure 13. Selected integration lines for integrating along the uwpard and downward branches in cruise phase observation data. The lines are shown in black above the proton upward and downward directed branches. The difference in position on the $\frac{E_D}{E_E}$ axis when compared to simulation and surface data is due to instrument calibration.

4.1. Cruise Phase Data

We analyzed days 1 to 195 of the MSL cruise phase. We exclude all solar particle events, resulting in a total length of 163 days. The integration paths for integrating the branches are shown in Figure 13. The flux ratio derived from this is $R = 0.74 \pm 0.13$.

In RAD cruise phase data, the ratio of upward to downward flux in observation data agrees with the ratio predicted by the simulation using beams of equal intensities without the spacecraft shielding geometry. The ratio predicted by the simulation reproducing shielding conditions inside the MSL spacecraft predicts a 30% higher upward to downward flux.

However, we do not know the shielding conditions in detail, and the simulation uses a simplified geometry. As described in section 2.2, we reduce the geometry to a set of aluminum blocks, whereas the actual spacecraft is made of components of different materials in a complex arrangement. For a uniform shielding distribution, the modification of primary spectra by the shielding should not change the upward downward ratios.

For nonuniformly distributed shielding, upward and downward directed particle fluxes can be shielded differently. This leads to different spectra in the two directions, even when the primary spectra outside the shielding are identical, as would be the case for GCR. Finally, the nonuniform shielding distribution would, even for identical upward and downward fluxes, lead to a change in the upward to downward ratio.

In conclusion, the discrepancy of 30% between simulation results and the observations is a result of the uncertainties in using the simulation setup as described in section 2.2.

4.2. Surface Data

We analyzed surface data for 463 sols, starting from sol 1 to sol 500, again excluding all solar particle events. We note that even when selecting a long time range like the one used here, the upward directed flux is still very low. This is another reason we employed the branch integration process described in section 3.3, which allows us to separate the signal from unwanted contaminations as cleanly as possible. For the branches as shown in Figure 14, we derive a flux ratio of $R = 0.10 \pm 0.02$.

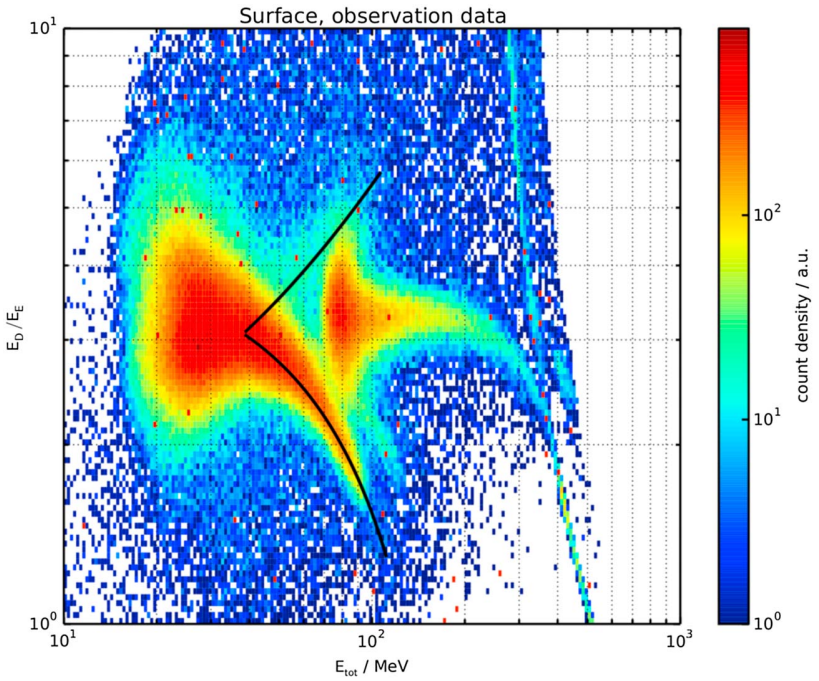

Figure 14. Selected integration lines for integrating along the uwpard and downward branches in surface observation data. The lines are shown in black above the proton upward and downward directed branches. The difference in position on the $\frac{E_D}{E_E}$ axis when compared to simulation and cruise phase data is due to instrument calibration.

5. Discussion

The flux ratios for cruise phase and surface data as well as the corresponding simulation results are shown in Table 6.

The results already consider the numerical uncertainties in the method, which are due to the counting statistics in the simulation. There are other factors influencing the results, of which we list four here and discuss them below:

First, the rover body composition and thus the shielding for the upward directed radiation is not well known, as seen for the results obtained for the cruise phase. Second, the simulation considers only a perfectly even Martian surface with the rover body at all times being perfectly parallel to the surface. However, in reality, local topography will produce variations from these ideal conditions. Third, the influence of secondary particles generated inside the rover body has not been fully considered in this work. Finally, the upward and downward directed particle spectra modeled by the Planetocosmics simulation might not agree well with the real spectra seen on the Martian surface due to uncertainties of the primary spectra, the atmospheric, and soil properties as well as the choice of model and the physics processes considered in the model. We now discuss these four factors in some more details.

The influence of an only partially known shielding geometry has been described in the cruise phase results. We found a discrepancy of approximately 30% between measured and simulated upward to downward flux ratio. This discrepancy is most probably due to the unknowns in shielding geometry and composition. In the simulations for the Martian surface, we only need to consider the lower part of the shielding, since the upper viewcone of the RAD instrument is unshielded by spacecraft structures and the composition and structure of the Martian atmosphere is well known. On the Martian surface, we find good agreement between simulation and observation data. Given that the shielding situation on the surface contains fewer unknowns than the shielding situation during the cruise phase, the good agreement we find is consistent with our conclusions for the cruise phase data. Additionally, we can conclude that the composition and

Table 6
Results of Upward to Downward Flux Ratio Calculations for Cruise Phase and Surface Simulations and Observation Data Sets

	Cruise phase	Surface
Simulation	0.98 ± 0.08	0.10 ± 0.01
Observation	0.74 ± 0.13	0.10 ± 0.02

structure of the rover body is known well enough to allow accurate simulation of the radiation environment on the Martian surface.

The simulation setup for Martian surface conditions assumes a perfectly flat surface with the rover being parallel to it. In reality, however, the surface can be uneven or tilted. Additionally, the terrain next to the rover can be higher or lower than beneath it. This can lead to shielding of the incoming GCR in the upper hemisphere, as well as allowing more of what is here considered the upward directed fluxes to arrive at the instrument. In total, this would lead to a higher upward to downward ratio. However, the observation data used in this analysis cover a long time span, and we only consider particles inside the narrow acceptance angle of about 18° in the vertical direction defined by the A2 and B detectors. The downward flux in this angular range has been shown to be close to isotropic, with only a small amount of shielding (Wimmer-Schweingruber et al., 2015). Based on this, we do not assume that local topography will have a major influence on this analysis. In the future, however, we hope to apply more sophisticated simulations including the tilting of the rover as well as realistic shielding by nearby mountains.

Secondary particles can be generated in the rover body both by upward and downward directed particle fluxes. The simulation setup we used for simulating particle fluxes on the Martian surface does not consider secondary particles generated in the rover body by downward fluxes. We only include secondary particles generated by upward fluxes from the Martian soil. However, the mass of the rover body is miniscule in comparison to the mass of the planet below it. Thus, downward directed particles will mainly produce upward directed secondary particle fluxes from the Martian soil.

The question of how well the particle spectra predicted by the Planetocosmics simulation agree with observed particle spectra is explored in Matthiä et al. (2016). The authors find good agreement between particle spectra measured by the RAD instrument and those predicted by the Planetocosmics simulation code for particle energies below 110 MeV. This suggests that the agreement between measured and simulated particle spectra will be sufficiently good for higher energy ranges as well. However, while Matthiä et al. (2016) considers the influence of high-Z particles in their work, we only consider proton and alpha particles as GCR primaries in our Planetocosmics simulations. Also, their work only treats the downward directed particle fluxes. The upward directed fluxes are not compared in Matthiä et al. (2016) and may be incorrectly predicted by Planetocosmics. Additionally, different solar modulations and atmospheric conditions may result in somewhat different results. Besides, the shielding of the primary fluxes through the atmosphere is also varying as the surface pressure changes seasonally (Guo et al., 2015).

Other authors (Gronoff et al., 2015) have compared the results of different transport models for the Martian surface, in particular the HZETRN code and Planetocosmics. While the upward fluxes are not reported by them, they find good agreement between both models. While it seems plausible that similar modeling results to those we present here could be obtained using other transport codes, the general agreement lets us conclude that our choice of Planetocosmics is valid for the scenario discussed here.

In sum, we use the same information on the shielding geometry as well as the same set of primary spectra for the cruise phase simulations as for the surface simulations. Cruise phase and surface simulations will be equally influenced by uncertainties produced by the primary spectra. However, the simulations reproducing the situation on the Martian surface only depend on the rover body shielding simulation as opposed all of the MSL cruise stage spacecraft needed for the cruise phase simulations. Thus, the uncertainties in shielding geometry and composition will have a lesser influence on surface simulations. Since we found good agreement between simulation and observation on the Martian surface, we conclude that the other sources of uncertainties discussed above do not play a major role.

6. Conclusions

We developed and demonstrated a method for distinguishing between upward and downward directed particle fluxes with the RAD instrument. After compiling known data for the geometry and composition of the shielding masses both during the cruise phase and on the Martian surface, we developed simulation models for both phases. For the cruise phase, reasonable agreement for the upward to downward ratio was found between RAD instrument data and simulation data. On the Martian surface, we found good agreement between simulation and observation data. While this will need to be confirmed e.g. by evaluating the upward and downward fluxes for particles other than protons, or by evaluating the fluxes for different time ranges on

the Martian surface, we conclude that we can simulate the Martian radiation environment in enough detail to reproduce our observations.

The method presented here allows for distinguishing between flux directions. It is also a first step in the goal of extending charged particle spectra measurements from the design limit of 10MeV to 100MeV stated in Hassler et al. (2012) up to 200 MeV. During the branch integration, the upward and downward fluxes in that energy range are integrated. The downward integrated flux can directly be used as an extension of the existing flux histograms. This will be a significant extension of the instruments' design capabilities as outlined in Hassler et al. (2012) and will be of considerable value for future work. The method is also an implementation of the idea to use particles penetrating the detector stack for in-depth analysis as outlined in Posner et al. (2005).

Acknowledgments
RAD is supported by NASA (HEOMD) Mars Science Laboratory Mission and Science Investigation, under JPL subcontract 1273039 to Southwest Research Institute and in Germany by DLR and DLR's Space Administration grants 50QM0501 and 50QM1201 to the Christian Albrechts University, Kiel. Part of this research was carried out at the Jet Propulsion Laboratory, California Institute of Technology, under a contract with the National Aeronautics and Space Administration. In particular, we would like to extend sincere gratitude to Jeff Simmonds, Ashwin Vasavada, and Joy Crisp at JPL, Gale Allen, Michael Meyer, Chris Moore, Victoria Friedensen at NASA HQ, and Heiner Witte at DLR in Germany for their unwavering support of RAD over the years. The RAD instrument data used in the analysis presented here are available in the NASA Planetary Data System at http://ppi.pds.nasa.gov/search/view/?f=yes&id=pds://PPI/MSL-M-RAD-2-EDR-V1.0

References

Agostinelli, S., Allison, J., Amako, K., Apostolakis, J., Araujo, H., Arce, P., … Zschiesche, D. (2003). Geant4—A simulation toolkit. *Nuclear Instruments and Methods in Physics Research Section A: Accelerators, Spectrometers, Detectors and Associated Equipment*, *506*(3), 250–303. https://doi.org/10.1016/S0168-9002(03)01368-8

Allison, M. (1997). Accurate analytic representations of solar time and seasons on Mars with applications to the Pathfinder/Surveyor missions. *Geophysical Research Letters*, *24*, 1967–1970. https://doi.org/10.1029/97GL01950

Böhm, E. (2004). Neutron detection with scintillation counters (Tech. Rep.). Kiel, Germany: Christian-Albrechts-University of Kiel.

Desorgher, L., Flückiger, E. O., & Gurtner, M. (2006). The PLANETOCOSMICS Geant4 application. In *36th COSPAR Scientific Assembly*. Beijing.

Edquist, K. T., Hollis, B. R., Johnston, C. O., Bose, D., White, T. R., & Mahzari, M. (2014). Aerothermodynamic design of the Mars Science Laboratory heatshield. *Journal of Spacecraft and Rockets*, *51*(4), 1106–1124. https://doi.org/10.2514/6.2009-4078

Ehresmann, B., Zeitlin, C., Hassler, D. M., Wimmer-Schweingruber, R. F., Bohm, E., Bottcher, S., … Reitz, G. (2014). Charged particle spectra obtained with the Mars Science Laboratory Radiation Assessment Detector (MSL/RAD) on the surface of Mars. *Journal of Geophysical Research: Planets*, *119*, 468–479. https://doi.org/10.1002/2013JE004547

Forget, F., Millour, E., & Lebonnois, S. (2006). The new Mars climate database. In *Second workshop on Mars atmosphere modelling and observations*. Granada, Spain.

Gieseler, J., & Heber, B. (2016). Spatial gradients of GCR protons in the inner heliosphere derived from Ulysses COSPIN/KET and PAMELA measurements. *Astronomy & Astrophysics*, *589*, A32. https://doi.org/10.1051/0004-6361/ 201527972

Gronoff, G., Norman, R. B., & Mertens, C. J. (2015). Computation of cosmic ray ionization and dose at Mars. I: A comparison of HZETRN and Planetocosmics for proton and alpha particles. *Advances in Space Research*, *55*(7), 1799–1805. https://doi.org/10.1016/j.asr.2015.01.028

Grotzinger, J. P., Crisp, J., Vasavada, A. R., Anderson, R. C., Baker, C. J., Barry, R., … Wiens, R. C. (2012). Mars Science Laboratory Mission and science investigation. *Space Science Reviews*, *170*, 5–56. https://doi.org/10.1007/s11214-012-9892-2

Guo, J., Zeitlin, C., Wimmer-Schweingruber, R. F., Rafkin, S., Hassler, D. M., Posner, A., … Reitz, G. (2015). Modeling the variations of dose rate measured by RAD during the first MSL Martian year: 2012–2014. *The Astrophysical Journal*, *810*(1), 24. https://doi.org/10.1088/0004-637X/810/1/24

Haberle, R. M., Gomez-Elvira, J., de la Torre Juarez, M., Harri, A.-M., Hollingsworth, J. L., Kahanpää, H., … Zorzano- Mier, M.-P. (2014). Preliminary interpretation of the REMS pressure data from the first 100 sols of the MSL mission. *Journal of Geophysical Research: Planets*, *119*, 440–453. https://doi.org/10.1002/2014JE004657.Received

Hassler, D. M., Zeitlin, C., Wimmer-Schweingruber, R. F., Böttcher, S., Martin, C., Andrews, J., … Cucinotta, F. A. (2012). The radiation assessment detector (RAD) investigation. *Space Science Reviews*, *170*(1-4), 503–558. https://doi.org/10.1007/s11214-012-9913-1

Hassler, D., Zeitlin, C., Wimmer-Schweingruber, R. F., Ehresmann, B., Rafkin, S., Eigenbrode, J. L., … t. M. S. Team (2014). Mars' surface radiation environment measured with the Mars Science Laboratory's curiosity rover. *Science*, *343*(6169), 1244,797–1244,797. https://doi.org/10.1126/science.1244797

Matthiä, D., Ehresmann, B., Lohf, H., Köhler, J., Zeitlin, C., Appel, J., … Wimmer-Schweingruber, R. F. (2016). The Martian surface radiation environment—A comparison of models and MSL/RAD measurements. *Journal of Space Weather and Space Climate*, *6*, A13. https://doi.org/10.1051/swsc/2016008

McDonald, F. B., & Ludwig, G. H. (1964). Measurement of low-energy primary cosmic-ray protons on IMP-1 satellite. *Physical Review Letters*, *13*(26), 783–785. https://doi.org/10.1103/PhysRevLett.13.783

Morthekai, P., Jain, M., Dartnell, L., Murray, A., Bøtter-Jensen, L., & Desorgher, L. (2007). Modelling of the dose-rate variations with depth in the Martian regolith using GEANT4. *Nuclear Instruments and Methods in Physics Research Section A: Accelerators, Spectrometers, Detectors and Associated Equipment*, *580*(1), 667–670. https://doi.org/10.1016/j.nima.2007.05.118

Müller-Mellin, R., Kunow, H., Fleißner, V., Pehlke, E., Rode, E., Röschmann, N., … Henrion, J. (1995). COSTEP—Comprehensive suprathermal and energetic particle analyser. In B. Fleck, V. Domingo, & A. Poland (Eds.), *The SOHO mission* (pp. 483–504). Dordrecht: Springer Netherlands. https://doi.org/10.1007/978-94-009-0191-9_13

Niita, K., Sato, T., Iwase, H., Nose, H., Nakashima, H., & Sihver, L. (2006). PHITS—a particle and heavy ion transport code system. *Radiation Measurements*, *41*(9-10), 1080–1090. https://doi.org/10.1016/j.radmeas.2006.07.013

Ogunniyi, I. O., Vermaak, M. K. G., & Groot, D. R. (2009). Chemical composition and liberation characterization of printed circuit board comminution fines for beneficiation investigations. *Waste management (New York, N.Y.)*, *29*(7), 2140–6. https://doi.org/10.1016/j.wasman.2009.03.004

O'Neill, P. (2010). Badhwar-o'neill 2010 galactic cosmic ray flux model—Revised. *IEEE Transactions on Nuclear Science*, *57*(6), 3148–3153. https://doi.org/10.1109/tns.2010.2083688

Posner, A., Hassler, D. M., McComas, D. J., Rafkin, S., Wimmer-Schweingruber, R. F., Böhm, E., & Heber, B. (2005). A high energy telescope for the solar orbiter. *Advances in Space Research*, *36*(8), 1426–1431. https://doi.org/10.1016/j.asr.2004.11.040

Reitz, G., Berger, T., Bilski, P., Facius, R., Hajek, M., Petrov, V., … Dettmann, J. (2009). Astronaut's organ doses inferred from measurements in a human phantom outside the international space station. *Radiation Research*, *171*(2), 225–235. https://doi.org/10.1667/RR1559.1

Sierks, H. (1997). Messung geladener teilchen mit dem kieler instrument EPHIN an bord der SOHO-raumsonde, Ph. D. thesis. Kiel, Germany: Christian-Albrechts-University of Kiel.

Tran, H., Johnson, C., Rasky, D., Hui, F., Hsu, M.-T., & Chen, Y. (1996). Phenolic impregnated carbon ablators (PICA) for Discovery class missions. In *31st Thermophysics Conference*. Reston, Virginia: NASA, American Institute of Aeronautics and Astronautics. https://doi.org/10.2514/6.1996-1911

Usoskin, I. G., Bazilevskaya, G. A., & Kovaltsov, G. A. (2011). Solar modulation parameter for cosmic rays since 1936 reconstructed from ground-based neutron monitors and ionization chambers. *Journal of Geophysical Research*, *116*, A02104. https://doi.org/10.1029/2010JA016105

Wimmer-Schweingruber, R. F., Köhler, J., Hassler, D. M., Guo, J., Appel, J.-K., Zeitlin, C., … Cucinotta, F. (2015). On determining the zenith angle dependence of the Martian radiation environment at Gale Crater altitudes. *Geophysical Research Letters*, *42*, 10,557–10,564. https://doi.org/10.1002/2015GL066664

Zeitlin, C., Hassler, D. M., Cucinotta, F. A., Ehresmann, B., Wimmer-Schweingruber, R. F., Brinza, D. E., … Reitz, G. (2013). Measurements of energetic particle radiation in transit to mars on the Mars Science Laboratory. *Science*, *340*(6136), 1080–1084. https://doi.org/10.1126/science.1235989

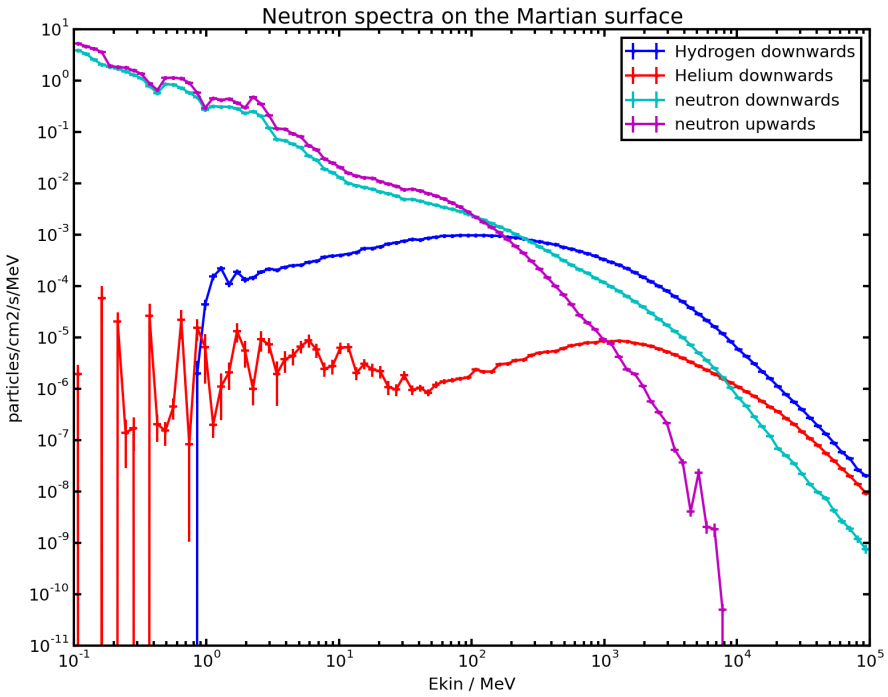

Figure 6.1: Planetocosmics simulation of energy spectra for upward- and downward-directed neutron particle fluxes on the Martian surface. The spectra of downward hydrogen and helium fluxes are shown for comparison.

6.2 OBSERVING DIRECTIONALITY OF NEUTRAL PARTICLES

Knowing the neutron radiation environment is very important for correctly assessing the habitability of the Martian surface. Neutrons contribute a large part to the dose deposited in biological tissue due to the high hydrogen content in such tissues. At the same time, neutrons are abundant in the Martian radiation environment, both from above and from below. This is evident when looking at Planetocosmics simulation data as shown in Fig. 6.1.

The neutron flux on the Martian surface has been measured by the RAD instrument (Köhler et al. (2011), Hassler et al. (2014)). Since neutron detection in RAD works omnidirectionally, the upward directed particles are part of the measurements made. However, a distinction between the neutron directions cannot be made using RAD.

One particularly interesting point when considering upward neutron fluxes is their sensitivity to soil water content. Neutrons can interact very efficiently with the hydrogen in water, since the hydrogen nuclei have almost exactly the same mass as neutrons, making energy transfer in elastic collisions very efficient. Thus, the content of hydrogen in the soil influences the upward neutron fluxes on the Martian surface. Modeling results of this effect, obtained using

Planetocosmics, are shown in Fig. 6.2, showing large variations in upward-directed neutron fluxes for different soil water contents.

The neutron flux is influenced by soil hydrogen content over an energy range in which neutrons are typically classified as two different energy classes (Krieger, 2007). Thermal neutrons have a kinetic energy that has been equalized to that of the ambient medium by repeated collisions. This corresponds to an energy of approximately $0.0252\,eV$ for an ambient medium at room temperature. Neutrons at higher energies with $E_{kin} \leqslant 0.5\,eV$ are called epithermal neutrons.

The flux of downward neutrons is independent of soil hydrogen content. The upward flux, however, is dependent on it, meaning that the ratio of upward to downward flux can be used to determine soil hydrogen content. A similar measurement has been done previously by the Dynamic Albedo of Neutrons (DAN) instrument using active measurements, i. e., using a neutron source. Using the instrument concept presented here, such a measurement could be done passively by an instrument designed to fulfill another role. This enables the instrument to provide more measurements at the same payload cost.

The previous section, 6.1 , presented a method for distinguishing charged particle directionality. This method is based on particles making deterministic energy deposits in a detector depending on their primary energy. However, neutrons deposit energy stochastically, meaning that the energy deposited by a neutron passing through a detector, E_{dep}, is random within the interval $0 \leqslant E_{dep} \leqslant E_{kin}$. Because of this ambiguity of the deposited energy, the method presented above cannot be used to determine neutron directionality. Here, an instrument concept capable of measuring the directionality of neutrons will be presented, and its capabilities assessed through simulations.

6.2.1 *Instrument Concept*

Charged and neutral particles interact with matter in a fundamentally different way, as explained in Krieger (2007) and a multitude of other literature. Charged particles interact mainly with the electrons in the atoms through Coulomb interactions. This leads to them undergoing a deterministic mean energy loss per length when transversing matter. This has been described first by Bethe (1930) as a relationship known as the Bethe-Bloch equation.

Neutrons interact mainly with the atoms nuclei. They lose energy stochastically, with the energy loss per interaction according to $0 \leqslant E_{loss} \leqslant E_{kin}$. The method presented above for determining charged particle directionality relies on deterministic deposits of energy into different detectors. Due to the stochastic nature of neutron energy losses, this method is not applicable for neutron directionality determinations. Instead, the instrument presented here uses a Time of Flight (ToF) system composed of two detectors vertically separated

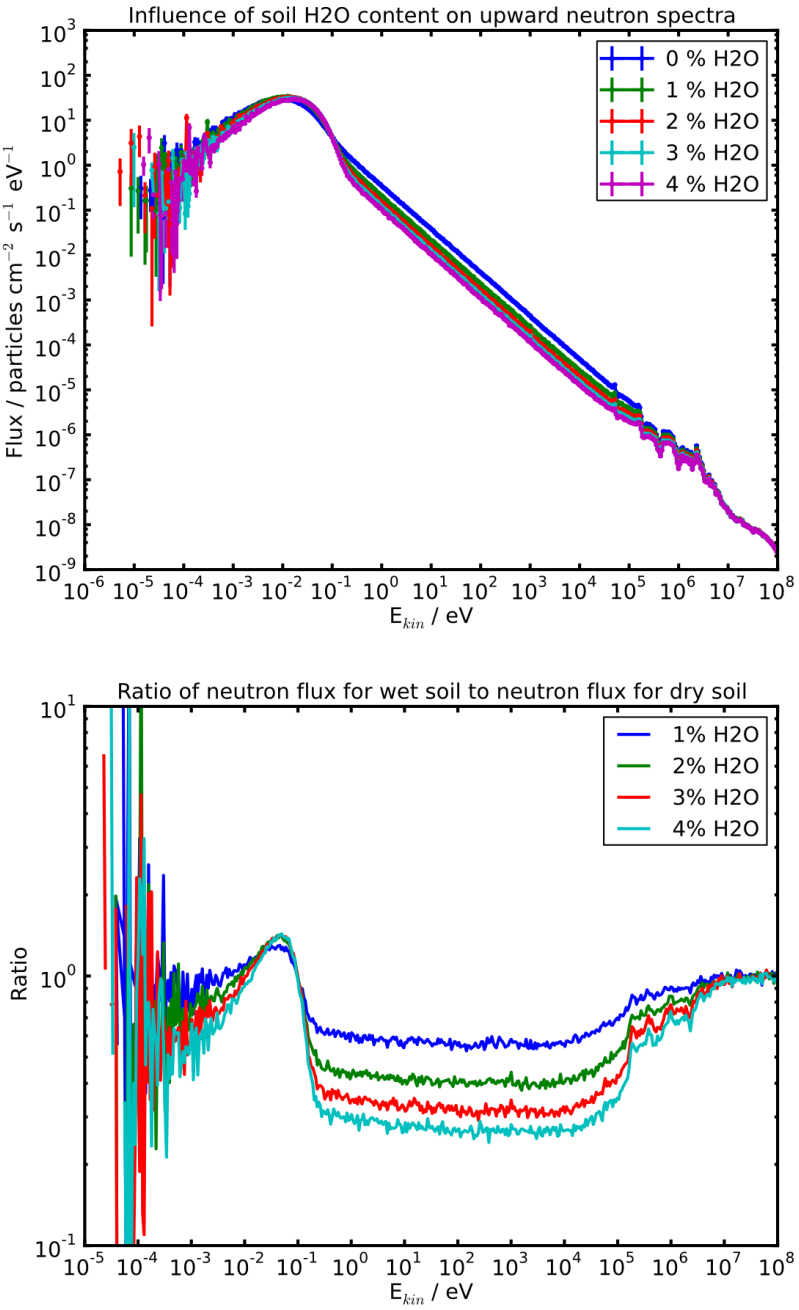

Figure 6.2: Planetocosmics simulation of energy spectra for upward-directed neutron particle fluxes. Spectra are shown for different soil hydrogen contents. The upper figure shows the neutron energy spectra, the lower figure shows the ratio of upward neutron spectra for various soil hydrogen contents to the upward neutron spectrum with no hydrogen in the soil.

by a small distance. The time difference between one neutrons signal in the bottom and top detector $\Delta t = t_{bottom} - t_{top}$, where t_{bottom} and t_{top} are the detection times in the bottom and top detectors, is used to discriminate between particle directions. If $\Delta t > 0$, the particle has entered the detector from above, and if $\Delta t < 0$, it has entered from below. In order to detect particles, the two detectors need to be sufficiently distant. This distance is easily computed given some assumptions. If the instrument is to resolve neutron directionality up to a particle energy of $10\,MeV$, and assuming that the ToF detection system is able to detect time differences of $\Delta t \geqslant 10\,ns$, the needed separation of both detectors is $4\,cm$.

An instrument concept called Radiation, neutron Albedo, and Mapping of hydrogen (RAMA) has been developed for possible conclusion on the NASA Mars 2020 mission. The instrument is described in detail in Hassler (2015), and a general description of the concept as well as the aspects developed as part of this thesis are given below. A Computer Aided Design (CAD) sketch of the instrument is shown in Fig. 6.3. Logically, the instrument is split into two subsystems, which share much of the hardware. The Neutron Directionality Sensor (NDS) measures thermal, epithermal and fast neutron direction and energy, while the Hydrogen Detection Sensor (HDS) measures soil hydrogen content. The detectors of the NDS are two layers of plastic scintillator cubes. The layers are separated by a distance of $5\,cm$. Each detection layer contains two scintillation cubes with a side length of $2\,cm$ each. The scintillators are read out by a Photo-Multiplier Tube (PMT). A Silicon SSD covers the top of the lower scintillator layer and the bottom of the upper layer. The SSD are used as an anti-coincidence system to reject charged particles that enter the NDS detection system. Additionally, they would be used for charged particle dosimetry, however, this aspect will not be discussed here.

When a fast neutron enters the detector system from either above or below, it can deposit energy in a scintillator in both layers by elastic scattering. Fast neutrons are thus characterized by a double pulse, with one pulse in each scintillator layer.

The energy measurement by ToF is viable for energies up to $10\,MeV$. The relationship between ToF and neutron energy is determined by Geometry and Tracking version 4 (Geant4) simulations. However, the energy resolution offered by the ToF method is limited. Therefore, for energies from $0.3\,MeV$ to $3\,MeV$, neutron spectroscopy is done via a process called "capture gating". The scintillator material in both layers is doped with ^{10}B. A neutron entering the scintillator can get thermalized through multiple scatterings, and the thermal neutron can then be captured by the Boron (Balmer, Gamage, and Taylor, 2014). This capture reaction gives a characteristic pulse amplitude and timing distribution. A neutron in this energy range is then characterized by a triple pulse, with the first pulse from energy deposits by scattering in

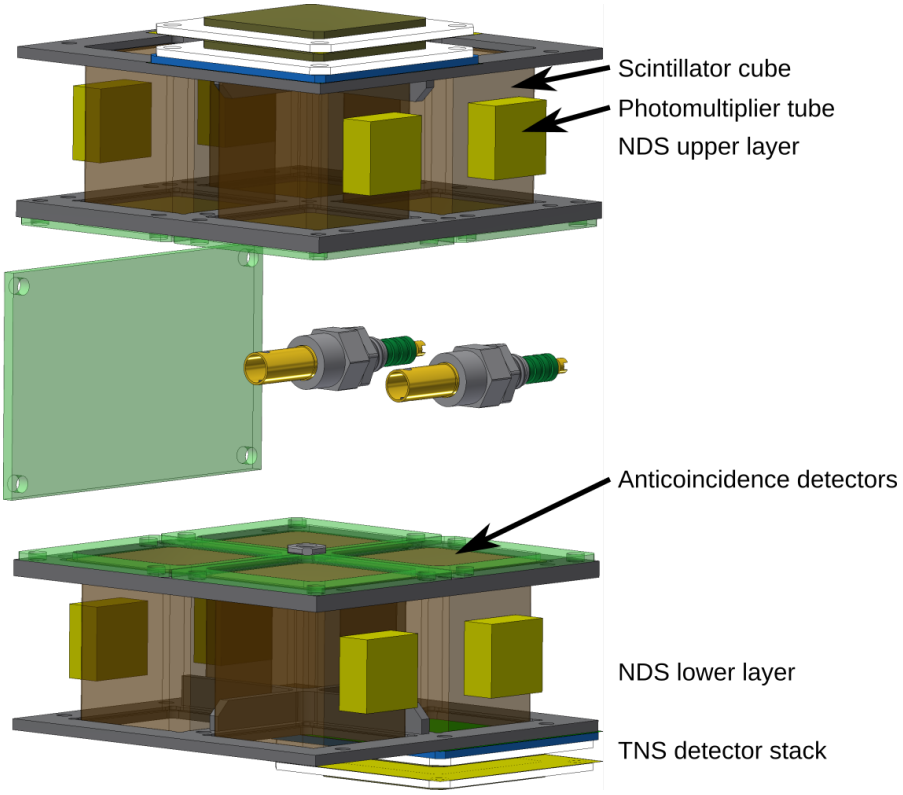

Figure 6.3: Sketch of the Radiation, neutron Albedo, and Mapping of hydrogen (RAMA) instrument design for detecting the directionality of neutron particles. The two Neutron Directionality Sensor (NDS) layers are shown, as well as the anti-coincidence detectors and the Thermal Neutron Sensor (TNS) stack. Image courtesy of L. Seimetz.

the first scintillator layer, the second pulse in the second layer from the neutron thermalizing, and the third pulse from the Boron capture. The total neutron energy is given by the sum of all three pulses.

Thermal neutrons are detected in the Thermal Neutron Sensor (TNS), which is a Silicon SSD covered by a Gadolinium foil. Thermal neutrons are captured in the Gadolinium, giving off conversion electrons in the reaction. These electrons are then detected in the SSD. Epithermal neutrons are detected in the lower scintillator layer of the NDS. The scintillators are wrapped in Cadmium foil of sufficient thickness to stop approximately 99 % of thermal neutrons, while higher energy particles enter the scintillator and are detected only by the Boron capture flash. The HDS utilizes the same detector hardware as the NDS, resulting in a mass efficient instrument. The energy ranges in which neutrons are affected by soil hydrogen content are thermal and epithermal neutrons, as shown in Fig. 6.2.

6.2.2 *Capabilities and Preliminary Simulations*

The instrument's capabilities have been assessed in a series of simulations, of which the NDS simulations were done within the scope of this thesis. In particular, detection efficiencies, neutron directionality and energy determinations and the influence of subsurface hydrogen on the upward neutron spectra have been investigated.

The simulations to assess the performance of the detection system were performed using a simpler geometry than that of the final proposed instrument design. This is simply because the use of four scintillation detectors per detection layer in the NDS was a late addition designed to provide some angular resolution. The geometry used for the simulation of detector performance is shown in Figure 6.4. The dimensions of the simulation geometry are noted in the figure description. This geometry has been used for all of the following simulations, except where otherwise noted.

A set of simulations was performed to assess the range of values for the ToF measurements of neutrons. A neutron beam was simulated entering the detector from above and below, parallel to the vertical axis of the detector. The simulation code used, Geant4, gives the energy deposited in a detector for each particle, as well as the time the particle enters (t_{enter}) and leaves (t_{leave}) the detector volume. The energy deposit then has to have occurred at a time $t_{deposit}$ with $t_{enter} \leqslant t_{deposit} \leqslant t_{leave}$. Here, it was simply assumed that $t_{deposit} = (t_{leave} - t_{enter})/2$, and $t_{deposit}$ for detector 1 and detector 2 labeled t_1 and t_2, respectively. We then define the time between deposits as

$$\Delta t = t_2 - t_1 \tag{6.1}$$

meaning that $\Delta t > 0$ indicates a particle traveling downward through the detector system, and $\Delta t < 0$ indicates one traveling upward.

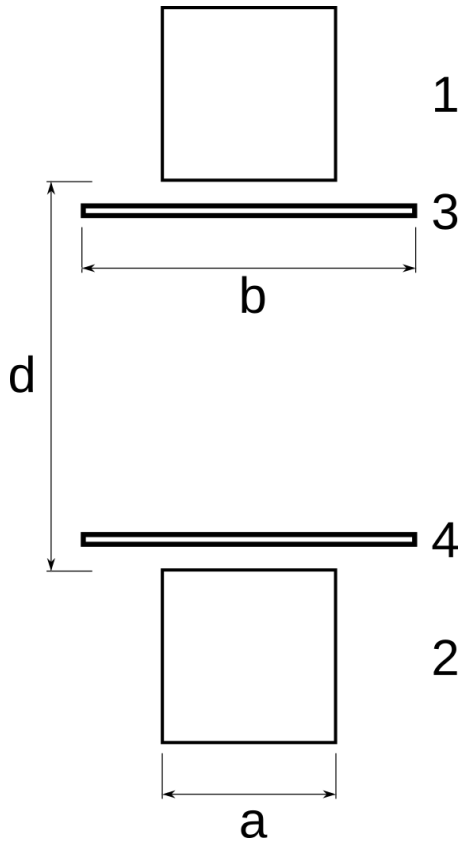

Figure 6.4: Geometry used for simulating the Neutron Directionality Sensor (NDS). Detectors 1 and 2 are the scintillation detector cubes with a side length of $a = 30.75\,mm$, detectors 3 and 4 are the Silicon Solid State Detector (SSD) anti-coincidence detectors with a side length of $b = 50\,mm$. The distance between detectors 1 and 2 is $d = 100\,mm$.

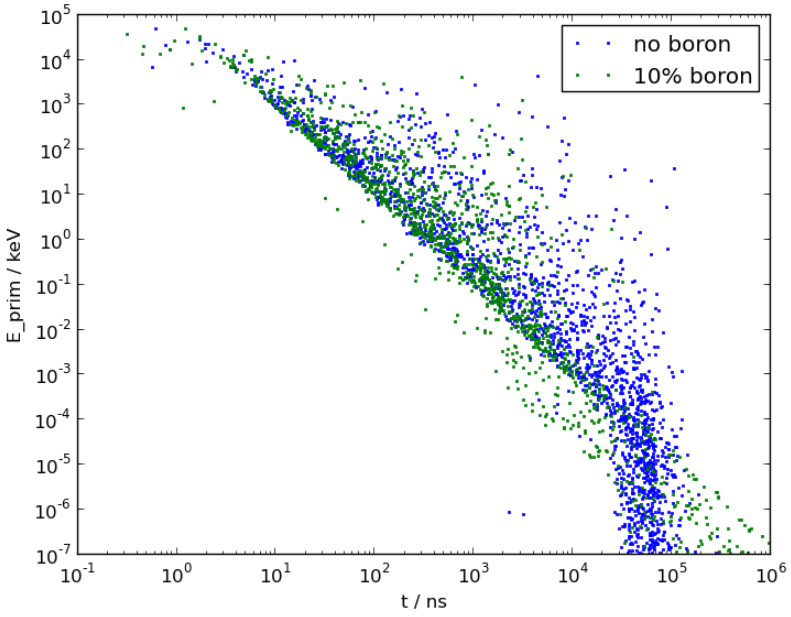

Figure 6.5: Plot showing the primary particle energy E_{prim} versus time difference $|\Delta t|$ for the Neutron Directionality Sensor (NDS). Time differences are shown both for scintillation detectors of pure BC-432m and for ones with 10 % Boron doping added.

Figure 6.5 shows a plot of primary particle energy E_{prim} over $|\Delta t|$. The values of Δt predicted by the simulations range from $\Delta t = 1\,ns$ for particle energies of $E_{prim} = 10\,MeV$ to $\Delta t = 1\,ms$ for energies of $E_{prim} = 1 \times 10^{-7}\,keV$.

The detection and rejection efficiencies of the NDS detector system are an important metric to assess the overall performance of the design. They were assessed in a series of Geant4 simulations. In the following, the term detection efficiency is defined as the probability of a particle to generate a signal in both the upper and lower scintillation detector, i. e., detectors 1 and 2 in Figure 6.4. Rejection efficiency then is the probability of generating a signal in the Silicon SSD anti-coincidence detectors 3 and 4. A false positive, or false detection, is a charged particle generating signals in the scintillation detectors 1 and 2, but not in the anti-coincidence detectors. Similarly, a false negative, or false rejection, is a neutron generating signals in the anti-coincidence detectors, thus being rejected as a charged particle.

Two separate sets of simulations to assess the detection and rejection efficiencies were carried out. First, particles were emitted in a parallel vertical beam with a diameter of 20 mm with the beam passing through all four detectors. It should be noted that the scintillation detectors in this simulation are composed of BC-432m, the same material used in the RAD instrument for the E and F detectors. The Boron

particle		**efficiency / %**
neutron	detection	0.29
	rejection	0.36
gamma	detection	0.03
	rejection	41.54
proton	detection	1.11
	rejection	99.29
electron	detection	1.20
	rejection	99.29

Table 6.1: Detection and rejection efficiencies computed from simulations of the Neutron Directionality Sensor with 10 % Boron doping in the scintillation detectors. Particles are required to have deposited energy in either detector 1 or detector 2 in order to be considered valid.

doping was introduced in a later step. The simulation was carried out using both proton and neutron particle beams. For neutrons, a detection efficiency of 0.36 % was computed, of which 0.81 % were false rejections. The rejection probability for the proton beam was 99.99 %.

The second set of simulations model an isotropic angular distribution of primary particles and introduce a Boron doping for the scintillation detectors. The composition of the detectors was still modeled as BC-432m, with the addition of 10 % by mass of Boron added. Simulations were carried out for neutron, proton, gamma, and electron particles. The particles were emitted from a square with a side length of 200 mm above detector 1, traveling downward along the vertical axis with a cosine law angular distribution. The detection and rejection efficiencies computed from those simulations are given in Table 6.1. So far, the simulations have not considered any additional mass between the two NDS detection layers. The possibility of maintaining instrument performance with structural or electronics masses between the two detection layers would ease the instruments construction constraints, allowing for a more flexible layout. In order to assess this, two additional sets of simulations were performed with mass added between the detector layers. Additionally, mass was added to the side of the detectors to represent the detector housing. The modified geometry is shown in Figure 6.6. Two sets of simulations were run with different configuration for the added mass. The first was using a plate of Aluminum with a thickness of 2 mm. The second was modified to include a layer of Printed Circuit Board (PCB)-like material with a thickness of 1 mm sandwiched between two layers of Aluminum with a thickness of 1 mm each. The mass density of the PCB-like material was $\rho = 0.183\,\mathrm{g\,cm^{-3}}$, with a composition as taken from Ogunniyi, Vermaak, and Groot (2009) and shown in Table 6.2.

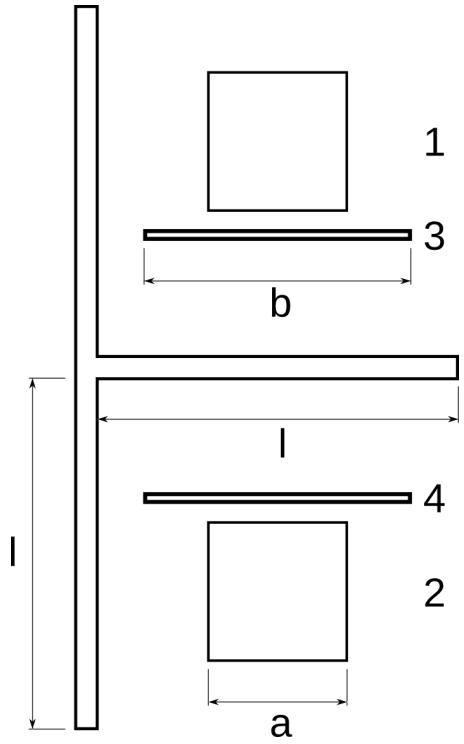

Figure 6.6: Modified geometry used for simulating Neutron Directionality Sensor (NDS) performance with mass added to the side of and between the detector layers. Dimensions and detector distance are identical to those in Figure 6.4 ($a = 30.75\,mm$, $b = 50\,mm$, distance between detectors 1 and 2 is $d = 100\,mm$). The arm length of the added mass is $a = 100\,mm$.

material	percentage
Cu	20 %
SiO_2	15 %
PET	9.9 %
PP	4.8 %
Al	2 %
Pb	2 %
Ni	2 %
Fe	8 %
Sn	4 %
Mg	30 %

Table 6.2: Composition of Printed Circuit Board (PCB)-like material used in the simulation of the Neutron Directionality Sensor (NDS). The sum of the percentage values are normalized to 100 % in the simulations. Values are taken from Ogunniyi, Vermaak, and Groot (2009).

particle		efficiency Al. / %	efficiency Al. & PCB / %
neutron	detection	0.29	0.30
	rejection	0.92	0.92
gamma	detection	0.03	0.03
	rejection	42.14	45.80
proton	detection	0.79	0.79
	rejection	99.34	99.34
electron	detection	0.88	0.88
	rejection	99.38	99.38

Table 6.3: Detection and rejection efficiencies computed from simulations of the modified Neutron Directionality Sensor (NDS) geometry with structural elements added between the detection layers and to the side of the detector. Particles are required to have deposited energy in either detector 1 or detector 2 in order to be considered valid.

Note that this material is identical to the one used to represent the rover body in the investigation of charged particle directionality in Section 6.1. The detection and rejection efficiencies computed from both sets of simulations are given in Table 6.3.

In total, the efficiency for neutron detection is comparatively low. However, charged particles are rejected with a probability of more than 99 %. While gamma particles have a lower rejection rate of approximately 45 %, they also have a low detection efficiency. This indicates that the instrument can be expected to perform reliable and clean neutron detections.

The instruments detection efficiency can be further evaluated when comparing particle fluxes for different particles on the Martian surface. In order to assess this, the ground-level particle fluxes were simulated

using the Planetocosmics application. The simulation was set up using a present-day atmosphere profile taken from the Mars Climate Database (MCD) with a total altitude of 250 km. The primary particles were generated from solar minimum proton and alpha particle Galactic Cosmic Ray (GCR) energy spectra. The total neutron flux in the energy range from 1×10^{-1} MeV to 30 MeV computed from this simulation is $\Phi_{neutron} = 4.21\,particles/cm^2/s$, while the charged particle flux in the same energy range is $\Phi_{charged} = 0.81\,particles/cm^2/s$. Over the total energy range of the simulation, 1×10^{-1} MeV to 1×10^{5} MeV, the charged particle flux is $\Phi_{charged} = 2.81\,particles/cm^2/s$. It is clear that the flux of neutrons in the relevant energy range is bigger than the total flux of charged particles across the whole energy range. This does not yet take into account the detection efficiencies for different particles, however.

In order to estimate the probability of a neutron or proton coincidence, the probability of a particle entering one of the scintillation detectors is derived first. The total particle flux computed by Planetocosmics is $\Phi_{tot} = 102.80\,particles/cm^2/s$. One scintillator cube with a side length of $a = 30.75$ mm has an area of

$$A_s = a^2 \tag{6.2}$$

through which particles can enter, representing either the upper or the lower face of the scintillator cube. If the surface area through which one particle enters during the time t is

$$A' = \frac{1}{\Phi_{tot} t}\,, \tag{6.3}$$

then the total probability of a particle entering the detector p_{tot} is

$$p_{tot} = \frac{A_s}{A'}. \tag{6.4}$$

When the proton and neutron fluxes are designated as Φ_{proton} and $\Phi_{neutron}$, and the flux ratio of either particle as $r_{particle} = \frac{\Phi_{particle}}{\Phi_{tot}}$, the probability for one of the particles to enter a detector becomes

$$p_{particle} = r_{particle} p_{tot}. \tag{6.5}$$

With $p_{coin,particle}$ as the probability for a particle to generate a valid coincident signal as computed numerically above, the probability for a particle to generate a valid signal becomes

$$p_{signal,particle} = p_{coin,particle} p_{particle}. \tag{6.6}$$

The probability for a particle to hit the anti-coincidence detectors is computed in the same manner as above. The detector surface area for this is

$$A_r = b^2 \tag{6.7}$$

with $b = 50\,mm$. With

$$p_{tot,r} = \frac{A_r}{A'} \tag{6.8}$$

as the total probability of a particle entering the anti-coincidence detector, and $p_{anticoin,particle}$ as the probability for a particle to generate a signal in it, the total probability of a particle to be rejected by the anti-coincidence becomes

$$p_{reject,particle} = p_{anticoin,particle} p_{particle,r} \tag{6.9}$$

where $p_{particle,r} = r_{particle} p_{tot,r}$.

The total detection probability for a particle then becomes

$$p_{detect,particle} = p_{signal,particle}(1 - p_{reject,particle}) \tag{6.10}$$

For a time period of $t = 10\,ns$, the total detection probabilities become $p_{detect,neutron} = 1.19 \times 10^{-9}$ and $p_{detect,charged} = 6.04 \times 10^{-10}$, making the detection of a neutron almost twice as likely as the detection of a charged particle.

The proposed detection system has the capability to indirectly measure surface hydrogen content. Hydrogen can be present in the soil through subsurface water deposits or mineral composition. Its measurement is therefore extremely important in order to assess the habitability of the Martian surface and subsurface as well as understanding the development of Martian topography. Soil hydrogen content influences the upward directed neutron spectra, because the cross section for neutron-hydrogen interaction is extremely large due to their almost identical mass. Figure 6.2 shows the influence of soil water content on the upward directed neutron spectra. The variances in the spectra are clearly visible for different water contents, especially when looking at the ratio in comparison to dry soil. The most drastic changes, a reduction of neutron fluxes by a factor of approximately 0.3, are expected for particle energies below $100\,keV$, while the NDS is intended to measure neutrons above $0.3\,MeV$. Therefore, the hydrogen detection role in the proposed instrument will mainly be covered by the TNS, which was not investigated in the scope of this thesis.

6.2.3 *Conclusions*

This chapter presented and discussed two different methods for determining particle directionality on the Martian surface. The first method is designed for charged particles and can be applied to data taken by the RAD instrument. Due to the design of the instrument and the trigger setup used to detect incoming particle events, this method only works for particles with an energy of at least $100\,MeV\,nuc^{-1}$. Above an energy of approximately $200\,MeV\,nuc^{-1}$, it is no longer possible to discriminate between particle directions with this method.

However, total flux can still be derived, thus extending the measurement range of the RAD instrument. As shown in Section 6.1.4, the upward-directed charged particle fluxes are a factor of 0.1 less intense than the downward-directed fluxes. This necessitates the use of long time integration when applying the separation method in order to gain sufficient statistics for the upward flux measurement.

A design for an instrument able to measure neutron particle directionality was presented, and simulations of the instruments capabilities have been performed. The instrument is able to distinguish directionality of neutrons up to energies of $10\,MeV$, and particle energies for neutrons up to $5\,MeV$. It is also able to aid in soil hydrogen detection through detecting the difference of particle fluxes in the energy ranges influenced by subsurface hydrogen content in an energy range from $1\,eV$ to $1 \times 10^4\,eV$. However, the instrument design is not without engineering challenges. In order to effectively read out the B-doped scintillators, PMT tubes are needed. Their high operating voltage present a challenge in the Martian atmosphere due to the possibility of electrical arcs. In order to meet the goals described above, the ToF detection needs to be able to measure time differences on the order of a few nanoseconds, which is not easily done. These challenges are, however, possible to be overcome with careful design. Even though the instrument concept requires research and development work, it has been shown here to be a practicable design.

7

DISCUSSION AND CONCLUSIONS

As part of the MSL/RAD investigation, this work aims to help meet the science goals of the Radiation Assessment Detector (RAD) instrument. In particular, two goals have been addressed:

- The verification of simulation codes for particle transport in the Martian atmosphere.
- The characterization of the Martian radiation environment.

There are two main investigations presented herein, with both investigations contributing towards meeting both of the science goals. The first investigation is an effort to model the influence of atmospheric dust content and global dust storms on the Martian surface radiation environment. Secondly, a characterization of the directionality of particle fluxes, both on the Martian surface and in interplanetary space during the Mars Science Laboratory (MSL) cruise phase, is performed. In the following, the results of both investigations will be summarized and discussed, followed by conclusions and outlook.

7.1 DISCUSSION

Global Martian dust storms can drastically change the atmospheric conditions, and the second investigation in this thesis, in Section 6.2, is an attempt to model the influence of these changes on the Martian radiation environment. While no global dust storms have occurred to date during the MSL mission, there has been one time period during which enhanced atmospheric dust activity was observed. In simulations using the Mars Climate Database (MCD) atmosphere profiles, the drastic atmospheric changes during a global dust storm do not lead to changes in the ground-level radiation environment. Observational data during the time period of enhanced dust activity suggest a weak but significant correlation between atmospheric opacity and ground-level dose rate. Since the atmospheric opacity τ observed during the period of enhanced dust activity was not as high as during a global dust storm, the correlation analysis should be repeated if observations during a global dust storm become available. Around an altitude of 100 km, the simulations predict an enhancement of the ionization rate during a global dust storm. As discussed in Norman,

Gronoff, and Mertens (2014), this can lead to a degradation in surface downlink signals to landers operating on Mars, and radar signals transmitted through the Martian atmosphere, due to shielding by the ionized atmosphere layer. The simulation data predicts the changes of ionization rate to be more drastic during a Solar Energetic Particle (SEP) event due to the larger flux of relatively low-energy particles that deposit their energies in the relatively thin upper atmosphere layers. The simultaneous occurrence of an SEP event and a global dust storm has not so far been observed during the MSL mission. In conclusion, while the simulations presented here agree with the limited observational data available, no strong conclusions can be drawn. For that, RAD observations during a dust storm, either local or global, are needed, although these observations cannot be planned for. While an attempt has been made to compare simulations with observational data, care must be taken when doing so. The atmosphere profiles obtained from the MCD for a global dust storm scenario rely on an artificially fixed atmospheric opacity of $\tau = 5$ for the whole time frame during which such storms have been observed to be possible. While such an atmosphere profile represents the thermal layering of the Martian atmosphere during a global dust storm reasonably well, the pressure profile may not be well represented for all locations on the Martian surface. Atmospheric column mass, represented by ground-level atmospheric pressure, is an important factor in simulations of ground-level dose rate and particle spectra. If possible, a General Circulation Model (GCM) should be used to simulate atmospheric conditions during a global dust storm before performing particle transport simulations in future work.

The main result of the second part of this thesis, presented in Section 6.1, is the development of a method to distinguish charged particle directionality using the RAD instrument. The method has then been verified using data taken during the cruise phase and applied to and demonstrated on Martian surface data. It has been found that the simulations of both the cruise phase and surface data agree well with the instrument observations. This indicates that the simulation codes used here, the Geometry and Tracking version 4 (Geant4) code and the Planetocosmics application based on that code, are well suited to modeling the Martian surface environment and instruments aboard spacecrafts in interplanetary space. However, the shielding of the RAD instrument by the rover and the MSL cruise stage is not well known. The RAD instrument itself is well described through its Computer Aided Design (CAD) model. Such models also exists for both the rover and the cruise stage, but were not made available for this study. The abbreviated information on the shielding of the instrument may have led to inaccuracies in the simulations, however, the probability for that is low, as evidenced by the good agreement between the simulation and observation data.

In addition to the method for detecting charged particle directionality, a concept for an instrument capable of detecting neutron directionality has been studied. Applying the method developed for charged particles to neutrons is not possible due to its reliance on deterministic energy deposits made by the particles, while neutrons deposit energy stochastically. Instead, a concept of a Time of Flight (ToF) instrument capable of measuring neutron directionality in an energy range from $0.3\,MeV$ to $10\,MeV$ has been studied. In addition to directionality, this instrument is capable of measuring neutron energy spectra, limited charged particle energy spectra, and, albeit indirectly, the soil hydrogen content. A series of simulations of the proposed instrument have been performed in order to aid in the development process and to ascertain that it is capable of meeting its intended performance goals. While the instrument relies on technologies presenting an engineering challenge, e. g., the use of Photo-Multiplier Tube (PMT) in the thin Martian atmosphere, it is a feasible design capable of delivering its intended performance.

7.2 CONCLUSIONS

While the general method for determining charged particle directionality has been established, there are several aspects which have not been explored here due to time constraints. In particular, the variability of the ratio of upward to downward particle fluxes has not been investigated. There are several possible sources for variations of this ratio. Seasonal and diurnal atmospheric variations are known to lead to changes in the Martian radiation environment, as shown in, e. g., Rafkin et al. (2014) or Guo et al. (2015). Such changes could also lead to variations in the upward to downward ratio. A further factor influencing this could be the soil composition. However, Planetocosmics simulations investigating the influence of soil composition on the surface particle spectra point to this having an influence that is not possible to be modeled. Such changes should therefore be expected to be small, and might not be detectable using the method presented in Section 6.1, considering the large uncertainties. In general, detecting variations in the upward to downward ratio using this method will be challenging due to the large integration time needed to obtain reliable values for upward directed particle fluxes.

The investigation into the influence of global dust storms on the Martian radiation environment, presented in Chapter 5, has been hindered by the fact that necessary data sets for the analysis presented here are not yet available for a global dust storm, e. g., the storm observed in 2018. In addition to RAD observations, measurements of atmospheric opacity τ by the Mastcam simultaneously to the RAD observations are needed. As an additional facet of this investigation, an attempt to correlate the downlink signal strength of the Curiosity

rover should be made, which can be expected to yield insights to the increased ionization rate expected at an altitude of approximately 100 km. However, the rover engineering data sets containing this information might not be available to the science team due to restrictions. In order to produce meaningful particle transport simulation data to compare with observations, GCM data using the 3-D dust distribution for the particular storm under investigation should be performed, if possible.

The RAD instrument provides a first insight into the Martian radiation environment. While the measurements of charged particle spectra are detailed, and the instrument is able to provide further particle directionality measurements, the data regarding neutral particles is more limited due to the instrument design. In order to remedy this, the instrument concept presented and studied in Section 6.2 should be built and flown on an appropriate mission. This would provide further insight into the neutron radiation environment on the Martian surface, which would be very valuable to refine the assessment of habitability and the risk to possible future human explorers. The data would also be valuable in order to further the understanding of the development of the Martian topography through the instruments capability of subsurface hydrogen detection. In general, as evidenced, e. g., by the fact that neutron particle fluxes were instrumental in accurately replicating the upward to downward charged particle fluxes on the Martian surface through simulations, by their generation of secondary particles within the rover body, understanding the neutron radiation environment is important to fully understand the whole of the Martian radiation environment.

Measurements of the Martian radiation environment have only been made by the RAD instrument, inside Gale Crater, to date. However, as shown in Chapter 3, the Martian surface features a wide range of environments with differences in a variety of parameters, e. g., soil composition and, due to the large variations in local ground altitude, atmospheric pressure. In order to provide more data points to measurements of the radiation environments, and in order to explore the variations in local environments on the Martian surface, instruments similar to RAD in capability should be flown on appropriate missions landing on Mars in the future, since even the one point of measurement provided by RAD has revealed things not expected before, i. e., the diurnal variation described in Rafkin et al. (2014). Additionally, it is important to continue measurements of the radiation environment inside a spacecraft in interplanetary space during the cruise to Mars. This will help to provide additional data needed to develop appropriate radiation protection measures for future human exploration of Mars.

In the work presented within this thesis, the biggest challenge, as well as the biggest source of uncertainties, was the lack of sufficient

information regarding the shielding of the RAD instrument, both during the cruise phase and on the Martian surface. Had sufficient data on this been available, setting up the simulations for replicating the upward to downward flux ratio could have been done more quickly, since considerable time had to be spent on attempting to replicate the environment accurately enough and to validate the simulation. The solution was making educated guesses based on the best available data regarding the rover composition, including calculating the shielding mass the RAD Electronics Box (REB) adds to the RAD lower view cone from the CAD model of the instrument, as well as careful and extensive validation of the simulation setup built in this way.

In total, the work done in this thesis has contributed to meeting the RAD science goals. By helping to improve the understanding of the Martian radiation environment, and to validate and verify the suitability of simulation codes for the Martian environment, contributions have been made toward our understanding of the unique aspects of the planet. Overall, the MSL mission, and other missions currently underway on and around Mars, have made large improvements to the assessment of the present, and past, habitability of the Martian surface and subsurface. In fact, the RAD instrument used here has provided the first measurements of dose rate and ionizing radiation on another planet (Hassler et al., 2014). Results from other instruments on the MSL mission have helped to confirm a wet past on Mars, and the possible presence of a lake within Gale crater (Grotzinger et al., 2014). Today, the body of knowledge about the Martian environment shows a variety of different environments, and builds the basis for allowing future human exploration of Mars, as well as helping to understand and assess other possible habitats in the solar system.

BIBLIOGRAPHY

[1] S. Agostinelli et al. "Geant4—a simulation toolkit". In: *Nuclear Instruments and Methods in Physics Research Section A: Accelerators, Spectrometers, Detectors and Associated Equipment* 506.3 (July 2003), pp. 250–303. ISSN: 01689002. DOI: 10.1016/S0168-9002(03)01368-8 (cit. on p. 36).

[2] Matthew J.I. Balmer, Kelum A.A. Gamage, and Graeme C. Taylor. "Critical review of directional neutron survey meters". In: *Nuclear Instruments and Methods in Physics Research Section A: Accelerators, Spectrometers, Detectors and Associated Equipment* 735 (Jan. 2014), pp. 7–11. DOI: 10.1016/j.nima.2013.08.087 (cit. on p. 95).

[3] J. F. Bell et al. "Mineralogic and compositional properties of Martian soil and dust: Results from Mars Pathfinder". In: *Journal of Geophysical Research: Planets* 105.E1 (Jan. 2000), pp. 1721–1755. ISSN: 01480227. DOI: 10.1029/1999JE001060 (cit. on p. 33).

[4] E. G. Berezhko. "Cosmic ray acceleration by supernova shocks". In: *Advances in Space Research* 41 (2008), pp. 429–441. DOI: 10.1016/j.asr.2007.04.034. arXiv: 0809.0738 (cit. on p. 26).

[5] H. Bethe. "Zur Theorie des Durchgangs schneller Korpuskularstrahlen durch Materie". In: *Annalen der Physik* 397.3 (1930), pp. 325–400. ISSN: 15213889. DOI: 10.1002/andp.19303970303 (cit. on p. 93).

[6] R.T. Clancy et al. "An intercomparison of ground-based millimeter, MGS TES, and Viking atmospheric temperature measurements: Seasonal and interannual variability of temperatures and dust loading in the global Mars atmosphere". In: *J. Geophys. Res.* 105.E4 (Apr. 2000), pp. 9553–9571 (cit. on p. 33).

[7] J. E. P. Connerney et al. "The Global Magnetic Field of Mars and Implications for Crustal Evolution". In: *Geophysical Research Letters* 28.21 (2001), pp. 4015–4018 (cit. on pp. 26, 27).

[8] L. R. Dartnell et al. "Modelling the surface and subsurface Martian radiation environment: Implications for astrobiology". In: 34, L02207 (Jan. 2007), p. L02207. DOI: 10.1029/2006GL027494 (cit. on p. 39).

[9] M. Desorgher, L.; Flückiger, E. O.; Gurtner. "The PLANETOCOSMICS Geant4 application". In: *36th COSPAR Scientific Assembly*. Beijing, 2006 (cit. on pp. 33, 38).

[10] Laurent Desorgher. *PLANETOCOSMICS Software User Manual*. Tech. rep. Physikalisches Institut, University of Bern, Switzerland, 2005, pp. 1–106 (cit. on pp. 33, 38).

[11] J. F. Drake et al. "A Magnetic Reconnection Mechanism for the Generation of Anomalous Cosmic Rays". In: 709 (Feb. 2010), pp. 963–974. DOI: 10.1088/0004-637X/709/2/963. arXiv: 0911.3098 [astro-ph.SR] (cit. on p. 26).

[12] Lori K. Fenton, Paul E. Geissler, and Robert M. Haberle. "Global warming and climate forcing by recent albedo changes on Mars." In: *Nature* 446.7136 (2007), pp. 646–649. ISSN: 0028-0836. DOI: 10.1038/nature05718 (cit. on pp. 29, 32).

[13] S. E. Forbush. "On cosmic-ray effects associated with magnetic storms". In: *Terrestrial Magnetism and Atmospheric Electricity (Journal of Geophysical Research)* 43 (1938), p. 203. DOI: 10.1029/TE043i003p00203 (cit. on p. 28).

[14] F. Forget, E. Millour, and S. R. Lewis. *Mars Climate Database v5.0 Detailed Design Document*. Tech. rep. 2012, p. 37 (cit. on pp. 32, 33).

[15] Thomas K. Gaisser. *Cosmic Rays and Particle Physics*. Cambridge University Press, 1990. ISBN: 9780521339315 (cit. on p. 26).

[16] Javier Gómez-Elvira et al. "Curiosity's rover environmental monitoring station: Overview of the first 100 sols". In: *Journal of Geophysical Research: Planets* 119.7 (July 2014), pp. 1680–1688. ISSN: 21699097. DOI: 10.1002/2013JE004576 (cit. on pp. 28, 29).

[17] J. P. Grotzinger et al. "A Habitable Fluvio-Lacustrine Environment at Yellowknife Bay, Gale Crater, Mars". In: *Science* 343.27, 1242777 (Jan. 2014), p. 1242777. DOI: 10.1126/science.1242777 (cit. on p. 111).

[18] John P. Grotzinger et al. "Mars Science Laboratory Mission and Science Investigation". In: *Space Science Reviews* 170.1-4 (July 2012), pp. 5–56. ISSN: 00386308. DOI: 10.1007/s11214-012-9892-2 (cit. on p. 17).

[19] J. Guo et al. "Modeling the Variations of Dose Rate Measured by RAD during the First MSL Martian Year: 2012-2014". In: 810, 24 (Sept. 2015), p. 24. DOI: 10.1088/0004-637X/810/1/24. arXiv: 1507.03473 [astro-ph.EP]. URL: http://adsabs.harvard.edu/abs/2015ApJ...810...24G (cit. on p. 109).

[20] Mark A. Gurwell et al. "Mars surface and atmospheric temperature during the 2001 global dust storm". In: *Icarus* 175.1 (2005), pp. 23–31. ISSN: 00191035. DOI: 10.1016/j.icarus.2004.10.009 (cit. on p. 31).

[21] Robert M Haberle, Conway B Leovy, and James B Pollack. "Some effects of global dust storms on the atmospheric circulation of Mars". In: *Icarus* 50.2-3 (1982), pp. 322–367 (cit. on p. 29).

[22] D. M. Hassler et al. "The Radiation Assessment Detector (RAD) Investigation". In: *Space Science Reviews* (July 2012). ISSN: 0038-6308. DOI: 10.1007/s11214-012-9913-1 (cit. on pp. 21, 22, 24).

[23] DM Hassler et al. "Mars' Surface Radiation Environment Measured with the Mars Science Laboratory's Curiosity Rover". In: *Science* 343.6169 (Dec. 2014), pp. 1244797–1244797. DOI: 10.1126/science.1244797 (cit. on pp. 92, 111).

[24] Donald Hassler et al. *RAMA (Radiation, neutron Albedo, and MApping of hydrogen) Proposal*. Tech. rep. 2015 (cit. on p. 95).

[25] S. L. Hess et al. "The annual cycle of pressure on Mars measured by Viking Landers 1 and 2". In: *Geophysical Research Letters* 7.3 (1980), pp. 197–200. ISSN: 19448007. DOI: 10.1029/GL007i003p00197 (cit. on pp. 19, 28, 29).

[26] J. A. Jacobs. "Planetary magnetic fields". In: *Geophysical Research Letters* 6.3 (1979), pp. 213–214. ISSN: 19448007. DOI: 10.1029/GL006i003p00213 (cit. on p. 26).

[27] C. G. Justus, B. F. James, and S. W. Bougher. "Mars-GRAM 2000: A Mars atmospheric model for engineering applications". In: *Adv. Space Res.* 29.2 (2002), pp. 193–202. DOI: 10.1016/S0273-1177(01)00569-5 (cit. on p. 32).

[28] J. Köhler et al. "Inversion of neutron/gamma spectra from scintillator measurements". In: *Nuclear Instruments and Methods in Physics Research Section B: Beam Interactions with Materials and Atoms* 269.22 (Nov. 2011), pp. 2641–2648. ISSN: 0168583X. DOI: 10.1016/j.nimb.2011.07.021 (cit. on pp. 36, 92).

[29] Hanno Krieger. *Grundlagen der Strahlungsphysik und des Strahlenschutzes, 2., überarbeitete und erweiterte Auflage*. 2007, p. 710. ISBN: 9783835101999 (cit. on p. 93).

[30] C. B. Leovy, R. W. Zurek, and J. B. Pollack. "Mechanisms for Mars dust storms". In: *Journal of the Atmospheric Sciences* 30.5 (1973), pp. 749–762. DOI: 10.1175/1520-0469(1973)030<0749:MFMDS>2.0.CO;2 (cit. on pp. 29, 32).

[31] Conway B. Leovy and Richard W. Zurek. "Thermal tides and Martian dust storms: Direct evidence for coupling". In: *Journal of Geophysical Research* 84.B6 (1979), p. 2956. DOI: 10.1029/jb084ib06p02956 (cit. on p. 29).

[32] Stephen R. Lewis et al. "A climate database for Mars". In: *J. Geophys. Res.* 104.E10 (Oct. 1999), p. 24177. ISSN: 0148-0227. DOI: 10.1029/1999JE001024 (cit. on p. 32).

[33] Percival Lowell. *Mars and its canals*. The Macmillan company; London: Macmillan & Co., Ltd., 1906 (cit. on p. 17).

[34] P. R. Mahaffy et al. "Abundance and Isotopic Composition of Gases in the Martian Atmosphere from the Curiosity Rover". In: *Science (New York, N.Y.)* 341.July (2013), pp. 263–266. ISSN: 0036-8075. DOI: 10.1126/science.1237966 (cit. on p. 28).

[35] G. M. Martínez et al. "The Modern Near-Surface Martian Climate: A Review of In-situ Meteorological Data from Viking to Curiosity". In: *Space Science Reviews* (Apr. 2017). DOI: 10.1007/s11214-017-0360-x (cit. on p. 30).

[36] D. Matthiä et al. "The Martian surface radiation environment - a comparison of models and MSL/RAD measurements". In: *Journal of Space Weather and Space Climate* 6.27, A13 (Mar. 2016), A13. DOI: 10.1051/swsc/2016008. URL: http://adsabs.harvard.edu/abs/2016JSWSC...6A..13M (cit. on pp. 38, 39).

[37] D. J. McCleese et al. "Structure and dynamics of the Martian lower and middle atmosphere as observed by the Mars Climate Sounder: Seasonal variations in zonal mean temperature, dust, and water ice aerosols". In: *Journal of Geophysical Research E: Planets* 115.12 (2010), pp. 1–16. ISSN: 01480227. DOI: 10.1029/2010JE003677 (cit. on p. 28).

[38] H. Y. McSween et al. "Chemical, multispectral, and textural constraints on the composition and origin of rocks at the Mars Pathfinder landing site". In: *Journal of Geophysical Research: Planets* 104.E4 (Apr. 1999), pp. 8679–8715. ISSN: 01480227. DOI: 10.1029/98JE02551 (cit. on p. 33).

[39] R. A. Mewaldt et al. "Energy spectra, composition, and other properties of ground-level events during solar cycle 23". In: *Space Science Reviews* 171.1-4 (2012), pp. 97–120. ISSN: 00386308. DOI: 10.1007/s11214-012-9884-2 (cit. on p. 26).

[40] J.-P. Meyer. "The baseline composition of solar energetic particles". In: *Astrophysical Journal Supplement* 57 (Jan. 1985), pp. 151–171. DOI: 10.1086/191000 (cit. on p. 26).

[41] K. Min et al. "(U-Th)/He ages of phosphates from Zagami and ALHA77005 Martian meteorites: Implications to shock temperatures". In: 196 (Jan. 2017), pp. 160–178. DOI: 10.1016/j.gca.2016.09.009 (cit. on p. 17).

[42] D. W. Mittlefehldt. "ALH84001, a cumulate orthopyroxenite member of the Martian meteorite clan". In: *Meteoritics* 29 (Mar. 1994), pp. 214–221 (cit. on p. 17).

[43] L. Montabone et al. "Validation of martian meteorological data assimilation for MGS/TES using radio occultation measurements". In: *Icarus* 185.1 (2006), pp. 113–132. ISSN: 00191035. DOI: 10.1016/j.icarus.2006.07.012 (cit. on p. 17).

[44] A. O. Nier and M. B. Mcelroy. "Composition and structure of Mars' upper atmosphere results from the neutral mass spectrometers on Viking 1 and 2". In: *Journal of Geophysical Research* 82.28 (1977), pp. 4341–4349. ISSN: 0148-0227. DOI: 10.1029/JS082i028p04341 (cit. on p. 28).

[45] Koji Niita et al. "PHITS—a particle and heavy ion transport code system". In: *Radiation Measurements* 41.9-10 (Oct. 2006), pp. 1080–1090. ISSN: 13504487. DOI: 10.1016/j.radmeas.2006.07.013 (cit. on p. 39).

[46] Ryan B. Norman, Guillaume Gronoff, and Christopher J. Mertens. "Influence of dust loading on atmospheric ionizing radiation on Mars". In: *Journal of Geophysical Research: Space Physics* 119.1 (Jan. 2014), pp. 452–461. ISSN: 21699380. DOI: 10.1002/2013JA019351 (cit. on pp. 19, 20, 41, 107).

[47] P.M. O'Neill. "Badhwar-O'Neill 2010 Galactic Cosmic Ray Flux Model —Revised". In: *IEEE Transactions on Nuclear Science* 57.6 (Dec. 2010), pp. 3148–3153. DOI: 10.1109/tns.2010.2083688 (cit. on p. 27).

[48] I O Ogunniyi, M K G Vermaak, and D R Groot. "Chemical composition and liberation characterization of printed circuit board comminution fines for beneficiation investigations." In: *Waste management (New York, N.Y.)* 29.7 (July 2009), pp. 2140–6. ISSN: 0956-053X. DOI: 10.1016/j.wasman.2009.03.004 (cit. on pp. 100, 102).

[49] Z. Osmanov, A. Rogava, and G. Bodo. "On the efficiency of particle acceleration by rotating magnetospheres in AGN". In: *Astronomy and Astrophysics* 470 (2007), pp. 395–400. DOI: 10.1051/0004-6361:20065817 (cit. on p. 26).

[50] T. Owen et al. "The composition of the atmosphere at the surface of Mars". In: *Journal of Geophysical Research* 82.28 (1977), pp. 4635–4639. DOI: 10.1029/JS082i028p04635 (cit. on p. 28).

[51] Marius S. Potgieter. "The dynamic heliosphere, solar activity, and cosmic rays". In: *Advances in Space Research* 46.4 (2010), pp. 402–412. ISSN: 02731177. DOI: 10.1016/j.asr.2009.09.016 (cit. on pp. 25, 26, 28).

[52] D. A. Prokopovich et al. "Geant4 simulation of the CERN-EU high-energy reference field (CERF) facility". In: *Radiat. Prot. Dosim.* 141.2 (May 2010), pp. 106–113. DOI: 10.1093/rpd/ncq152 (cit. on p. 36).

[53] M. Purucker et al. "An altitude-normalized magnetic map of Mars and its interpretation". In: *Geo* 27.16 (2000), pp. 2449–2452 (cit. on pp. 17, 26).

[54] Scot C.R. Rafkin et al. "Diurnal variations of energetic particle radiation at the surface of Mars as observed by the Mars Science Laboratory Radiation Assessment Detector". In: *Journal of Geophysical Research: Planets* 119 (2014), pp. 1345–1358. DOI: 10.1002/2013JE004525 (cit. on pp. 29, 31, 109, 110).

[55] R. Rieder. "The Chemical Composition of Martian Soil and Rocks Returned by the Mobile Alpha Proton X-ray Spectrometer: Preliminary Results from the X-ray Mode". In: *Science* 278.5344 (Dec. 1997), pp. 1771–1774. ISSN: 00368075. DOI: 10.1126/science.278.5344.1771 (cit. on p. 33).

[56] F.M. Rieger and K. Mannheim. "Particle acceleration by rotating magnetospheres in active galactic nuclei". In: *Astron. Astrophys.* 353 (2000), pp. 473–478 (cit. on p. 26).

[57] Giovanni Schiaparelli. "The Distribution of Land and Water on Mars". In: *Publications of the Astronomical Society of the Pacific* 5.31 (1893). ISSN: 0004-6280. DOI: 10.1086/120651 (cit. on p. 17).

[58] Giovanni Schiaparelli. "Observations of the Planet Mars". In: *Science* 9.227 (1899). DOI: 10.1126/science.9.227.633 (cit. on p. 17).

[59] J. Spiga et al. "The GEANT4 toolkit for microdosimetry calculations: Application to microbeam radiation therapy (MRT)". In: *Med. Phys.* (Nov. 2007). DOI: 10.1118/1.2794170 (cit. on p. 36).

[60] Huiqun Wang. "Relationship between frontal dust storms and transient eddy activity in the northern hemisphere of Mars as observed by Mars Global Surveyor". In: *Journal of Geophysical Research* 110.E7 (2005). DOI: 10.1029/2005je002423 (cit. on p. 29).

[61] John W. Wilson et al. "HZETRN: Description of a free-space ion and nucleon transport and shielding computer program". In: Technical report NASA-TP-3495 (1995), pp. 1–148 (cit. on pp. 20, 35).

[62] John W. Wilson et al. "Advances in NASA radiation transport research: 3DHZETRN". In: *Life Sciences in Space Research* 2.Supplement C (2014), pp. 6–22. ISSN: 2214-5524. DOI: https://doi.org/10.1016/j.lssr.2014.05.003. URL: http://www.sciencedirect.com/science/article/pii/S2214552414000297 (cit. on p. 35).

[63] R. J. Wilson and K. Hamilton. "Comprehensive model simulation of thermal tides in the Martian atmosphere." In: *Journal of Atmospheric Sciences* 53 (May 1996), pp. 1290–1326. DOI: 10.1175/1520-0469(1996)053<1290:CMSOTT>2.0.CO;2. URL: http://adsabs.harvard.edu/abs/1996JAtS...53.1290W (cit. on p. 29).

[64] C. Zeitlin et al. “Measurements of Energetic Particle Radiation in Transit to Mars on the Mars Science Laboratory”. In: *Science* 340.6136 (May 2013), pp. 1080–1084. ISSN: 0036-8075. DOI: 10.1126/science.1235989 (cit. on p. 23).

[65] Richard W. Zurek. “Inference of dust opacities for the 1977 Martian great dust storms from Viking Lander 1 pressure data”. In: *Icarus* 45.1 (Jan. 1981), pp. 202–215. DOI: 10.1016/0019-1035(81)90014-2 (cit. on p. 29).